CERN 99–12
16 December 1999

CERN 99–12

LABORATOIRE EUROPÉEN POUR LA PHYSIQUE DES PARTICULES
CERN EUROPEAN LABORATORY FOR PARTICLE PHYSICS

$\mu^+ - \mu^-$ COLLIDERS

David Neuffer

GENEVA
1999

ISSN 0007-8328
ISBN 92-9083-158-8

CERN 99–12
16 December 1999

LABORATOIRE EUROPÉEN POUR LA PHYSIQUE DES PARTICULES
CERN EUROPEAN LABORATORY FOR PARTICLE PHYSICS

$\mu^+ - \mu^-$ COLLIDERS

David Neuffer

GENEVA
1999

CERN–Service d'information scientifique–RD/997–2000–décembre 1999

Abstract

In these lectures the concept of a high-energy, high-luminosity μ^+–μ^- collider is developed. A μ^+–μ^- collider would provide heavy lepton collisions, with unique capabilities in the exploration of Higgs bosons at 100–180 GeV energies, and it could be extended to multi-TeV energies. A μ^+–μ^- collider requires a high-intensity proton source for pion production, a high-acceptance decay channel to collect muons from pion decay, a muon cooling system, a rapid acceleration system, and a high-luminosity collider ring for the collisions of short, intense μ^+–μ^- bunches. Critical problems exist in each of the collider concept components, and in the interaction-region detectors needed to analyse the collisions. These problems and the search for solutions within the current μ^+–μ^- collider research programme are described.

CONTENTS

1 INTRODUCTION

The presently emphasized approaches in high-energy accelerators are reaching critical size and performance constraints. It appears that hadronic colliders (p–p) are reaching maximum cost and size limitations with the CERN Large Hadron Collider (LHC) with up to 14 TeV collisions, and are performance-constrained in that they produce complicated many-particle collisions, with a rapidly diminishing fraction (in numbers and energy) of the interactions in point-like new-particle-state production. Lepton (e^+–e^-) colliders produce simple interactions, and this magnifies the effective energy of collisions by more than an order of magnitude over hadron colliders. Extension of e^+–e^- colliders to multi-TeV energies (effectively beyond the LHC) is constrained by 'beamstrahlung' and synchrotron radiation effects, which increase as $(E_e/m_e)^4$, limiting performance as well as forcing the use of two costly full-energy linacs, with impractically large size requirements and power demands (GW or more).

However, muons (heavy electrons, with $m_\mu = 200\ m_e$) have negligible radiation and beamstrahlung, and can be accelerated and stored in multiturn recirculating devices or rings. The liabilities of muons are that they decay, with a lifetime of $2.2 \times 10^{-6}\, E_\mu/m_\mu$ s, and that they are created through decay into a diffuse phase space. But the phase space can be reduced by ionization cooling, and the lifetime is sufficient for storage-ring collisions. (At 2 TeV, $\tau_\mu = 0.044$ s.) Following these observations, the μ^+–μ^- collider concept, in which intense bunches of muons are generated, accelerated and collided, was introduced [1], [2].

Recently, more substantial investigations into the possibilities of high-luminosity muon (μ^+–μ^-) colliders have developed [3]–[7], and critical improvements in collider scenarios have been initiated which promise the possibility of high luminosity. This intensified activity resulted in the Muon Collider Feasibility Study reported at the 1996 DPF/DPB Summer Study on High Energy Physics (Snowmass 96) [8]. The Muon Collider Collaboration, a multi-laboratory organization, has been formed to intensify study of the concept [9]. This collaboration has identified critical physics goals and requirements for useful colliders, and has studied many components of potential scenarios in detail. The results of many of these studies are summarized in the published status report. The goal of the collaboration is to complete sufficient R& D within the next few years to determine whether a physically useful muon collider is technically feasible, and, if it is, to design the First Muon Collider. The research reported in the present report is based on the efforts of that collaboration.

The studies have identified several specific physics goals of a muon collider [10]. The most attractive near-term goal is in the exploration of the Higgs boson. Because the Higgs Boson H couples through the particle mass m, with a strength proportional to m2, the s-channel process for Higgs production in a μ^+–μ^- collider μ^+–$\mu^- \rightarrow$ H) would be enhanced through the relatively large muon mass. Theoretical studies support the concept that the Higgs boson mass is in the 100–150 GeV mass region, and exploration of Higgs particle properties in a μ^+–μ^- collider 'Higgs factory' is an attractive goal for a first muon collider. Other possible physics goals include Z-physics measurements, precision m_W and m_t measurements, deep-inelastic physics, supersymmetry observations, including new particle production, strong WW production physics, light and heavy technicolour studies, new Z particles, plus any other unknown discoveries which may be obtained by extending a new type of particle probe into an extended energy regime.

At the lower end of the energy spectra, recent observations support the possibility that neutrinos have finite (but very small) masses and that neutrino oscillations among the various neutrino types occur. Exploration of this neutrino physics will require higher intensity neutrino beams, and that implies higher intensity pion and muon beams, using the same techniques that we are developing to obtain the high-intensity μ^+–μ^- bunches needed for a high-luminosity collider.

Most of these physics goals, including the Higgs factory, require relatively high luminosities. A luminosity of 10^{31} cm^{-2}/s or higher would be needed for thorough exploration of a Standard Model low-mass Higgs at $\sim$ 100 GeV, and the luminosity should increase from this value in proportion to $\sim$ E^2 for higher-energy general-purpose colliders. The Muon Collider Collaboration is developing collider concepts with these luminosity goals. Table 1.1 shows some possible parameters for μ^+–μ^- colliders. It includes a $\sim$ 100 GeV Higgs factory, which can operate in a small energy width mode for precision measurements or a higher-luminosity mode. The Table also includes parameters for a $\sim$ 400 GeV collider (at the t–t* region) and a high-energy 4 TeV collider with a luminosity of L = 10^{35} cm^{-2}s^{-1}. Figure 1.1 shows a conceptual overview of the collider concept, and Fig. 1.2 shows a 3 TeV collider concept drawn to scale within the Fermilab site map. Figure 1.3 shows a 500 GeV and 4 TeV collider at a randomly selected location.

Table 1.1
Parameter lists for μ^+–μ^- colliders

Parameter	Higgs factory (Small-large δE)	Top source	4 TeV
Collision energy (2 E$_\mu$) (GeV)	100	400	4000
Energy per beam (E$_\mu$) (GeV)	50	200	2000
Luminosity (L = f$_0$n$_s$n$_b$N$_\mu^2$/4$\pi\sigma^2$)(cm^{-2}s^{-1})	10^{31}–10^{32}	10^{33}	10^{35}
Source parameters (4 MW p-beam)			
Proton energy (E$_p$) (GeV)	16	16	30
Protons/pulse (N$_p$)	$4 \times 2.5 \times 10^{13}$	$4 \times 2.5 \times 10^{13}$	$4 \times 3 \times 10^{13}$
Pulse rate (f$_0$) (Hz)	15	15	15
μ acceptance (μ/p)	0.2	0.2	0.2
μ-survival (N$_\mu$/N$_{source}$)	0.4	0.4	0.4
Collider parameters			
Collider mean radius (R) (m)	50	150	1200
μ /bunch (N$_{\mu\pm}$)	4×10^{12}	2×10^{12}	2.5×10^{12}
Number of bunches (n$_B$)	1	2	2
Storage turns (2n$_s$)	1000	1500	1800
Normalized emittance (ϵ_N) (cm-rad)	0.028–0.01	10^{-2}	5×10^{-3}
μ-beam emittance ($\epsilon_t = \epsilon_{N/\gamma}$) (cm-rad)	(5.6–2) $\times 10^{-5}$	5.3×10^{-6}	2.5×10^{-7}
Interaction focus β_0 (cm)	13–4	1	0.3
IR beam size sigma = $(\epsilon\beta_0)^{1/2}$ (μm)	270–90	23	2.1
δE/E at collisions (%)	0.003–0.12	0.12	0.12

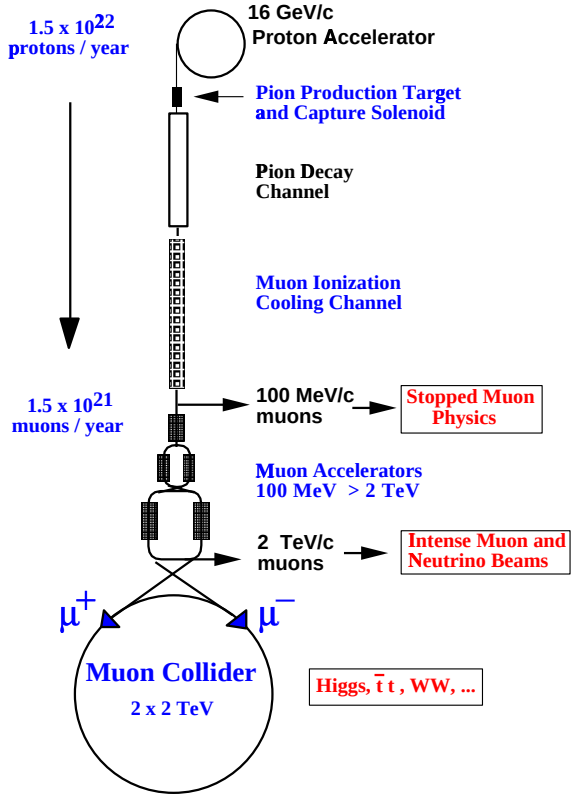

Fig. 1.1: Overview of the μ^+–μ^- Collider Facility showing proton source, muon production and cooling, acceleration and collider components.

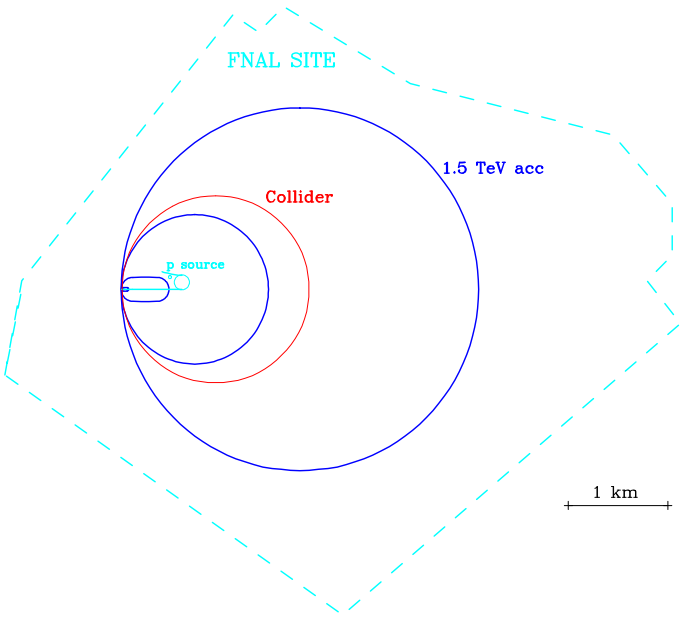

Fig. 1.2: Scale model of a 3 TeV muon collider superimposed on the Fermilab site. The proton source, m-production and cooling channel occupy a small are in the right centre. The source accelerators and collider ring fit easily within the site boundaries.

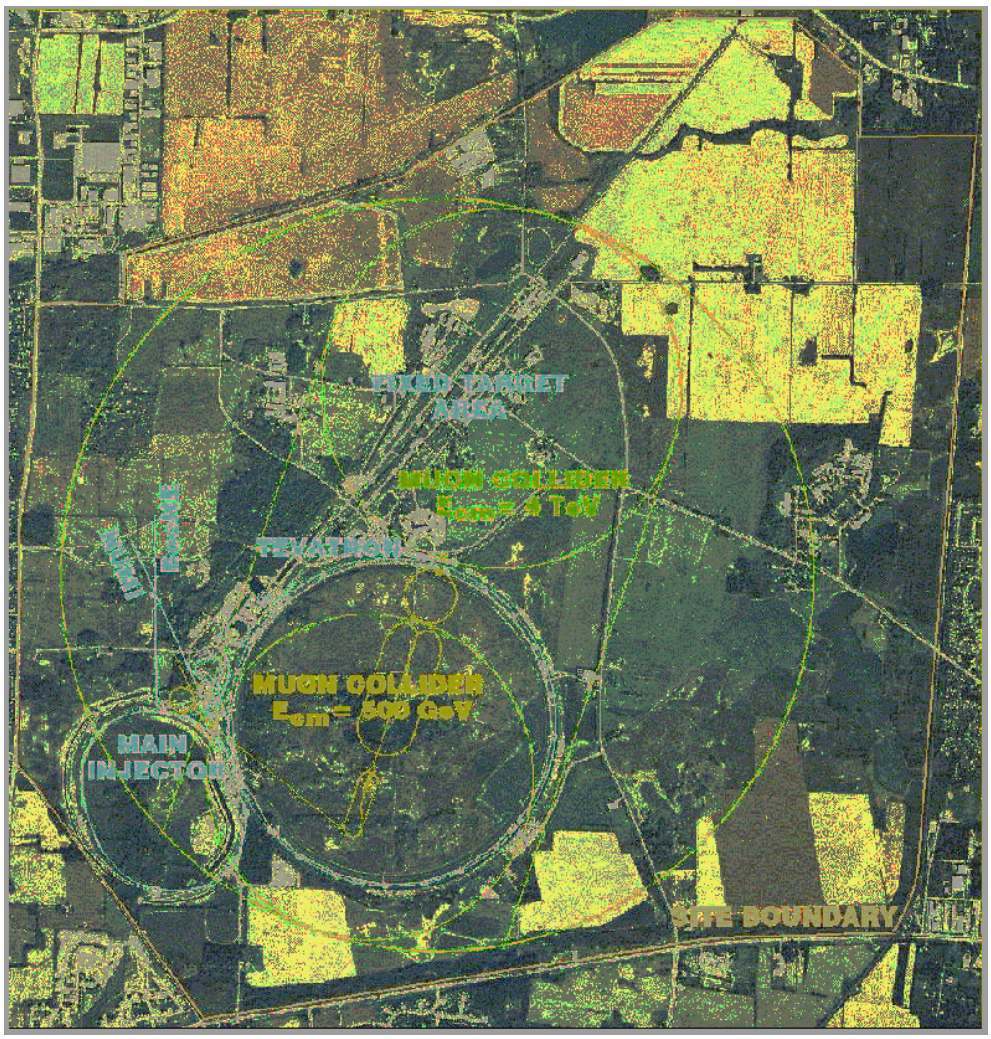

Fig. 1.3: Photograph of the Fermilab site (with main injector, BOONE and NUMI beam lines, Tevatron, and fixed target areas), with schematic drawings of μ^+–μ^- colliders superimposed.

Each of these scenarios is based upon the same muon source concept, with further acceleration and higher energy collider rings added to obtain the higher energy cases. The muon source is based on a high-intensity proton synchroton which generates short, high-intensity pulses of protons. These pulses are transported onto a high-Z target, which is immersed within a high-field solenoid, where the pulses produce large numbers of pions. The pions are captured within the high-field, which is adiabatically matched to a low-field solenoid transport which also contains a low-frequency RF system. The pions decay to muons within the transport, while the RF system rotates the beam in phase space, limiting the captured beam energy spread while lengthening the bunches.

The muon bunches are captured within a phase space which is too diffuse for high-luminosity collisions, and must be compressed and cooled. The cooling method which is used in the scenarios is ionization cooling, in which muons lose energy while passing through material (losing transverse and longitudinal momentum) and are reaccelerated (regaining only longitudinal momentum); a transport with multiple energy loss and acceleration sections can cool by large factors. As described below, the phase-space densities used in Table 1.1 are based on calculated limits of ionization cooling.

The cooled μ^+ and μ^- bunches are then accelerated through a sequence of multiturn accelerators [linac, recirculating linac (RLA), fixed-field alternating-gradient (FFAG) and/or very-rapid-cycling synchrotron (VRCS)] to full energy, where they are inserted into a collider ring. The muons circulate in the collider ring for a muon lifetime ($n_S \cong 1000$ turns), where they are focused to collisions within the detectors of the ring interaction areas. The entire process is repeated at the muon source repetition rate (f_0).

The expression for luminosity (for equal intensity round beams) is:

$$L = \frac{f_0 n_S n_b \gamma_\mu N_\mu^2}{4\pi \epsilon_N \beta^*}$$

where n_S is the luminosity lifetime (in turns) in the collider, n_b is the number of colliding bunches in each beam, N_μ is the number of muons per bunch, $\gamma_\mu = E_\mu/m_\mu$), ϵ_N is the normalized emittance, and β^* is the collider focusing parameter, with the beam size at collisions given by $\sigma^2 = \epsilon_N \beta^*/\gamma_\mu$.

Each of the components of these scenarios will be described in more detail below, and critical problems in their implementation will be discussed. Chapter 2 describes the proton source and possible variations. Chapter 3 describes the target, pion production and muon capture problems. Chapter 4 discusses the challenges associated with muon cooling. Because ionization cooling is a novel technique that has not yet been utilized, muon cooling has been a primary focus of recent research and receives a more extensive presentation in this report. Chapter 5 describes possible acceleration scenarios and components. The collider ring and the detector problems are discussed in detail in Chapter 6, and neutrino opportunities (n-beams from the collider concept, and the proton source) and problems (n-radiation) are discussed in Chapter 7. The current R&D programme toward implementation of μ^+–μ^- collider concepts, including simulation studies, targetry experiments, cooling experiments, and other efforts are summarized in Chapter 8.

In outlining these presently developing scenarios, we do not exclude the possibilities that significantly different scenarios for a μ^+–μ^- collider could be developed, or that particular components of the scenarios could be greatly changed. Indeed the current R&D has identified many difficulties which will require significant innovations and/or inventions for adequate solutions. We hope that this discussion will inspire the reader (Hello, there!) to develop improvements and innovations to the presently developing baseline collider scenarios.

References

[1] A.N. Skrinsky and V.V. Parkhomchuk, Sov. J. Nucl. Phys. **12**, 3 (1981); E.A. Perevedentsev and A.N. Skrinsky, *Proc. 12th Int. Conf. High Energy Accel.*, p. 485 (1983).

[2] D. Neuffer, Fermilab Note FN-319, July 1979; D. Neuffer, Part. Accel. **14**, 75 (1983); D. Neuffer, *Proc. 12th Int. Conf. High Energy Accel.*, p. 481 (1983); D. Neuffer, Nucl. Instrum. Methods **A350**, 27 (1994).

[3] D. Neuffer and R. Palmer, Proc. 1994 EPAC, p. 52 (London, 1994).

[4] D. Cline, ed., *Physics Potential and Development of μ^+–μ^- Colliders*, AIP Conf. Proc. **352** (1996).

[5] J.C. Gallardo, ed., *Beam Dynamics and Technology Issues for μ^+–μ^- Colliders*, AIP Conf. Proc. **372** (1996).

[6] D.B. Cline, ed., *μ^+–μ^- Colliders*, Nucl. Phys. B (Proc. Suppl.) **51A** (1996).

[7] D.B. Cline, ed., *Proc. 4th Int. Conf. on the Physics Potential and Development of μ^+–μ^- Colliders*, AIP Conf. Proc. **441** (1998).

[8] $\mu^+\mu^-$ Collider - A Feasibility Study, BNL-52503, Fermi-Lab-Conf.-96-092, LBNL-38946 (1996), presented at the Snowmass 96 Workshop (1997).

[9] C.M. Ankenbrandt et al., 'Status of muon collider research', submitted to Phys. Rev. Special Topics (1998).

[10] V. Barger, M. Berger, J. Gunion, and T. Han, Nucl. Phys. B (Proc. Suppl.) **51A**, 13 (1996); Phys. Rep. **286**, 1 (1997).

2 PROTON SOURCE

2.1 Introduction

High luminosity requires a large number of muons ($n_b N_\mu$) compressed into a relatively small number of bunches (n_b) produced at a relatively high rate (n_s). Each of these bunches derives from primary proton bunches (in the baseline scenario); therefore, the proton driver should produce a large number of protons within a relatively small number of primary proton bunches.

The critical parameter in translating from proton intensity to collider muon intensity is $\eta_{\mu/p}$, the number of useful muons captured per primary proton. Recent simulations of the production and capture of muons (as reported in the next section) indicate that, in our baseline scenarios, $\eta_{\mu/p} \cong 0.3$. This estimate could change with experimental observations and/or scenario changes, which would change the proton driver requirements.

With this estimate, the parameters of the proton source have been chosen to be relatively modest extrapolations of existing machines. Table 2.1 shows parameters of a possible source and Fig. 2.1 shows an overview of a proton driver source. The cycle time of 15 Hz is the Fermilab booster cycle time. The beam intensities of $n_b = 4$ bunches, $N_p = 2.5 \times 10^{13}$ protons/bunch or 10^{14} protons/cycle are similar to BNL AGS parameters. The beam energy is 16 GeV, within the optimal 10–30 GeV range for efficient production of ~ 400 MeV/c pions, and the overall beam power is 4 MW, similar to that proposed for the (cancelled) TRIUMF KAON factory [1].

A critical difference between this source and previously developed KAON proposals is that the protons are delivered in a relatively small number of compressed bunches, rather than in a continuous stream. This implies that a compatible RF system with a bunch formation and compression scenario is required, such as that described in the next section.

This proton driver would be the centrepiece of a new μ^+–μ^- collider facility, and could also serve as a premier high-intensity source for medium-energy physics explorations, including K, hypernucleon, π, μ and ν physics explorations. Some of these, particularly the neutrino-beam opportunities, are discussed in Chapter 7 below.

Table 2.1
Parameters of a 16 GeV proton source

Parameter	Linac	Prebooster	Booster
Final kinetic energy (E_p) (GeV)	1	3	16
Pulse rate (f_0) (Hz)	15	15	15
Protons/pulse ($n_B \times N_p$)	$40000 \times 3\ 10^9$	$4 \times 2.5\ 10^{13}$	$4 \times 2.5\ 10^{13}$
Length/circumference (m)	366 + 134	158	474
Emittance (95%, 6× rms) (πmm-mrad)	6	200	240
Dipole packing factor (1.3 T peak field)		0.39	0.575
Aperture (cm)		13	10
Tunes (ν_x, ν_y)		3.9, 2.4	9.4,4.9
Transition γ (γ_T)		7	25
RF parameters			
RF frequency (fRF) (MHz)	$201 \rightarrow 805$	6.6–7.4	7.4–7.5
RF harmonic		4	12
RF voltage/turn (MV)		0.2	1.2
RF length (m)		10	40

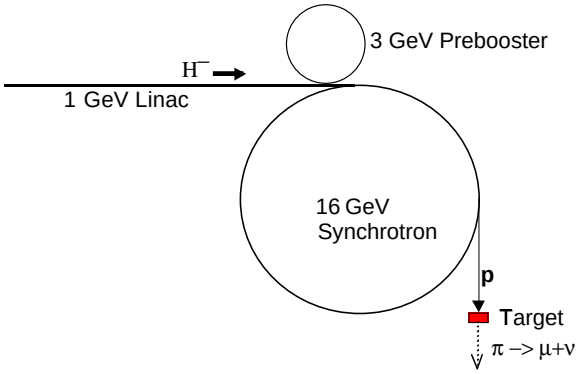

Fig. 2.1: Schematic view of a 16 GeV proton driver, with 1 GeV Linac, 3 GeV prebooster and 16 GeV synchrotron.

The beam power specifications of the baseline source ($\sim$ 4 MW) are similar to KAON factory and spallation neutron sources. However, GeV proton sources at 100 MW power levels (or higher) are being proposed for such applications as accelerator production of tritium and transmutation of radioactive waste. These sources could also be used as primary drivers of μ^+–μ^- colliders, and would permit significantly different scenarios; perhaps easing capture and cooling requirements and/or enabling higher luminosities (the reader is invited to explore the possibilities ...).

2.2 Sample proton driver scenario

Table 2.1 shows the parameters of a possible proton driver, which consists of a 1 GeV linac, a 3 GeV prebooster and a 16 GeV booster. The parameters are from a Fermilab-based plan for a multipurpose proton source upgrade (K–ν factory/μ-collider/Tevatron, etc.), which would replace the existing Fermilab booster [2, 3]. The linac is an extension of the present Fermilab linac (400 MeV) to higher energy in order to enable higher intensities in the succeeding rings. The linac would inject beam into a new prebooster which would capture beam into four bunches and accelerate them to $\sim$ 3 GeV, where they are transferred into a larger, higher energy booster for acceleration to 16 GeV extraction. The entire cycle would repeat at 15 Hz, with each of the rings cycling at that frequency, which also matches the existing Fermilab booster cycle. The circumference of the 16 GeV ring is also set to match that of the existing Fermilab booster, for maximal compatibility with the present Fermilab programme. However, it is felt that to enable very high intensities this new booster would have to be placed in a new booster tunnel. Thus, the Fermilab linac would be either extended from its current location or moved, and new (deeper and better shielded) prebooster and booster tunnels would be constructed.

The 1 GeV linac is based on the Fermilab 400 MeV linac, which consists of a 18 kV magnetron ion source which feeds a 0.75 MV Cockroft-Walton column, followed by a 100 MeV 201 MHz Alvarez linac, and a 300 MeV 805 MHz side-coupled linac. The upgrade requires a magnetron source which can provide 100 mA of beam in 250 μs pulses ($\sim 1.2 \times 10^{14}$ H^- ions). The beam would be captured into 201 MHz buckets and then accelerated to 100 MeV, where they are captured within 805 MHz buckets and accelerated to $\sim$ 1 GeV. The additional 600 MeV of 805 MHz linac is an extension of the existing Fermilab 805 MHz linac, using $11^{1/2}$ additional side-coupled modules (131.3 m). The total linac length is $\sim$ 500 m.

The H^- ions are multiturn injected at 1 GeV through a foil stripper into the 1–3 GeV prebooster (500 turns), where they are captured in 6.64 MHz buckets and accelerated as four bunches of 2.5×10^{13} protons to 3 GeV in 33 ms. The prebooster would have a circumference of 154 m (one-third of the existing Fermilab booster).

The four bunches are then transferred into matched buckets in the high-energy booster for acceleration to full energy (16 GeV). At full energy, the bunches are compressed to minimal lengths ($\sigma_z \sim 0.3$ m) and extracted to the π-production target. The ring circumference is matched to that of the existing Fermilab booster for compatibility with existing Fermilab accelerators.

A key limitation is transverse space charge and the design goal is to keep the space-charge tune-shift $\delta\nu = \mathrm{r_p N}/\ (4\epsilon_\mathrm{n}\beta\gamma^2 \mathrm{B})$ less than $\sim$ 0.25–0.4 throughout the cycle, where r_p is the classical proton radius, N is the number of protons, B is the bunching factor (B is the ratio of average to peak current), and ϵ_n is the normalized rms emittance. Space charge $\delta\nu$ is minimized by choosing higher injection energies, larger emittances, and larger B. The injection kinetic energy is 1 GeV, which sets $\beta\gamma^2$ at the relatively large value of 3.75. ϵ_n is increased above the linac value of $\sim$ 1 mm-mrad to $\sim$ 33 mm-mrad (rms) by painting the beam across the foil in multiturn injection. B is conservatively set at 0.25 at injection by longitudinal painting into the four RF buckets of the prebooster, which is initially filled so that each of the four bunches is relatively long (large B). The beam bunch lengths decrease as the beam accelerates (decreasing B while $\beta\gamma^2$ increases), and the beam is transferred into the larger ring at 3 GeV. The four bunches from the prebooster occupy only four buckets of the $h = 12$ booster.

The beam transports of both rings consist of rapid-cycling separated-function magnets. The peak dipole field is set at 1.3 T in both lattices, and the transition energy ($\gamma_\mathrm{t} \mathrm{m_p} c^2$) is set above extraction so that the beams are always below transition, which avoids instabilities due to 'negative mass' and at transition crossing, and maintains a stable natural chromaticity. The high-γ_t is obtained by use of a 'flexible-momentum-compaction' lattice, which gives a tuneable γ_t [4]. Figure 2.2 shows a possible lattice configuration. The large emittances imply large apertures (13 cm for the 3 GeV ring and 10 cm for the 16 GeV ring). To minimize eddy currents from rapid-cycling, a high-impedance beam pipe using Inconel or ceramic with conducting wires/strips is needed.

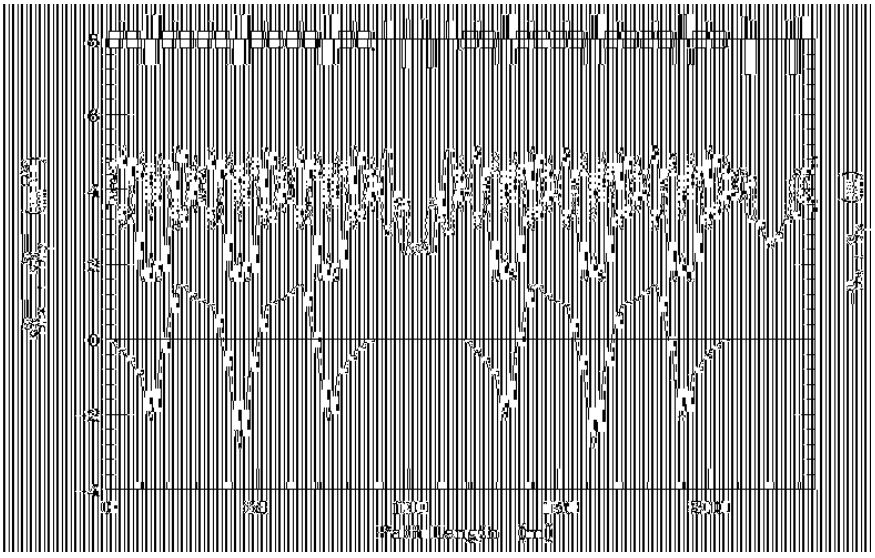

Fig. 2.2: Lattice for a proton source (half of ring is shown).

2.3 Proton driver RF systems

Griffin has developed an acceleration scenario with RF system designs for each ring [5]. The RF cavities are 1 m long units with ceramic accelerating gaps and metal-alloy tape-wound cores, with outboard inductive tuners containing NiZn ferrite rings with bias current windings for tuning from 6.6 to 7.4 MHz during the acceleration (see Fig. 2.3). Power amplifiers for cavity excitation and transient beam loading compensation are coupled directly to the accelerating gaps. Ten such cavities can generate up to 200 kV in the prebooster, and 40 cavites can produce 1.5 MV in the booster. Bunches injected with $\sim$ 100 ns full-width in the prebooster are compressed to $\sim$ 20 ns after booster acceleration, and rotated to $\sim$ 6 ns ($\sigma_{\rm rms} \cong 1$ ns and δE $= \pm 200$ MeV) at booster extraction. An inductive insert to cancel space charge is helpful in the final compression. Simulations of this acceleration and bunching have been performed [6], [7].

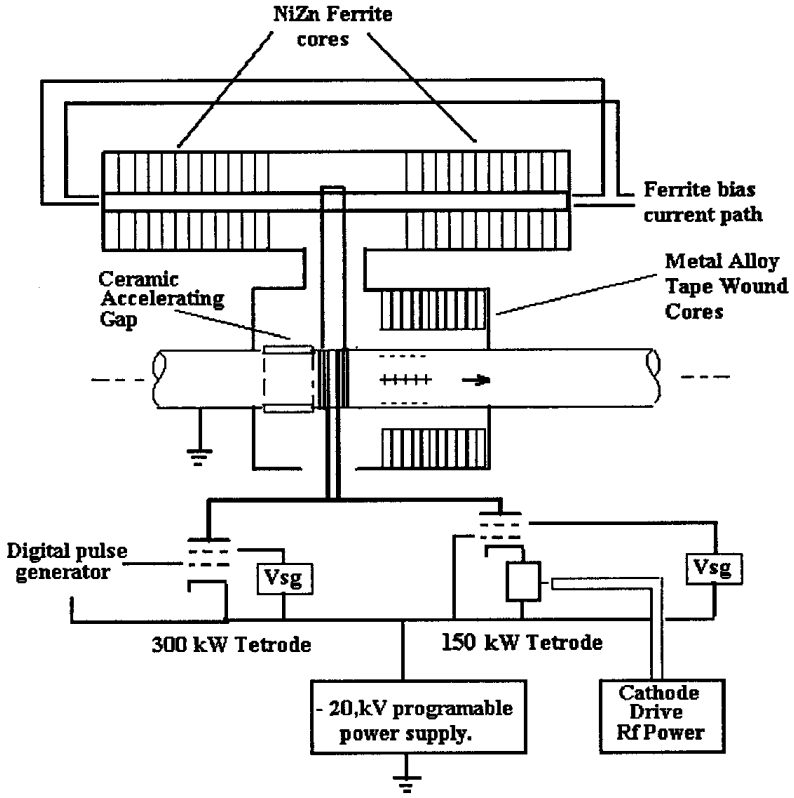

Fig. 2.3: Radio frequency cavity system for proton source.

2.4 Proton driver design report

A design study group led by W. Chou has been formed at Fermilab to develop a detailed design of a proton driver, based on the concepts discussed above. A conceptual design report is due in October 2000 [8]. The Fermilab proton driver is a dual-purpose machine, which will provide higher intensity beams for the existing hadron programme, while also providing the basis for a future muon storage ring and collider programme.

The Fermilab driver has some constraints specific to matching to Fermilab facilities. The driver circumference is matched to the existing 8 GeV booster circumference (for matching into the Main Injector) and that limits the maximum energy to $\sim$ 16 GeV.

2.5 Instability considerations

The required high intensities, and particularly the high peak intensities associated with the short bunch lengths of the extracted beams, present possibilities of high-intensity instabilities. Ng and Qian [9] have initiated discussion of instability considerations for the driver rings. A key consideration is space charge, where the transverse space charge tune shift is given by:

$$\Delta\nu = -\frac{3\mathrm{N}\mathrm{r_p}}{2\beta\gamma^2\epsilon_{\mathrm{N,F}}\mathrm{B}}$$

where B is the bunching factor (average current/peak current), and $\epsilon_{\mathrm{N,F}}$ is the Fermilab full emittance (95% normalized emittance). The operational strategy is to control the bunch length through the cycle such that $\Delta\nu$ is always less than 0.4 (or, preferably, 0.25) so that the beam always remains below the space charge limit.

Impedance driven instabilities are also considered. The beam is always below transition, which should improve stability. Space charge impedances place the beam near stability thresholds, and it is therefore considered desirable to introduce an inductive impedance to cancel the space charge impedance. This can be done by adding a hollow cylinder of ferrite of length L about the beam pipe, which would have an impedance of :

$$\frac{\mathrm{Z_L}}{\mathrm{n}} = -\mathrm{i}\frac{\mathrm{Z}_0\omega_0}{2\pi\mathrm{c}}\mu\mathrm{L}\ \ln(\mathrm{d/b})$$

with μ the ferrite permeability, and d and b are the inner and outer radius of the ferrite. The ferrite length can be chosen to cancel the longitudinal space charge, reducing the effective impedance, but also enabling a reduction in the RF voltage needed to confine the beam.

2.6 Proton driver experiments

Some critical experiments to test elements of the proton source design have been performed.

At the BNL AGS, experiments in bunching the beam near transition were performed, at parameters similar to the post-acceleration bunching of the proton source. The rms bunch length of 3 MHz, 8 GeV bunches was reduced from 6.7 to 2.1 ns by a phase-space rotation just below transition [10]. Bunching below transition avoids the longitudinal emittance increase caused by mismatches and instabilities with transition crossing, and therefore permits bunching to shorter lengths. The results support the proposition that initially long proton bunches can be accelerated and then compressed to ns lengths, as is required for the μ^+–μ^- collider. The bunching experiment was performed at only moderate intensities ($\sim 3 \times 10^{12}$ protons/bunch), larger intensities were not then available. The experiments will be repeated at higher intensities in the future.

At higher intensities, space charge debunching will increase and may cause phase space dilution. Reduction of space charge by addition of a cancelling inductive impedance may be possible. A set of inductive ferrite modules was placed in the LANL Proton Storage Ring. Longitudinal space charge effects were reduced without generating instability, and the results support the use of inductive inserts to cancel space charge [11]. Experiments at the KEK proton synchrotron have also established the value of an inductive insert to cancel space charge impedance [12].

These experiments will be extended in the future, with higher intensity bunching below transition in the AGS, and with higher intensity test of space charge cancellation. Other experiments on the proton driver concept will be developed. One of these is the development and testing of prototype RF cavity systems.

2.7 Other proton driver systems

The present system is neither the only nor the optimum possible proton driver system. A proton driver system based on use of the BNL AGS has also been suggested [13]. A schematic view of the upgrade programme is shown in Fig. 2.4. The AGS presently produces 6×10^{13} protons in 8 bunches at 25 GeV and 0.6 Hz, and could be increased to 10^{14} per pulse. A 2.5 GeV accumulator ring in the AGS tunnel and an AGS power-supply upgrade to 2.5 Hz operation, which would match the repetition rate to a fourth of the 10 Hz rate of the existing (1/4-size) booster, would generate 1 MW of beam power. With an additional upgrade of the BNL linac from 200 MeV to 600 MeV, an intensity of 2×10^{14} protons per pulse in four bunches of 5×10^{13} at 25 GeV and 2.5 Hz could be reached, raising the power to 2 MW. Other options, such as a further upgrade to 5 Hz operation, could reach the 4 MW level of the previously described new proton source. A key difficulty in this particular upgrade option is the fact that the existing BNL AGS accelerator lattice crosses transition, with relatively large emittance dilution in that process. Lattice modifications to avoid transition crossing may be needed.

A proton driver system based on CERN facilities could be developed, and may be similar to the AGS adaptation, because of the similarities between the CERN PS and the AGS.

Proton driver systems based on 1–2 GeV linacs, such as those used for spallation neutron sources, could also be used, if of sufficient power (see Fig. 2.5). Compressor rings and arcs to form short bunches on targets would be desired; and the lower energies of the initial pions could imply a somewhat different collection and cooling system.

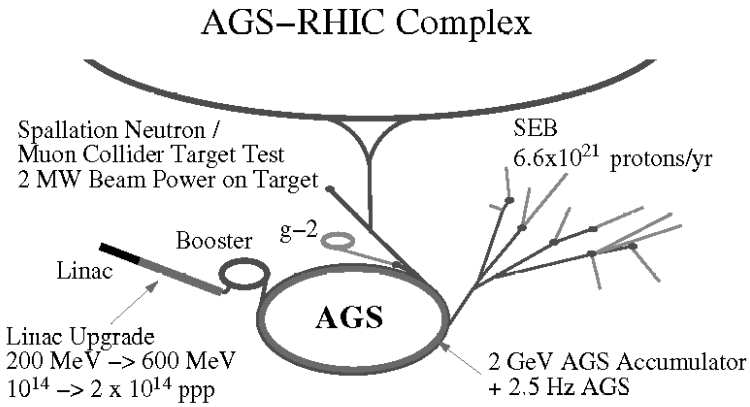

Fig. 2.4: Overview of plans to upgrade the BNL AGS system to 2 MW beam or more. A linac upgrade will allow more beam per bunch, and the AGS cycling rate will be increased to 2.5 Hz or more.

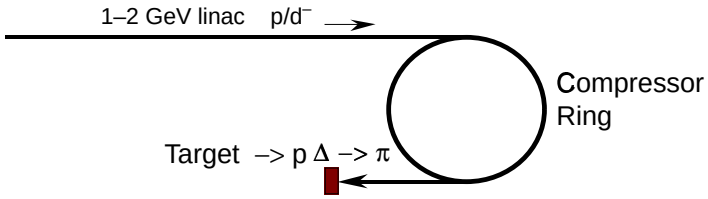

Fig. 2.5: Schematic view of a $\pi \rightarrow \mu$ source based on a 1–2 GeV linac and compressor ring.

References

[1] KAON Factory Study, Accelerator Design Report, TRIUMF, Vancouver BC, Canada (1990).

[2] C. Ankenbrandt, 'Design Concepts for a Novel Fermilab Superbooster', Fermilab-FN-650, November 1996.

[3] S.D. Holmes, ed., 'A Development Plan for the Fermilab Proton Source', Fermilab-TM-2021 (1997).

[4] S.Y. Lee, K.Y. Ng and D. Trbojevic, Phys. Rev. **E48**, 3040 (1993).

[5] J. Griffin, 'RF System Considerations for Muon Collider Proton Driver Synchrotrons', FN-669, (1998).

[6] K.Y. Ng, 'Some issues on the RF system in the 3 GeV Fermilab pre-booster', AIP Conf. Proc. **448**, 178 (1998).

[7] I. Kourbanis and Z. Qian, unpublished (1998).

[8] W. Chou et al., unpublished (1999).

[9] K.Y. Ng and Z. Qian, 'Space-charge effects of the proposed high-intensity Fermilab booster', AIP Conf. Proc. **435**, p. 841 (1998).

[10] C. Ankenbrandt et al., 'Bunching near transition in the AGS', Phys. Rev. Special Topics AB 1, 030101 (1998).

[11] J.E. Griffin et al., 'Passive Compensation of Space Charge in the LANL PSR', FN-661 (1998).

[12] C. Ohmori et al., *Proc. 1999 PAC*, New York, (New York, 1999); K. Koba et al., *Proc. 1999 PAC*, New York, (New York, 1999).

[13] T. Roser, in *Workshop on Space Charge Physics in High-Intensity Hadron Rings*, AIP Conf. Proc. **448**, 135 (1998).

3 π PRODUCTION AND μ CAPTURE

3.1 Introduction

The purpose of the production target and subsequent transport is to produce the maximum number of muons which can subsequently be accepted and cooled into collider bunches. For this purpose, the proton beam from the proton source must be optimally focused onto a production target and the beam optics must be arranged to capture the maximal number of pions from that source and confine them within a transport for $\pi \rightarrow \mu$ decay.

A number of options for the target, the π-capture optics, and the $\pi \rightarrow \mu$ decay transports have been studied [1]–[6]. The proton beam energies were varied from GeV to $\sim$ 100 GeV levels, and low to high Z target materials have been considered. From these studies it appears that an optimum scenario for producing forward π's for μ-collection is to use a high power 10–30 GeV proton beam on a relatively high-Z, high-density target, and capture the p's downstream from the target in a high-acceptance transport, which is based on solenoidal focusing with a low-frequency RF-bunching system.

3.2 π production and capture

For the capture optics, Li lenses, magnetic horns, quadrupole lenses, and high-field solenoids have been considered [7]. While the other approaches are possible (and may be preferable in variant scenarios), the fact that most of the pions are produced at relatively low energies ($\sim$ 100–500 MeV), and with relatively large transverse momenta ($\sim m_\pi c$), has made the choice of solenoid focusing relatively attractive.

From recent studies, maximal capture is obtained by immersing the production target in a high-field solenoid ($B_z = B_0$). Pions produced in the solenoid follow helical orbits downstream from the target. In the transverse projection, these orbits are circular and originate at the target (centre of the magnet). The orbits have a radius $r_\perp = p_\perp/(eB_0)$ or $B\rho_\perp/B_0$ and are centred a distance $r_\perp$ transverse to the target, where $p_\perp$ is the π transverse momentum. The radius R of the capture solenoid circumscribes accepted orbits, and the criterion for accepted orbits is:

$$p_\perp < \frac{eRB_0}{2}$$

A $B_0 = 20$ T solenoid with R = 7.5 cm radius has a transverse acceptance of $p_\perp = 225$ MeV/c, and accepts most of the π's produced from the target. The target solenoid is followed by a solenoid transport in which the magnetic field is adiabatically reduced, while the radius is increased. This transport accepts most of the low-energy μ's ($\sim$ 100–600 MeV/c) produced by π-decay (see Fig. 3.1).

Simulations of π-production as a function of proton energy, target material and geometry within a capture geometry have been performed, using Monte Carlo codes such as MARS [8] (and DPMJET [9] and ARC [10]) and these codes have been verified by comparison with experiments, particularly the recent pion production experiment 910 at BNL [11]. Figure 3.2 shows some of the results of MARS simulations. They show that the target should be $\sim$ 2–3 interaction lengths of a high-density, relatively high-Z material. Optimal proton energy is in the 10–30 GeV range. p-capture was found to be maximal with longitudinal momentum acceptance centered at $p_z \cong 250$ MeV/c. A target radius of $\sim$ 1 cm appears optimal, maximizing secondary production while minimizing absorption. Tilting the target (with respect to the magnetic field) by 100–150 mrad was found to improve acceptance somewhat, by minimizing reabsorption of the low-energy π's, which follow helical trajectories through the magnetic region.

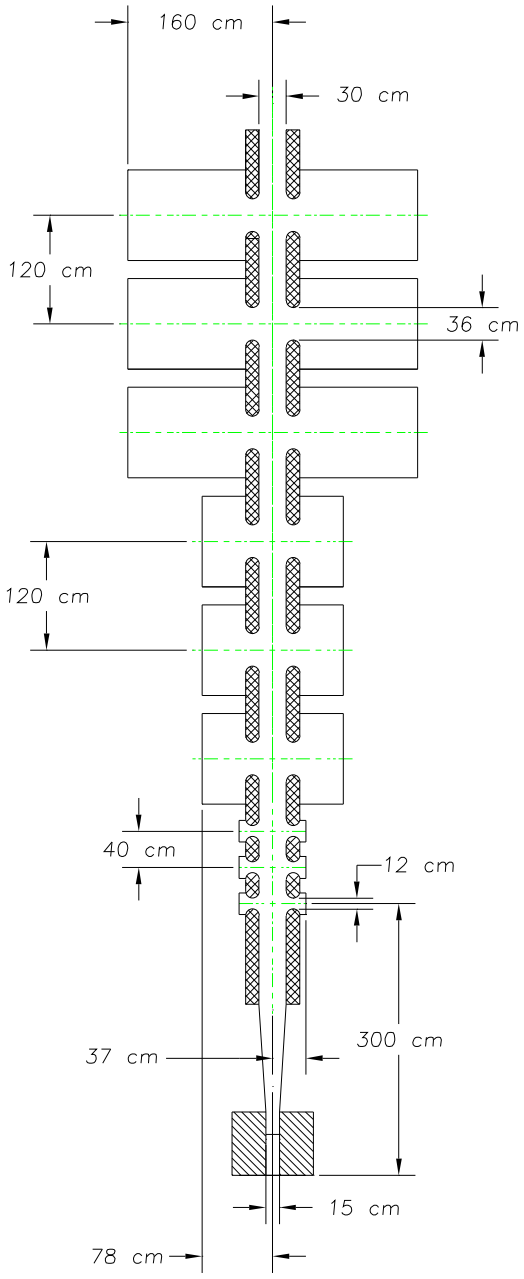

Fig. 3.1: Schematic view of pion production, capture and initial phase rotation. A pulse of 16 GeV protons is incident in a skewed target inside a high-field solenoid magnet followed by a decay and phase rotation channel.

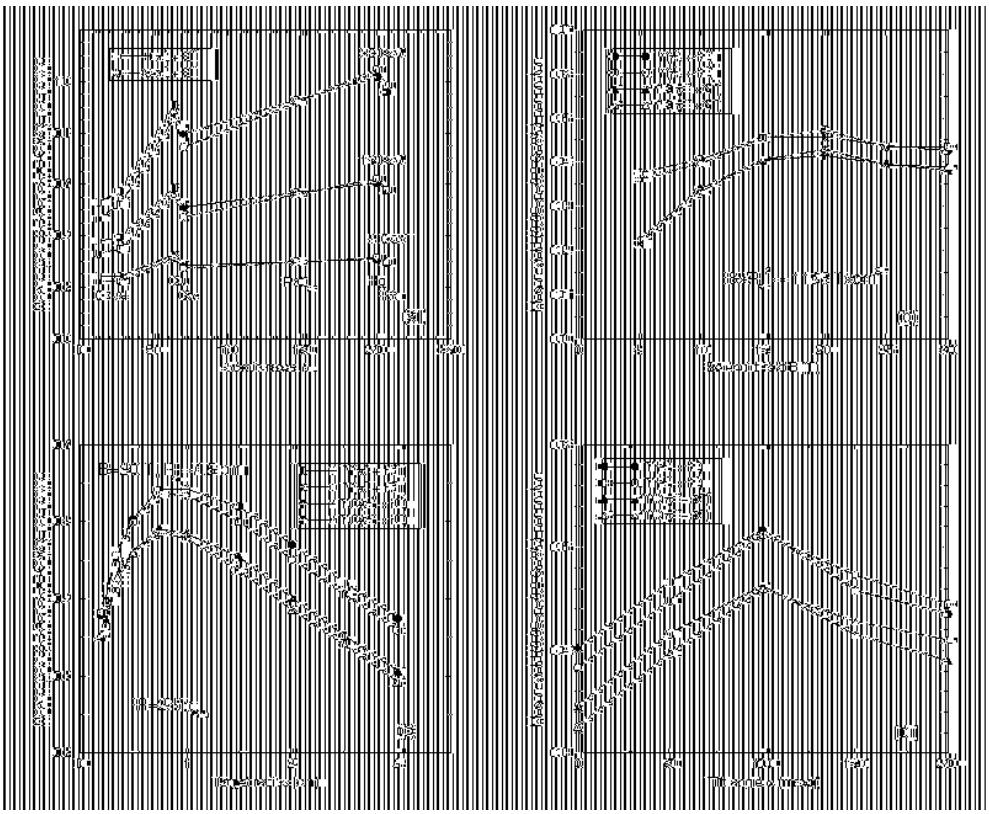

Fig. 3.2: Meson yield (π + K) from different targets tilted by an angle α in a solenoidal field B_0 of aperture R_a as calculated using the MARS13 (98) code [8], [12]. The target is aligned along the beam. The curves labeled Y are initial yield at the target, the curves labeled YC show mesons that are transported into the decay channel. In both cases a momentum acceptance window ($0.05 < p < 0.8$ GeV/c) is set, corresponding to the acceptance of the RF rotation. (a) Yield from a 1.5 interaction lengths, 1 cm radius target irradiated with 8, 16, and 30 GeV proton beams with $\sigma_x\sigma_y = 4$ mm as a function of target material atomic mass ($B_0 = 20$ T, $R_a = 7.5$ cm, $\alpha = 0$). (b) Yield from a 3 interaction length, 1 cm radius Ga target with 16 GeV proton beam at $\alpha = 150$ mrad versus solenoid field B_0 ($B_0R_a^2$ kept constant). (c) Yield as a function of target radius in a 16 GeV proton beam ($B_0 = 20$ T, $\alpha = 100$ mrad, $R_a = 7.5$ cm). (d) Yield vs tilt angle α of the target and beam (with respect to magnet centre).

3.3 Target considerations

About 400 kW of energy is deposited in the target and handling that is a serious problem. Cooling with a thermal bath would lead to large p-absorption, and thermal radiation is insufficient. Therefore the target must move so as to carry the energy deposited by the proton beam out to an external heat exchanger. Both moving solid metal and flowing liquid jet targets are under consideration. A liquid is relatively easy to move and cool. A liquid flowing in a pipe is a possibility, but experience and simulations indicate that the short proton pulses could lead to shock damage to the pipe. An open liquid jet is proposed [13].

Liquid mercury jets have been demonstrated, but without beam [14]. Low melting point lead and gallium alloys are also being considered, and are being studied to determine the effects of pulsed beam heating. It is expected that the liquid will be dispersed by the beam, which implies that the target section must be able to handle and collect the dispersed liquid. The targets operate in a strong magnetic field, and strong eddy currents are expected in conducting liquid jets, causing reaction forces that may disrupt its flow. Jets of nonconducting material may then be preferred.

Moving solid targets are also under consideration. A moving cable or 'band-saw' target [15] is possible, with the target supported and moved by rollers through the target station; mechanical design difficulties are a concern. Construction and testing of potential targets is an important goal of the collaboration targetry experiment at BNL [16]. The initial investigations will include building and testing liquid metal jet targets (see Chapter 8).

3.4 $\pi \rightarrow \mu$ decay and RF rotation

Following the target, the magnetic field is adiabatically decreased and the beam size is increased, following $\mathrm{Br}^2 = \text{constant}$, to B = 5–1.25 T (r = 15–30 cm). This scaling follows 'Busch's theorem' (from the conservation of canonical angular momentum), which implies that the particles follow helical orbits such that the parameter $\mathrm{B(s)\,r_\perp(s)^2}$ remains constant.

An RF system within that decay transport reduces the energy spread by 'RF rotation', in which the faster particles decelerate while slower ones accelerate. This transforms the short-bunch beam on target producing a large momentum spread in μ's to a longer μ bunch with reduced δp/p. Table 3.1 shows parameters of a sample RF rotation segment. The magnetically confined transport continues through a sufficient length for π decay. This transport also contains a multiharmonic $\sim$ 30–150 MHz RF system embedded in a short-period solenoid transport. Studies of RF rotation section solutions with lengths of 40–80 m containing a total of 200–500 MV of RF cavities have been developed. In the simulations, up to $\sim$ 0.35 μ's (of one sign)/proton are captured from 16–30 GeV protons within an acceptance window of a bunch length of $\sim$ 6 m and δE $\sim \pm 100$ MeV. This is roughly a third of the number of initially produced π's [1,2,17,18,19]. Energy selection in the m decay can be used to select a relatively high polarization in the μ beams [19].

Significant problems exist in designing the RF and focusing system, since it requires the combination of large low-frequency, relatively high-gradient cavities with relatively high-field superconducting solenoids. Several design iterations have been considered; a recent one (see Fig. 3.1) uses low-field 1.25 T magnets completely outside the cavities; a previous one uses 5 T magnets placed in the cavity irises.

Table 3.1
Parameters of a μ collection phase-rotation linac

Linac	Length (m)	Frequency (MHz)	Gradient (MV/m)
1	3	60	5
2	29	30	4
3	5	60	4
4	5	37	4

An experiment is proposed at the AGS on targetry related issues, which will test some of these systems [16]. It would include tests of liquid jet and other targets, placed within magnets, and then with beam, measuring p production. An RF cavity with solenoid would be added to test RF rotation components.

3.5 Other target/production options

One variation that may result in some improvements, is the use of a deuteron (or triton) beam [20]. The space charge in the beam is reduced by a factor of 2 (or 3) per nucleon, which may make it easier to accelerate and bunch to higher intensities. Also the neutron(s) in the projectile should result in relatively more π^- in the final state.

The low frequencies for the RF systems are rather difficult to obtain at the high gradients and total power requirements presently expected. Schemes which use higher frequency RF

systems, forming the initial muon distribution into a train of bunches, and then recombining them, are also being considered [21]. Some difficulties are expected in obtaining comparable acceptances, and the large apertures needed for transverse acceptance are more difficult with high-frequency RF.

As discussed in the previous chapter, the option of pursuing low-energy π production using a ~ 1 GeV proton beam could also be explored, and may be more efficient (in π's per MJ), and would be better matched to low-energy cooling options.

3.6 Polarization options

Use of polarized muon beams could provide important advantages over unpolarized cases, since some significant physics signals depend upon polarization states, while background events are typically unpolarized. In the center of mass of the decaying pion, the outgoing muon is fully polarized (-1 for μ^+ and $+1$ for μ^-). In the lab system the polarization depends upon the decay angle $\theta_{\rm d}$, boosted to the lab energy. The kinematics of the decay and capture transport favor the natural polarization, with residual polarizations of $\sim 20\%$ in each beam, in simulations of the capture transports described above.

Higher polarization is possible by energy selection of the captured decay muons. For higher polarization, selection of muons from forward π decays is required ($\cos\theta_{\rm d} \rightarrow 1$). In Fig. 3.3, the polarization is marked by the symbols +, o, and $-$, which imply $\{{\rm P} > 1/3,\ -1/3 < {\rm P} < 1/3,\ {\rm P} < -1/3\}$, respectively, and a correlation between energy and polarization can be identified. If a selection on the final accepted muon energy is made, the polarization can be increased, but at a cost in muon capture rate, and in the resulting μ^+–μ^- collider luminosity. Figure 3.3 displays the resulting correlation between luminosity and polarization. Initial proton beam intensity would have to be increased to avoid a loss of muon intensity with increased polarization.

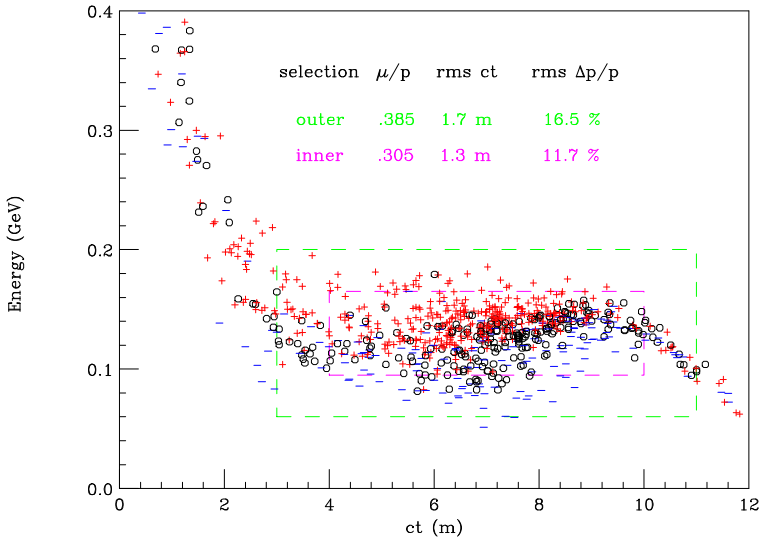

Fig. 3.3: Muon distribution in energy and ct at the end of a phase-rotation channel, as determined using the program MUONMC. The symbols +, o and $-$ denote muons with polarization ${\rm P} > 1/3$, $1/3 > {\rm P} > -1/3$, and ${\rm P} < -1/3$, respectively.

The polarization obtained by energy selection in the decay channel can be maintained through ionization cooling and acceleration. As described by Norum and Rossmanith [22], the spin flip probability P_S in ionization-cooling energy loss from passing through material is:

$$P_S = \int \frac{m_e}{m_\mu} \beta_\nu^2 \frac{dE}{E}$$

where $\beta_v = v/c$, dE/E is the fractional energy loss due to ionization and m_e, m_μ are the electron and muon rest masses. In our case this integrates to $\sim$ 10–20% loss in polarization through the cooling channel (twice the spin-flip probability). That loss is included in Fig. 3.4.

During circulation in any ring (accelerator or collider) the muon spin will precess by $(g-2)/2\gamma = 1.166\times10^{-3}/\gamma$ turns per revolution, and the energy spread will introduce variations in the precession. However, if the particles remain in the ring for an exact integer number of synchrotron oscillations, then no dilution occurs. (The width of the energy spread will vary the precession, however.) In the collider the spin can be rotated into the longitudinal direction at the IRs. However, this would complicate the collider beam optics.

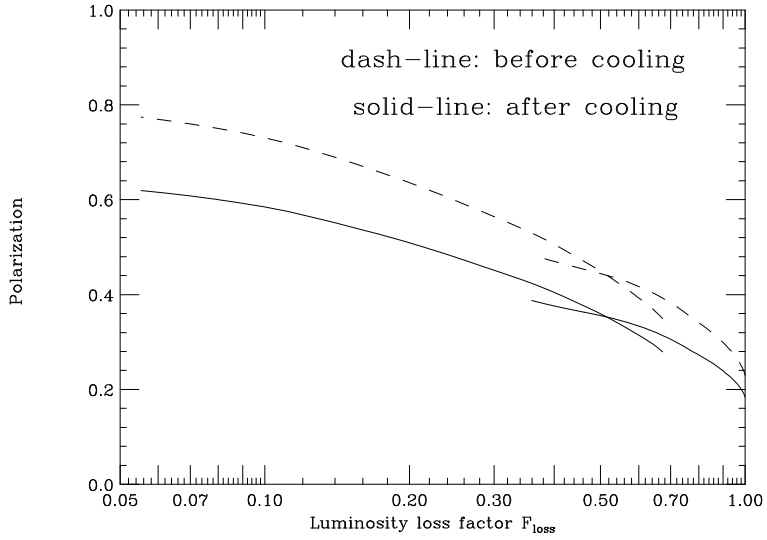

Fig. 3.4: Luminosity as a function of muon polarization, where polarization is enhanced by energy selection in the capture channel. (Discontinuity comes from switching from two to one bunch (per beam) collisions.)

References

[1] $\mu^+\mu^-$ Collider - A Feasibility Study, BNL-52503, Fermi-Lab-Conf.-96-092, LBNL-38946 (1996), presented at the *Snowmass 96 Workshop* (1997).

[2] Muon Collider Collaboration, 'Status of Muon Collider Research and Development and Future Plans', BNL 65623, Fermilab-PUB-98-179, LBNL-41935, submitted to Phys. Rev. Special Topics AB (1999).

[3] N.V. Mokhov, R. Noble and A. Van Ginneken, *Proc. Montauk Workshop*, AIP Conf. Proc. **372**, p. 61 (1996).

[4] N.V. Mokhov and A. Van Ginnekin, 'Target and Collection Optimization for Muon Colliders', Fermilab-Conf-98/041, AIP Conf. Proc. **441**, p. 320 (1998).

[5] D. Ehst, N.V. Mokhov, R.J. Noble and A. Van Ginneken, 'Target Options and Yields for a Muon Collider Source', *Proc. PAC 1997*, Vancouver, BC, p. 393 (1997).

[6] H. Takahashi, Y. An, X. Chen, and M. Nomura, *Proc. PAC 1997*, Vancouver, BC, p. 402 (1997).

[7] R.C. Fernow et al., AIP Conf. Proc. **352**, p. 134 (1996).

[8] N.V. Mokhov, The MARS Code System Users Guide, Fermilab FN-628 (1995).

[9] J. Ranft, DPMJET version II.3 and II.4, INFN-AE-97045 (1997).

[10] D. Kahana and Y. Torun, BNL-61983 (1995).

[11] Experiment 910 at BNL-AGS (1997).

[12] N.V. Mokhov and A. Van Ginneken, FNAL-Conf-98/041 (1998); N.V. Mokhov and S.I. Striganov, FNAL-Conf-98/053 (1998).

[13] C. Lu and K.T. McDonald, Princeton/$\mu\mu$/97-3 (1997) and Princeton/mm/98-10 (1998).

[14] C. Johnson, 'Solid and Liquid Targets Overview' unpublished, CERN, (1998).

[15] B.J. King, S. Moser, R.J. Weggel and N.V. Mokhov, paper THP58, *Proc. 1999 PAC*, New York, p. 3041, (New York, 1999).

[16] BNL targetry experiment proposal (1998).

[17] D. Neuffer and A. Van Ginneken, FNAL Pub 98-296, to be published in Nucl. Instrum. Methods A (1998).

[18] W. Turner and H. Kirk, *Proc. New Directions for HEP*, Snowmass 96, p. 242 (1996).

[19] R. Palmer and J. Gallardo, unpublished (1997).

[20] A. Van Ginneken, 'Deuterons or Tritons for Muon Collider Driver', Fermilab-FN-647 (1998).

[21] R. Palmer, N. Holtkamp et al., unpublished (2000).

[22] B. Norum and R. Rossmanith, Nucl. Phys. B (Proc. Suppl.) **51A**, 191 (1996).

4 MUON COOLING

4.1 Principles

In ionization cooling (muon cooling), particles pass through a material medium and lose energy (momentum) through ionization interactions, and this is followed by beam reacceleration in RF cavities (Fig. 4.1). The losses are parallel to the particle motion, and therefore include transverse and longitudinal momentum losses; the reacceleration restores only longitudinal momentum. The loss of transverse momentum reduces particle emittances, cooling the beam. However, the random process of multiple scattering in the material medium increases the rms beam divergence, adding a heating term which must be controlled in a complete cooling system. This cooling method is not very practical for protons, which would have frequent nuclear interactions, or electrons, which would have bremsstrahlung, but is practical for muons, and cooling rates compatible with muon lifetimes are possible.

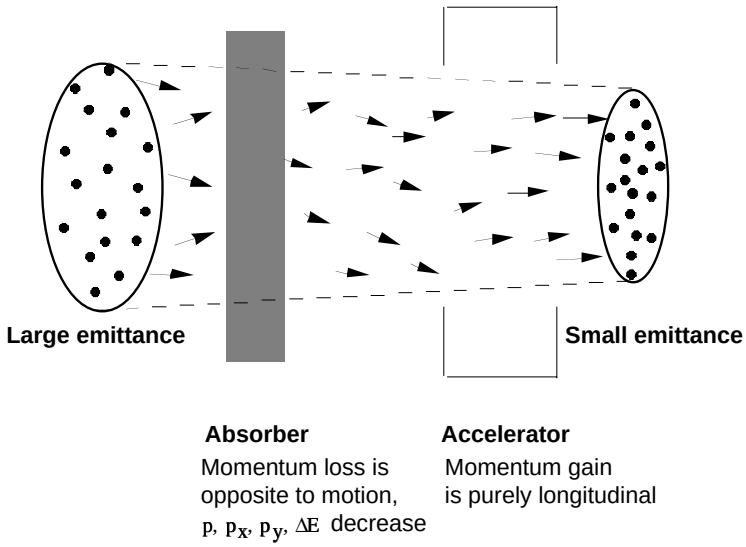

Fig. 4.1: Concept of ionization cooling.

The differential equation for rms transverse cooling is [1]–[5]:

$$\frac{\mathrm{d}\epsilon_\mathrm{N}}{\mathrm{ds}} = -\frac{1}{\beta^2\mathrm{E}}\frac{\mathrm{dE}}{\mathrm{ds}}\epsilon_\mathrm{N} + \frac{\beta\gamma\beta_\perp}{2}\frac{\mathrm{d}\langle\theta^2_\mathrm{rms}\rangle}{\mathrm{ds}} = -\frac{1}{\beta^2\mathrm{E}}\frac{\mathrm{dE}}{\mathrm{ds}}\epsilon_\mathrm{N} + \frac{\beta_\perp \mathrm{E_s^2}}{2\beta^3\mathrm{m}_\mu\mathrm{c}^2\mathrm{L_R E}} \tag{4.1}$$

where the first term is the energy-loss cooling effect and the second is the multiple scattering heating term. Here ϵ_N is the normalized emittance, E is the beam energy, $\beta = \mathrm{v/c}$ and γ are the usual kinematic factors, dE/ds is the energy loss rate, θ_rms is the rms multiple scattering angle, $\mathrm{L_R}$ is the material radiation length, $\beta_\perp$ is the betatron function, and $\mathrm{E_s}$ is the characteristic scattering energy ($\sim$ 13.6 MeV) [6]. [The normalized emittance is related to the geometric emittance $\epsilon_\perp$ by $\epsilon_\mathrm{N} = \epsilon_\perp/(\beta\gamma)$, and the beam size is given by $\sigma_\mathrm{x} = (\epsilon_\perp\beta_\perp)^{1/2}$.]

The equation for longitudinal cooling with energy loss is:

$$\frac{\mathrm{d}\sigma^2_\mathrm{E}}{\mathrm{ds}} = -2\frac{\partial\frac{\mathrm{dE}}{\mathrm{ds}}}{\partial\mathrm{E}}\sigma^2_\mathrm{E} + \frac{\mathrm{d}\langle\Delta\mathrm{E}^2_\mathrm{rms}\rangle}{\mathrm{ds}} \tag{4.2}$$

in which the first term is the cooling term and the second is the heating term caused by random fluctuations in the particle energy. Beam cooling can occur if the derivative $\partial(\mathrm{dE/ds})/\partial\mathrm{E} > 0$.

This energy loss can be estimated by the Bethe–Bloch equation [6]:

$$\frac{dE}{ds} = 4\pi N_A r_e^2 m_e c^2 \rho \frac{Z}{A}\left[\frac{1}{\beta^2}\ln\left(\frac{2m_e c^2\gamma^2\beta^2}{I}\right) - 1 - \frac{\delta}{2\beta^2}\right] \tag{4.3}$$

where N_A is the Avogadro constant, ρ, A and Z are the density, atomic weight and number of the absorbing material, m_e and r_e are the mass and classical radius of the electron, ($4\pi N_A r_e^2 m_e c^2 = 0.3071$ MeV cm^2/gm). The ionization constant I is approximately 16 $Z^{0.9}$ eV, and δ is the density effect factor which is small for low-energy μ's. (We have used $\delta = 0$ in initial rms evaluations.) The energy loss as a function of p_μ is shown in Fig. 4.2. The derivative is negative (or naturally heating) for $E_\mu < \sim 0.3$ GeV, and is only slightly positive (cooling) for higher energies.

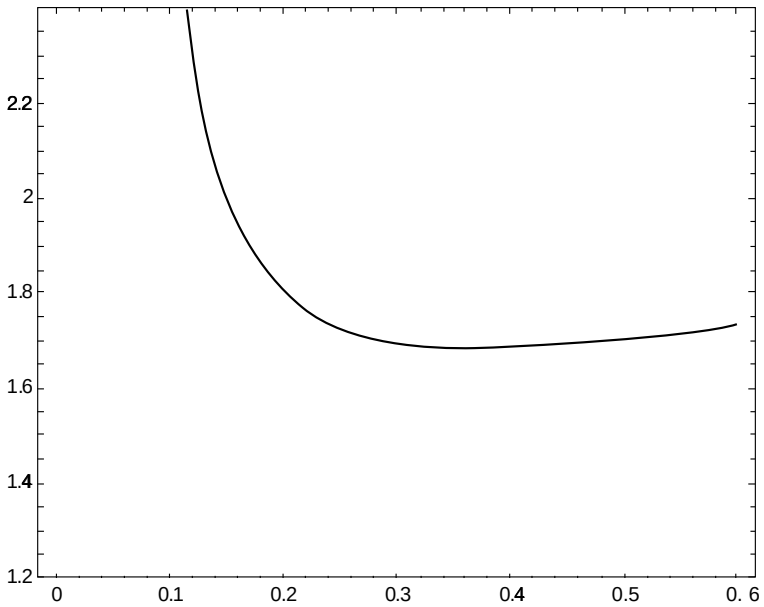

Fig 4.2: (dE/dx)/ρ [(MeV/(gm/cm^2)] as a function of muon momentum P_μ for Li. Note that this function is heating (negative slope) for $P_\mu < \sim 0.350$ GeV/c and becomes strongly heating (steep slope) for $P_\mu < 0.200$ GeV/c.

In the long-pathlength Gaussian-distribution limit, the second term in Eq. (4.2) is given approximately by [7]:

$$\frac{d\langle\Delta E_{rms}^2\rangle}{ds} = 4\pi(r_e m_e c^2)^2 n_e \gamma^2\left(1 - \frac{\beta^2}{2}\right) \cong 0.157\rho\frac{Z}{A}\gamma^2\left(1 - \frac{\beta^2}{2}\right)\ (\text{MeV})^2\text{cm}^2/\text{gm} \tag{4.4}$$

where n_e is the electron density in the material ($n_e = N_A\rho Z/A$). This expression increases rapidly with higher energy (larger γ), opposing the cooling process. After adding this energy straggling, ionization cooling does not naturally provide adequate longitudinal cooling.

4.2 Emittance exchange

However, the cooling term can be enhanced by placing the absorbers where transverse position depends upon energy (nonzero dispersion) and where the absorber density or thickness also depends upon energy, such as in a wedge absorber [8] (see Fig. 4.3). In that case the cooling derivative can be rewritten as:

$$\frac{\partial\frac{dE}{ds}}{\partial E} \Rightarrow \left.\frac{\partial\frac{dE}{ds}}{\partial E}\right|_0 + \frac{dE}{ds}\frac{\eta\rho'}{\beta cp\rho_0} \tag{4.5}$$

where ρ'/ρ_0 is the relative change in density with respect to transverse position, ρ_0 is the reference density associated with dE/ds, and η is the dispersion [$\eta = \mathrm{dx/d}(\Delta \mathrm{p/p})$]. Increasing the longitudinal cooling rate in this manner decreases the transverse cooling by the same amount. The transverse cooling term is changed to:

$$\frac{\mathrm{d}\epsilon_\mathrm{N}}{\mathrm{ds}} = -\frac{1}{\beta^2 \mathrm{E}} \frac{\mathrm{dE}}{\mathrm{ds}} \left(1 - \frac{\eta \rho'}{\rho_0}\right) \epsilon_\mathrm{N} \ . \tag{4.6}$$

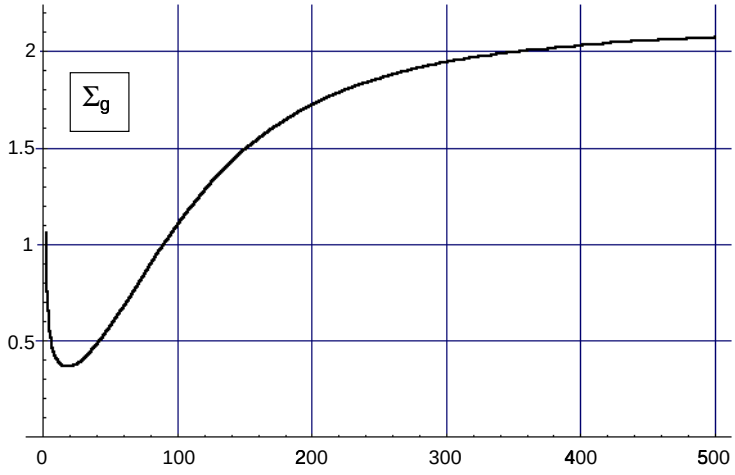

Fig. 4.3: The sum of the cooling partition numbers $\sum_\mathrm{g} = (\mathrm{g_x} + \mathrm{g_y} + \mathrm{g_L})$ as a function of momentum p (0–500 MeV/c). $\mathrm{g_x}$ and $\mathrm{g_y}$ are naturally 1 while $\mathrm{g_L}$ becomes strongly negative for p < 200 MeV/c. $\sum_\mathrm{g}$ remains greater than 0, which means that ionization loss remains intrinsically cooling at low momenta.

Note that the coupled transverse cooling (and heating) changes occur in the same direction (i.e. horizontal or vertical) as the dispersion and wedge. However, the sum of the cooling rates (over x, y, and z) remains constant. This sum can be represented, as with radiation damping, as a sum of cooling partition numbers, where the partition number is defined as the ratio of the cooling rate to the fractional momentum loss rate. For x and y emittance cooling the partition numbers are both naturally 1:

$$\mathrm{g_y} = \mathrm{g_x} = \frac{(\mathrm{d}\epsilon_\mathrm{x}/\mathrm{ds})/\epsilon_\mathrm{x}}{(\mathrm{dp/ds})/\mathrm{p}} = 1 \ . \tag{4.7}$$

The partition number for longitudinal cooling is given by

$$\mathrm{g_L} = \frac{(\mathrm{d}\epsilon_\mathrm{L}/\mathrm{ds})/\epsilon_\mathrm{L}}{(\mathrm{dp/ds})/\mathrm{p}} = \frac{\partial(\mathrm{dE/ds})}{\partial \mathrm{E}} \Big/ \frac{\mathrm{dp/ds}}{\mathrm{p}} = \frac{\partial(\mathrm{dp/dt})/\partial \mathrm{p}}{(\mathrm{dp/dt})/\mathrm{p}} \tag{4.8}$$

which is a function of muon energy. With this respecification the longitudinal cooling equation can be written as:

$$\frac{\mathrm{d}\sigma_\mathrm{E}^2}{\mathrm{ds}} = -2\frac{\mathrm{g_L}(\mathrm{dE/ds})}{\beta^2 \mathrm{E}} \sigma_\mathrm{E}^2 + 4\pi(\mathrm{r_e m_e c^2})^2 \mathrm{n_e} \gamma^2 \left(1 - \frac{\beta^2}{2}\right) \ . \tag{4.9}$$

With wedge enhancement of longitudinal cooling, $\mathrm{g_x}$ becomes:

$$\mathrm{g_x} = 1 - \frac{\eta \rho'}{\rho_0} \ , \tag{4.10}$$

while g_L increases by $\eta\rho'/\rho_0$, leaving the sum of the partition numbers $\sum_g = (g_x + g_y + g_L)$ constant. This sum is a function of muon momentum, and the sum of the partition numbers is displayed in Fig. 4.4. $\sum_g$ is approximately 2 for $p_\mu > 0.3$ GeV/c, but is smaller for lower energies. However, $\sum_g$ does remain positive for all energies, which indicates that cooling remains possible even at low μ energies.

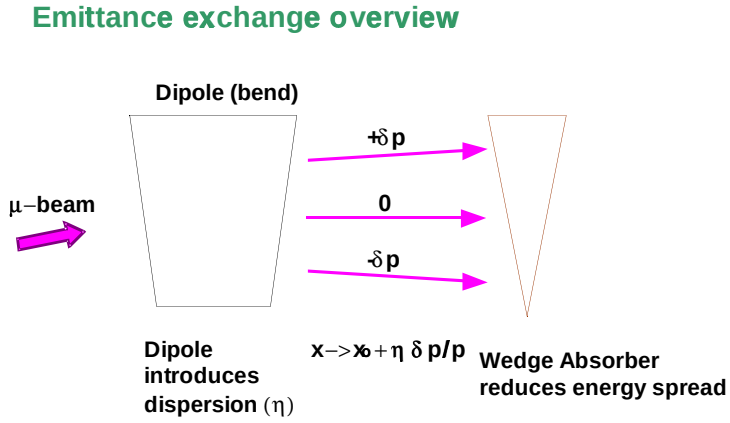

Fig. 4.4: Overview of an emittance exchange section, in which longitudinal emittance is reduced by using a wedge absorber at nonzero dispersion.

4.3 Cooling considerations

Some general considerations on the conditions for cooling, and the required absorbers and beam transports, can be developed from Eqs. (4.1) to (4.9). From Eq. (4.1) [with g_x from (Eq. 4.7)] we find an equilibrium emittance from setting the derivative to zero:

$$\epsilon_{N,eq} = \frac{\beta_\perp E_s^2}{2 g_x \beta m_\mu c^2 L_R (dE/ds)} \ . \tag{4.11}$$

This represents the minimal obtainable emittance for a given material and focusing parameter $\beta_\perp$. From this expression, obtaining small emittance implies having small $\beta_\perp$ (strong focusing), as well as large L_R dE/ds (small multiple scattering) at the absorber. Table 4.1 displays parameters of typical cooling materials; large L_R dE/ds implies light elements (H, Li, Be, etc.) for the absorber material.

In order to minimize multiple scattering heating equivalently the beam angular spread needs to be kept larger than the multiple scattering angles at the absorbers. If we require in Eq. (4.1) that the cooling term be twice as large as the heating term, then the angular spread at the absorber is given by:

$$\langle \theta_{rms}^2 \rangle = \frac{\epsilon_N}{\beta_\perp \beta \gamma} = \frac{E_S^2}{\beta^2 \gamma m_\mu c^2 L_R (dE/ds)} \ . \tag{4.12}$$

At typical parameters ($P_\mu = 240$ MeV/c), θ_{rms} (matched) is ~ 60 mrad for H_2, 80 mrad for Li and 90 mrad for Be absorbers. From Eq. (4.11) and consideration of minimum-$\beta_\perp$ focusing conditions (see below), we expect to be able to obtain $\beta_\perp \cong 0.01$ m, which means the transverse emittances can be cooled to $\epsilon_{\perp,n} \cong 0.0001$ m-rad.

Even with cooling, energy spreads are large. An expression for the energy spread can be found from Eqs. (4.2), and (4.4) and (4.5), obtaining:

$$\Delta E_{rms}^2 = \frac{4\pi (r_e m_e c^2)^2 N_A \rho Z \gamma^2 E \beta^2}{2 g_L (dE/ds) A} \left(1 - \frac{\beta^2}{2}\right) \ . \tag{4.13}$$

Solving for $\Delta E/E$ finds a minimum value of $\sim 2\%$ at E = 250 MeV, with relatively weak energy dependence ($\sim 3\%$ at E = 500 MeV) and relatively weak dependence on material.

Table 4.1
Material properties for ionization cooling [6]

Material	Symbol	Z	A	dE/ds (min.) (MeV/cm)	L_R (cm)	L_R dE/ds (MeV)	Density (g/cm^3)	$g_x\beta\epsilon_{N,eq}/\beta_\perp$ mm-mrad/cm
Hydrogen	H_2	1	1.01	0.292	865	252.60	0.071	37
Lithium	Li	3	6.94	0.848	155	130.80	0.534	71
Lith. hydride	LiH	3+1	7+1	1.340	102	137.00	0.9	68
Beryllium	Be	4	9.01	2.980	35.3	105.20	1.848	88
Carbon	C	6	12.01	4.032	18.8	75.80	2.265	122
Aluminium	Al	13	26.98	4.370	8.90	38.90	2.70	238
Copper	Cu	29	63.55	12.900	1.43	18.45	8.96	503
Tungsten	W	74	183.85	22.100	0.35	7.73	19.3	1200

The minimum longitudinal emittance depends on the product of bunch length and energy spread. Longitudinal focusing can be varied substantially, depending on the RF wavelength and gradient, as well as the transport isochronicity. However, from recent studies, cooling to bunch lengths of $\sim$ 1 cm seems readily achievable. A 3% energy spread at $E_\mu \cong 250$ MeV ($\sigma_E \cong 7.5$ MeV) obtains a normalized longitudinal emittance of:

$$\epsilon_{L,N} = \frac{\sigma_{ct}\sigma_E}{m_\mu c^2} \cong 0.0007 \text{ m} . \tag{4.14}$$

A cooling scenario with a normalized 6D emittance cooling goal of $\sim 10^{-10}$ m^3 appears possible, and that is (approximately) the cooling goal of recently proposed μ^+–μ^- collider scenarios. More detailed considerations are discussed below; however, complete specifications await more complete design and cooling scenario development.

4.4 Longitudinal motion with ionization cooling

Longitudinal motion requires particular attention, since ionization cooling does not naturally cool effectively in the longitudinal direction, and energy straggling in the energy loss process naturally increases the energy spread to relatively large values. Also, cooling at lower energies ($p_\mu < 300$ MeV/c) heats the beam longitudinally. The transport must keep the beam confined longitudinally, and additional longitudinal cooling (from emittance exchanges) must be regularly included in the cooling channel.

The equations of longitudinal motion in a linac are:

$$\frac{d\Delta E}{ds} = eV'(\cos(\phi+\phi_s) - \cos\phi_s) \cong -eV' \sim \phi_s\phi \tag{4.15}$$

$$\frac{d\phi}{ds} = \left(\frac{1}{\beta_0} - \frac{1}{\beta}\right)\frac{2\pi}{\lambda_0} \cong \frac{1}{\beta^3\gamma^3}\frac{2\pi}{\lambda_0}\frac{\Delta E}{mc^2} \tag{4.16}$$

This second equation should be modified in the case of a noncolinear transport by the inclusion of the nonisochronous transport element $M_{56}^{1/2} \equiv 1/\gamma_t^2$ (or $\alpha_p = 1/\gamma^2 - 1/\gamma_t^2$), to

$$\frac{d\phi}{ds} \cong \frac{1}{\beta^3\gamma}\left(\frac{1}{\gamma^2} - \frac{1}{\gamma_t^2}\right)\frac{2\pi}{\lambda_0}\frac{\Delta E}{mc^2} = C_1\Delta E , \tag{4.17}$$

where $M'_{56} = \eta/R$ and η is the dispersion and R is the local bending radius, and the symbol C_l is introduced as a shortened notation for the equation coefficient.

In ionization cooling an energy loss term dE/ds is added. The mean energy (E_0) remains constant if $dE/ds = eV' \cos\phi_s$. If only this mean energy loss is included, then the equations of motion are integrable for $\Delta E, \phi$, and particle trajectories move along orbits such that:

$$\frac{(\Delta E)^2}{2} = \frac{eV'\lambda_0 mc^2\beta^3\gamma}{2\pi\alpha_p}[(\phi_0 - \phi)\cos\phi_s + (\sin(\phi + \phi_s) - \sin(\phi_0 + \phi_s))] \,, \tag{4.18}$$

where ϕ_0 is a constant of a trajectory and $\Delta E(\phi)$ maps out a particle trajectory. The separatrix (separating trapped from untrapped particles) is obtained from Eq. (4.4) with $\phi_0 = -2\phi_s$. Figure 4.5 shows the separatrix and an interior orbit ($\phi_0 = -\phi_s$) at 'typical' ionization cooling parameters, used in ASOL cooling segments: $eV' = 20$ MV/m, $\phi_s = 1$ rad, $E = 205.66$ MeV, $\alpha_p = 1/\gamma^2$, and $\lambda_0 = 0.375$ m (800 MHz RF). The separatrix extends over $\Delta E = \pm 27$ MeV, which is not much larger than typical energy spreads ($\Delta E_{rms} \cong 10$ MeV) (see Fig. 4.5). The numbers indicate that there are not large safety factors in forming stable bunch configurations at ionization cooling parameters.

A useful parameter is the ratio of the energy to the phase amplitude (in the small amplitude limit); this corresponds to a longitudinal 'betatron' function:

$$R = \frac{\Delta E}{\phi} = \sqrt{\frac{eV'\sin\phi_s\beta^3\gamma\lambda_0 mc^2}{2\pi\alpha_p}} \,. \tag{4.19}$$

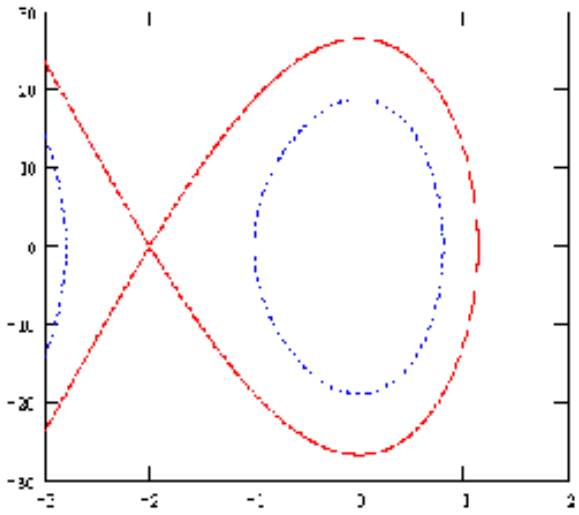

Fig. 4.5: RF bucket – separatrix and an interior orbit (in ΔE, ϕ space) and for $E_{total} = 205.66$ MeV, $\lambda_0 = 0.375$ m (800 MHz), $\phi_s = 1$ rad.

This factor is ~ 22 MeV at the reference parameters. Another useful parameter is the longitudinal motion oscillation length; the distance over which the longitudinal motion undergoes a full phase-space oscillation. For small amplitude oscillations this can be written as:

$$\lambda_{osc} = 2\pi\sqrt{\frac{\beta^3\gamma\lambda_0 mc^2}{2\pi\alpha_p eV'\sin\phi_s}} \,. \tag{4.20}$$

This is 8.3 m at the reference parameters.

As previously discussed, the rms energy spread is naturally at least 3% from energy straggling with cooling. Thus an rms energy spread of $\Delta E_{rms} \sim 7$ MeV ($3\sigma = 21$ MeV), would fit (barely) within the RF bucket shown in Fig. 4.5 and would have a 3σ phase spread of ± 1 rad ($\phi_{rms} \cong 0.33$ rad or $\delta ct \cong 2$ cm, which would lead to a normalized longitudinal emittance of $\epsilon_{L,rms} \cong \delta ct \Delta E_{rms}/(mc^2) \cong 0.0014$ m. Lower frequency RF systems could trap larger emittance beams, and lower frequency RF systems could also confine larger energy spreads, if the gradient eV' does not decrease by more than λ^{-1}. For example, a 50 MHz RF system with $eV' = 5$ MV/m would have a 32 cm long rms bunch length and a $\sqrt{2}$ larger ΔE for an rms emittance of 0.032 m.

Acceptance of larger momentum spreads and/or larger emittances requires some combination of higher gradients (eV'), longer wavelengths (λ_0), operating at higher energies (increases accepted ΔE by $(\beta\gamma)^{3/2}$, if $\alpha_p = 1/\gamma^2$), use of non-linac, more isochronous bunching transports ($\alpha_p \neq 1/\gamma^2$), and use of multiharmonic RF systems.

4.5 Cooling and heating effects

Ionization cooling significantly changes the longitudinal motion, adding an energy-dependent energy loss term, dE/ds, as well as an energy straggling term, $d(\Delta E)^2/ds$. The energy-dependent loss term contains an intrinsic dependence written as $\partial(dE/ds)/\partial E = g_L((dp/ds)/p)$ as well as emittance exchange with a wedge absorber. In that case the cooling derivative can be rewritten as:

$$\frac{\partial(dE/ds)}{\partial E} \Rightarrow \left.\frac{\partial(dE/ds)}{\partial E}\right|_0 + \frac{dE}{ds}\frac{\eta\rho'}{\beta cp\rho_0} \tag{4.21}$$

where ρ'/ρ_0 is the change in density with respect to transverse position, ρ_0 is the reference density associated with dE/ds, and η is the dispersion ($\eta = dx/d(\Delta p/p)$).

Without the stochastic process of energy straggling, the longitudinal equation of energy change can be rewritten as:

$$\frac{d\Delta E}{ds} = eV'(\cos(\phi + \phi_s) - \cos\phi_s) - g_L\frac{dE/ds}{\beta^2 E}\Delta E \cong -eV'\sin\phi_s\phi - g_L\frac{dE/ds}{\beta^2 E}\Delta E\,. \tag{4.22}$$

The mean beam energy remains constant if the energy gain $eV'\cos(\phi_s)$ equals the energy loss $dE/ds(E_0)$, where E_0 is the central beam energy. The linearized equations of motion can be solved, obtaining:

$$\Delta E = \Delta E(0) e^{B_1 s/2}\cos(k_1 s + \Psi_0) \tag{4.23}$$

where $B_1 = -g_L(dE/ds/\beta^2 E)$ and $k_1 = \sqrt{C_1 eV'\sin\phi_s - B_1^2/4}$. Note that for $p_\mu < \sim 300$ MeV/c, g_L is naturally negative (without emittance exchange), which means that the longitudinal emittance grows exponentially.

An estimate of the effect on longitudinal acceptance can be obtained by simply multiplying the limits of the zero-cooling bucket by $e^{-Bs/2}$ and reducing the bucket area by e^{-Bs}, where s is the length of a transverse cooling segment. For a 20 m cooling section at $p_\mu = 180$ MeV/c, where $g_L \cong 0.4$ (and $dp/ds \cong 12$ MeV/c/m), $e^{-Bs/2} \cong 0.77$, and the phase space area factor is 0.59, which means longitudinal emittance growth by 70%, simply from the dE/ds slope. (The energy straggling term also increases the emittance.) This is consistent with the heating seen in the ASOL cooling simulations. This intrinsic heating rate implies that some longitudinal cooling must be added to avoid unacceptable losses from the accelerating bucket.

This heating term does not include energy straggling. The addition of the energy straggling term adds only $\sim 10\%$ to this heating term at $p_\mu < 200$ MeV/c; the energy straggling term does become larger than the anti-damping at $E > \sim 350$ MeV.

4.6 Thick wedge absorbers

In practice the emittance-exchange wedge inserts can obtain a relatively large exchange in a single insert. A consideration of beam transformations with thick wedges can be very useful [9].

Figure 4.6 shows a stylized view of the passage of beam with dispersion through an absorber. The beam properties entering the wedge are the beam energy and momentum E_0, p_0, the relative beam momentum width $\delta_0 = \Delta p_0/p_0$, the beam transverse emittance ϵ_0, and the betatron function β_0, and the dispersion η_0. (To simplify discussion, we set β_0', $\eta_0' = 0$ at the wedge.) The wedge changes the momentum offset by:

$$\frac{\Delta p}{p} = \delta \to \delta - \frac{(dp/ds)\tan\theta}{p} x = \delta - \delta' x \tag{4.24}$$

where dp/ds is the momentum loss rate in the material ($dp/ds = \beta^{-1} dE/ds$), which is dependent on the material and the particle energy, and $x \tan\theta$ is the wedge thickness at transverse position x, and we have introduced the symbol $\delta' = dp/ds \tan\theta/p$ to indicate the change of d with x.

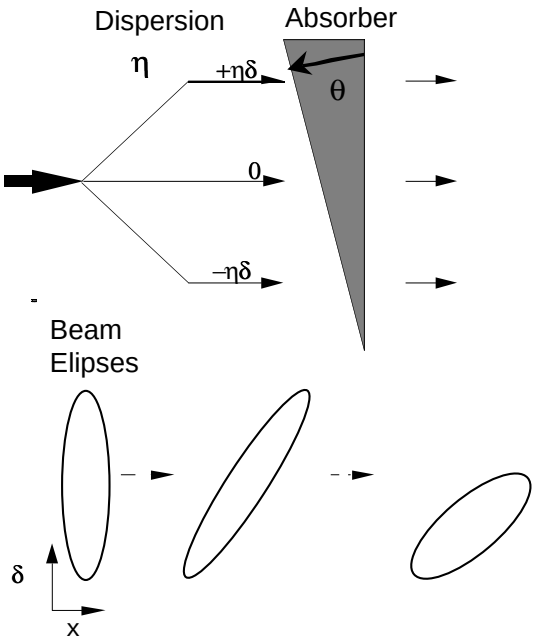

Fig. 4.6: Overview of the beam transformation in passing through a wedge absorber. The upper portion shows a stylized view of a beam passing through a dispersive transport into a wedge absorber; the lower portion shows the projection of the 6D beam phase space ellipse into x-δ phase space, and its changes passing through the system. Dispersion imposes an x-δ correlation (ellipse tilt), and the wedge reduces the beam energy $\delta(x)$, with energy loss a function of x: $\Delta\delta = \delta' x = x\,dp/ds \tan\theta/p$. Note that the x-$\delta$ ellipse area remains the same (in the limit where average energy loss is zero).

In first order, we ignore the central beam energy loss, as well as multiple scattering and energy straggling in the absorber, and consider only the effects of δ' and η_0. In that case, δ' and η_0 can be represented as linear transformations in the x-δ phase space projections and the transformations are phase-area preserving. The dispersion + wedge becomes:

$$M_{\eta\delta} = \begin{bmatrix} 1 & 0 \\ -\delta' & 1 \end{bmatrix} \cdot \begin{bmatrix} 1 & \eta_0 \\ 0 & 1 \end{bmatrix} = \begin{bmatrix} 1 & \eta_0 \\ -\delta' & 1 - \delta'\eta_0 \end{bmatrix} . \tag{4.25}$$

Under the general assumption of smoothly populated beam distributions, we can represent the x-δ beam distribution as a phase space ellipse, and transformations of that phase ellipse by the

above transport matrix can be used to derive the properties of the beam after the wedge. The energy width is changed to:

$$\delta_1 = \sqrt{g_1 \sigma_0 \delta_0} = \delta_0 \left[(1 - \eta_0 \delta')^2 + \frac{\delta'^2 \sigma_0^2}{\delta_0^2} \right]^{1/2} . \tag{4.26}$$

In the transformations the bunch length is unchanged. The longitudinal emittance is also changed by the factor δ_1/δ_0.

The transverse emittance, the transverse (for $\eta = 0$) beam size, and betatron functions are changed by the inverse of this factor:

$$\{\epsilon_1, \sigma_1, \beta_1\} = \{\epsilon_0, \sigma_0, \beta_0\} \left[(1 - \eta_0 \delta')^2 + \frac{\delta'^2 \sigma_0^2}{\delta_0^2} \right]^{-1/2} . \tag{4.27}$$

The new value of the dispersion is:

$$\eta_1 = \frac{\eta_0 (1 - \eta_0 \delta') - \delta' (\sigma_0^2/\delta_0^2)}{(1 - \eta_0 \delta')^2 + \delta'^2 (\sigma_0^2/\delta_0^2)} . \tag{4.28}$$

Note that the change in betatron functions (β_1, η_1) implies that the following optics should be correspondingly rematched.

A number of possible emittance exchange cases can be developed from this formalism. A maximal exchange case can be developed if $\eta_0 \delta' = 1$; a dispersion-cancelling exchange can be obtained from a solution with $\eta_1 = 0$; an emittance exchange can be arranged to increase δ (and decrease emittance) by choosing negative initial dispersion η_0. For thin wedges (small θ) the formalism is readily converted to a differential equation, covering small changes (per step), such as presented in Eq. (4.7).

An accurate treatment requires inclusion of effects of the finite average energy loss, heating as well as the energy-loss cooling, and can be obtained from the more detailed simulation codes. The above expressions give useful first estimates of the effects of emittance-exchange cooling segments, and can obtain approximate initial cooling-segment designs.

4.7 Cooling components

As discussed above, optimum cooling requires focusing the beam to small spots at the absorbers (or, equivalently, increasing the beam angular width above the multiple scattering width), which means strong focusing. Various focusing configurations have been considered, including magnetic quadrupole and solenoid focusing, as well as Li lens focusing. These methods are believed to be sufficient to reach cooled emittances of $\epsilon_{N,\perp} \sim 10^{-4}$ m-rad.

Quadrupole focusing suffers from the disadvantage that it focuses in only one plane at a time. That means that the beam leaving an absorber with a divergence of ~ 100 mrad is initially defocused in one dimension (increasing a divergence to ~ 200 mrad or more) which rather easily increases geometric aberrations above acceptable limits. Solenoid focusing and a Li lens both focus radially and are therefore currently preferred for focusing at or near the absorbers.

4.7.1 Solenoid focusing

A particle entering a solenoid is displayed in Fig. 4.7. To simplify discussion we set the initial momentum as purely longitudinal, with initial transverse position at a radius r_0 [10]. The longitudinal magnetic field increases from 0 to B_0, while the radial magnetic field is:

$$B_r = -1/2\, r\, dB_z/dz .$$

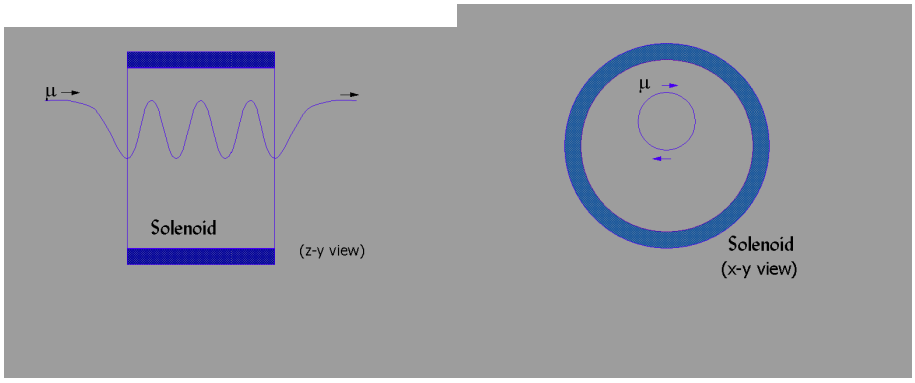

Fig. 4.7: Schematic view of a particle trajectory entering and exiting a long solenoid. An initially longitudinal off-centre trajectory ($y = y_0$) develops an angular momentum p_θ from $v_z \times B_r$, where B_r is the radial B-field from the fringe fields entering the solenoid ($B_r = -1/2\, dB_z/dz$). Inside the solenoid the particles follow circular trajectories passing through the magnet centre, which corresponds to focusing toward the centre. Exiting the solenoid the process is reversed, and the angular momentum is removed. (The figure shows an integral number of oscillations within the solenoid.)

In entering the solenoid the transverse momentum increases from integrating the force equation:

$$\vec{F} = e\vec{v} \times \vec{B}\ .$$

Integrating this equation, we find that the particle obtains a transverse momentum of

$$\Delta p_\theta = -\frac{e r_0 B_0}{2} \tag{4.29}$$

while the longitudinal momentum is reduced, conserving particle kinetic energy. This rotational momentum combined with the longitudinal field inside the solenoid provides a radial focusing force. Inside the solenoid the particle follows a helical orbit centred about $r = r_0/2$, with radius r and an angular velocity of $eB_0/m\gamma$.

It is often convenient to transfer the particle motion to a rotating frame; that is, one rotating at the Larmor frequency: $\omega_L = eB_0/(2m\gamma)$. In that frame the ΔP_θ is reduced to zero, while the radial motion becomes that of a harmonic oscillator with

$$\frac{d^2 r}{ds^2} + \left(\frac{B_0}{2B\rho}\right)^2 r = 0\ . \tag{4.30}$$

In the Larmor frame, the coordinate r oscillates between r_0 and $-r_0$ with a period of $2\pi/\omega_L$. When the particle exits the dipole the angular momentum is removed, but the radial focusing integrated over the solenoid (as described in the above equation) remains.

The matched betatron amplitude $\beta_\perp$ for the transverse oscillations can be written as:

$$\beta_\perp = \frac{2B\rho}{B_0} = \frac{2p}{eB_0}\ . \tag{4.31}$$

Note that the matched $\beta_\perp$ is proportional to momentum, implying a preference for using solenoids with lower energy beams. As an example used in cooling scenarios, a 15 T solenoid with 200 MeV/c particles would have a matched $\beta_\perp$ of 8.9 cm. This is sufficiently small to be useful in muon cooling.

4.7.2 Li lens focusing

A particularly attractive configuration for muon cooling is obtained by passing the beam through a conducting light-metal rod (such as a Li lens) which acts simultaneously as a focusing element

and as an energy-loss absorber [11]. A high current passing through the conductor provides an angular magnetic field given by:

$$\mathrm{B}_\theta = \frac{\mu_0 \mathrm{Ir}}{2\pi \mathrm{R}_\mathrm{c}^2} \tag{4.32}$$

where $\mathrm{R_c}$ is the rod radius and I is the total current in the rod. This angular magnetic field combines with the longitudinal velocity to obtain a radial focusing force with the resulting equation of motion:

$$\frac{\mathrm{d}^2\mathrm{r}}{\mathrm{ds}^2} + \frac{\mathrm{B}'}{\mathrm{B}\rho}\mathrm{r} = 0 \tag{4.33}$$

where $\mathrm{B}' = \mathrm{dB/dr} = \mu_0 \mathrm{I}/(2\pi \mathrm{R}_\mathrm{c}^2)$. Li lenses can provide quite strong focusing and are used for short, strong-focusing collection lenses. The Fermilab Li lens for antiproton collection is designed with $\mathrm{R_c} = 1$ cm, I = 0.5 MA, obtaining 1000 T/m gradients. The matched $\beta_\perp$ for a Li lens is:

$$\beta_\perp = \sqrt{\frac{\mathrm{B}\rho}{\mathrm{B}'}} = \sqrt{\frac{\mathrm{p}_\mu}{\mathrm{eB}'}}\ . \tag{4.34}$$

A Li lens with B = 20 T at a radius $\mathrm{R_c} = 2$ mm is possible and this would obtain a matched $\beta_\perp$ of 1 cm for $\mathrm{p}_\mu = 300$ MeV/c muons. This is somewhat smaller than what could be used with solenoidal focusing systems.

For muon cooling, relatively long lenses are needed to obtain large energy losses (~ 1 m of Li to obtain ~ 100 MeV of energy loss), and the high $\mathrm{I}^2\mathrm{R}$ power deposition associated with higher frequency operation (5–15 Hz) would melt Li. Liquid Li lenses are also desirable because of the brittleness of solid Li lenses, and a replacement liquid lens is being built for the Fermilab antiproton source. A longer, higher gradient liquid Li lens testing the limits of that technology for muon cooling is also planned in the μ^+–μ^- Collider R&D programme [12].

Practical difficulties exist in matching the large emittance, large Δp muon beams into and out of Li lenses, as well as in matching the beams into reaccelerating RF buckets with minimal dilution and losses. While initial attempts were unsuccessful, recently some solutions to this problem have been developed. Optics + cooling optimization remains a research topic.

4.7.3 Solenoid cooling segment

The design challenge is to integrate the focusing elements with the energy-loss absorbers and reacceleration RF cavities. Several possible configurations have been considered, and we will describe two of these: (1) the 'FOFO' scenario, in which the absorbers are placed at foci between strong-focusing solenoids, and (2) the 'ASOL' scenario, in which absorbers are placed within strong-focusing solenoids [13].

Use of solenoids in muon cooling scenarios has some specific difficulties due to the angular momentum added to the beam in entering the solenoid. The extra (amplitude-dependent) transverse momentum $\Delta\mathrm{P}_\theta$ reduces the longitudinal momentum and velocity correspondingly, and causes a significant amplitude-dependent phase lag. In the present cooling scenarios, maintaining phase stability in the reacceleration RF requires developing an amplitude-energy correlation in the beam, so that larger-amplitude particles have higher energies, and the longitudinal velocity of particles becomes amplitude independent.

The additional transverse momentum $\Delta\mathrm{P}_\theta$ is normally removed in exiting the solenoid. However, an absorber inside the solenoid reduces all momentum components including the solenoidal $\Delta\mathrm{P}_\theta$. The beam then retains a net angular momentum after each solenoid/absorber. To avoid a systematic accumulation of angular momentum in the cooling channel, the solenoids alternate in sign from cell to cell, which alternates the sign of the induced angular momentum. Also, individual cells are kept relatively short.

Figure 4.8 displays a schematic view of a sample FOFO transport line. The beam transport is designed so that the betatron amplitude oscillates between larger values within the solenoid to smaller focused values at the absorbers. Thus $\beta_\perp$ can oscillate to a smaller value at the absorber than the matched value. However, the depth of focus constraint ('hourglass' effect) requires that each individual absorber have length $\leq \beta_\perp$, and this limits cooling per cell and requires the use of relatively dense materials. Lithium hydride was used in initial studies. Since the absorber is at a B = 0 point, the residual angular momentum effect does not occur.

In simulations, FOFO lattices developed beam losses from limited momentum acceptance, particularly in matches to the low-$\beta_\perp$ points at the absorbers [13]. It is unclear whether that is a general or a correctable difficulty. (Recently a variant of this geometry is being developed, which reduces the momentum acceptance difficulty [14]).

Figure 4.9 shows a schematic view of an ASOL cooling line segment. In the ASOL configuration, the absorbers are placed within the strong-focusing solenoids and the transports are matched to obtain minimum $\beta_\perp \cong 2\mathrm{B}\rho/\mathrm{B}_0$. Because the absorbers are within the focusing elements the depth of focus constraint does not apply, and long absorbers can be used. Thus liquid hydrogen (H_2), which has the least multiple scattering, can be used. RF cavities are placed between the absorbers and weaker matching solenoids (not shown) are placed around the RF cavities to maintain focusing.

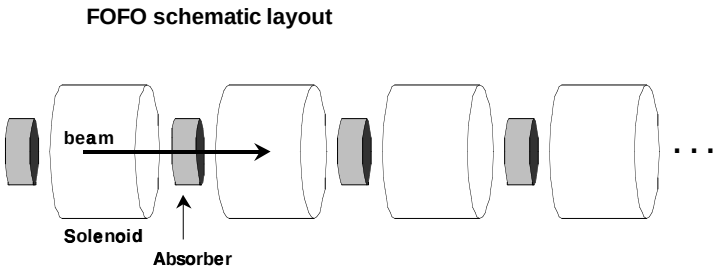

Fig. 4.8: Schematic layout of a FOFO transport/cooling system showing a string of strong-focusing solenoids, with absorbers between them. The solenoids alternate in strength from $+\mathrm{B}_0$ to $-\mathrm{B}_0$, with the absorbers. Reacceleration RF would be included in the system, probably inside the solenoids.

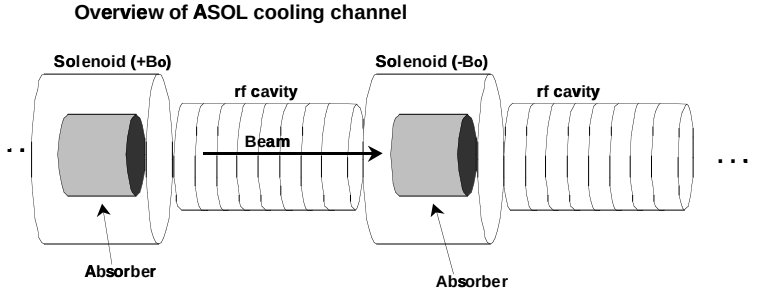

Fig. 4.9: Overview of an ASOL transport cooling channel, which has absorbers within the solenoids.

After considerable trial and error, it was discovered that the critical problem in obtaining adequate momentum acceptance is solved by optimizing the lattice such that $\beta_\perp(\mathrm{p})$ (and $\beta'_\perp$) in the absorbers is (nearly) constant over a broad momentum range ($\mathrm{p}_0 \pm 3\sigma_\mathrm{p}$). In practice this is done by perturbing the matching solenoids between the absorbers (around the RF) [15].

As an example Table 4.2 displays parameters of an ASOL cooling section. The cooling section consists of 17 identical 1.5 m long cells with 0.43 m liquid H_2 absorbers, 0.97 m acceleration cavities, and 15 T solenoidal fields at the absorbers (with weaker matching fields at the cavities). The table also shows results of ICOOL [16] simulations of muon beam transport and cooling through the system. Cooling by a factor of ~ 2 in transverse emittances and a factor of ~ 3 in 6D emittance is obtained. In this section $\sim 1\%$ of the beam is lost to apertures, and 2% is lost by decay. However, momentum spread has increased by $\sim 50\%$ in the channel, and beam is beginning to escape from the accelerating bucket; a longitudinal emittance cooling section following this would be required in a complete scenario. Other simulations have shown that cooling in this section can be improved by adiabatically increasing the focusing field along the channel, following the emittance reduction. The channel does require a strong $\Delta\mathrm{P}/\mathrm{p}_\perp^2$ (or energy-amplitude) correlation to develop matched cooling; however, a precise scenario for generating the needed correlation is not yet established.

The ASOL configuration has advanced significantly toward practical implementation. Figure 8.4 displays an initial engineering design of a sample 1.5 m cell.

Table 4.2
Parameters and performance of an ASOL cooling section

Parameter	Value	
Cell length	1.5 m	
Section length	25.5 m (17 cells)	
Absorber length	0.43 m	
RF frequency	805 MHz	
RF gradient, length/cell	36, 0.97 (MV/m, m)	
$\Delta\mathrm{P}_\mu$ - mean momentum loss/cell	14 MeV/c	
Mean beam momentum	185.5 MeV/c	
B_0 - magnetic field	15 T	
Matched $\beta_\perp$	8.25 cm	
Cooling performance	Before (ICOOL simulation)	After (ICOOL simulation)
Transverse emittance $\epsilon_{\perp,\mathrm{N}}$ (mm-mrad)	1650	800
Longitudinal emittance $\epsilon_{\perp,\mathrm{N}}$ (mm-rad)	1870	2760
$\sigma_\mathrm{x}, \sigma_{\mathrm{p,x}}$ (mm, MeV/c)	8.9, 27.8	6.45, 19.6
$\sigma_\mathrm{z}, \sigma_\mathrm{p}$ (cm, MeV/c)	2.0, 9.5	2.5, 13.1
6D cooling factor	1	0.347

4.7.4 Li lens cooling segments

Design of cooling segments incorporating Li lenses is also developing. Because the lens focuses and cools simultaneously, the depth of focus constraint does not apply and the lens can be extended to ~ 1 m lengths or more to obtain large cooling factors in a single device. Initially, it is believed to be preferable to have relatively long cooling lenses in order to minimize the number of entrance and exit matching sections in the complete cooling scenario. Figure 4.10 shows a stylized view of a Li lens cooling section, showing Li lens, optical matching through a solenoid into a longer reacceleration section, and matching into a following Li lens. The match from lens to lens would be into smaller, stronger focusing Li lenses in a multistep cooling.

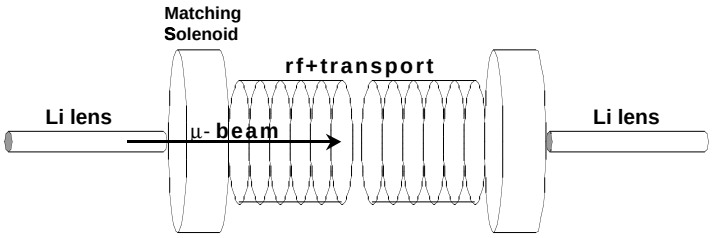

Fig. 4.10 Li lens cooling overview showing a beam transported through a Li lens, matched into an RF reacceleration transport, and focused back into a Li lens.

Some parameters of Li lenses considered for cooling are shown in Table 4.3. In this Table the Li lens lengths have been standardized at 1 m and a sequence of lenses of increasing strength is tabulated as examples of possible parameters.

Table 4.3
Li lens parameters

B T	B′ (T/m)	Radius (cm)	Length (m)	I (MA)	τ ($\delta = 0.7$ r)	β^* at P = 0.3 GeV/c
10	1000	1	1	0.500	1 ms	3.16 cm
15	3000	0.5	1	0.375	250 ms	1.83 cm
20	8000	0.25	1	0.250	63 ms	1.12 cm
20	16000	0.125	1	0.125	15 ms	0.79 cm

Li lenses can be used to extend the cooling to minimal emittances. As discussed above, lenses which can focus to $\beta^* = 1$ cm or less can cool muon beams to $\epsilon_{\rm T} \cong 10^{-4}$ or less. Figure 4.11 shows simulation results of cooling through a sequence of 12 lenses, with $\epsilon_{\rm T,N}$ reduced from 10^{-4} to 0.86×10^{-4} m-rad [17].

Extended cooling scenarios based on the use of Li lens for cooling have been developed by Balbekov. He has constructed scenarios with sequences of up to 15 lenses, with matching and reacceleration RF, as well as emittance exchange, and these scenarios are under investigation.

Using DPGeant, Spentzouris has calculated detailed simulations of cooling sequences with Li lens + matching + RF + matching into a second Li lens, and has successfully obtained matched cooling [18]. Further work in multicell matching and optimization, as well as the inclusion of longitudinal cooling and rematching, is in progress.

4.7.5 Emittance exchange sections

Cooling to collider intensities requires some longitudinal cooling and this implies use of emittance exchange. The general outline of an emittance exchange is a beam transport into a wedge absorber with a relatively large dispersion at the absorber. Several configurations have been considered, initially using dipoles to generate dispersion and solenoids and/or quadrupoles for focusing. Small $\beta_\perp$ at the absorber is also desired to minimize multiple scattering. Because the natural energy spread of the beam is ~ 10 MeV at cooling energies, wedges thick enough to remove that much or more energy are required. From the depth of focus constraint, we need wedge thicknesses less than $\beta_\perp$, unless the wedge is inside a lens.

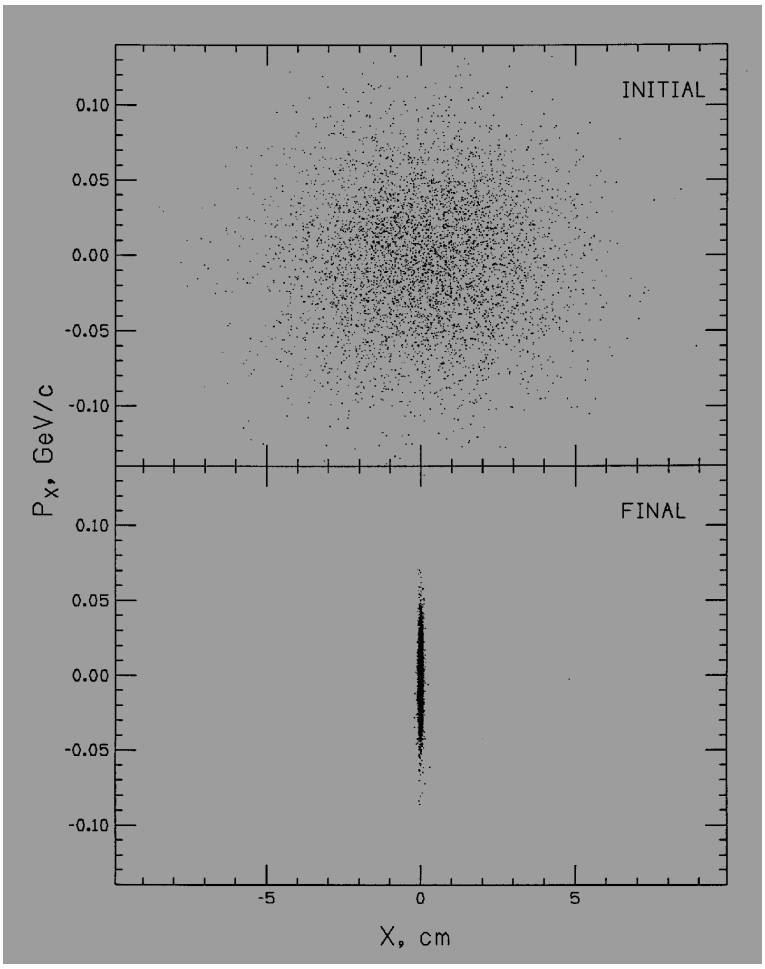

Fig. 4.11: Simulation results of cooling through a sequence of Li lenses, in which transverse emittances are reduced to $\epsilon_N < 10^{-4}$ m-rad. Note that beam size is greatly reduced (with stronger focusing from lens to lens) while transverse momentum spread remains nearly constant at a value set by multiple scattering constraints.

Avoiding multiple scattering blowup requires $\beta_\perp < 10$ cm. This implies that we want

$$\frac{\Delta E}{dE/ds} \leq \beta_\perp \ , \tag{4.35}$$

which means dE/ds > 1 MeV/cm. Requiring larger dE/ds with smaller multiple scattering implies that Be is the best element for wedge absorbers, and that is reflected in some designs.

One candidate optical configuration is use of a bent solenoid, since the solenoid focuses the beam, while the bent configuration generates dispersion. Figure 4.12 shows an outline of an emittance exchange section based on a bent solenoid design, showing a bend and a wedge system followed by a second bend + wedge system; the double system obtains emittance exchange with vertical, and then horizontal motions. In a bent solenoid the beam develops a dispersion in the plane opposite to the bend (vertical for horizontal bend) with a magnitude of

$$\eta = \int \frac{B\rho}{BR} ds = \frac{B\rho}{B}\Theta \tag{4.36}$$

where $B\rho = p/e$ is the magnetic rigidity of the beam, B is the solenoidal field, R is the bend radius and θ is the integrated bend angle. Some simulation results of motion through the system are displayed in Fig. 4.13, where exchange of transverse beam size with momentum spread is clearly

shown. Currently integration of the emittance exchange with the transverse cooling, including longitudinal phase-space matching and reacceleration is an important design challenge [19].

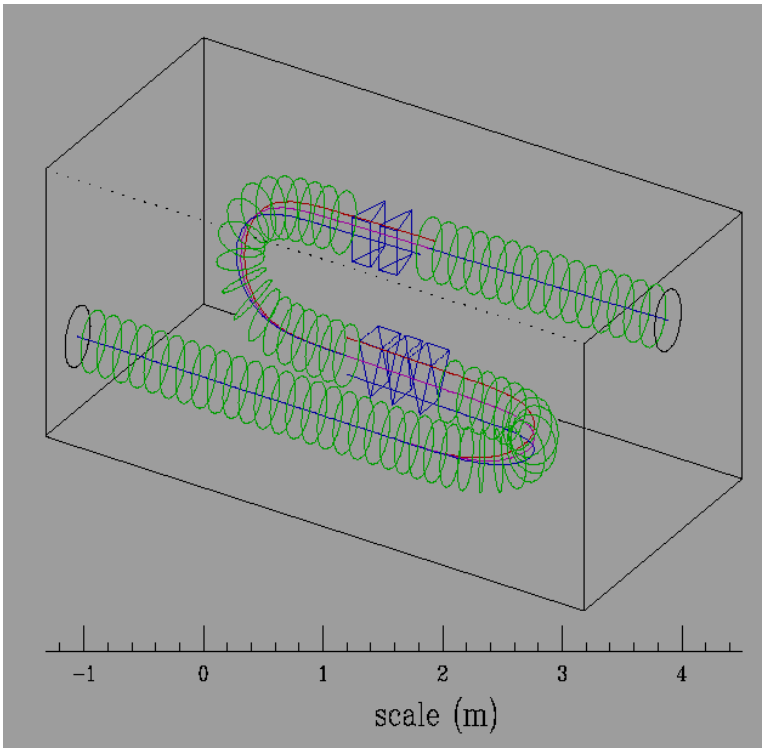

Fig. 4.12: Schematic view of a bent solenoid geometry for emittance exchange, showing bent solenoids going into a sequence of two wedge systems, (green circles indicate coil positions). Particle rays exhibiting the dispersive behaviour are also shown.

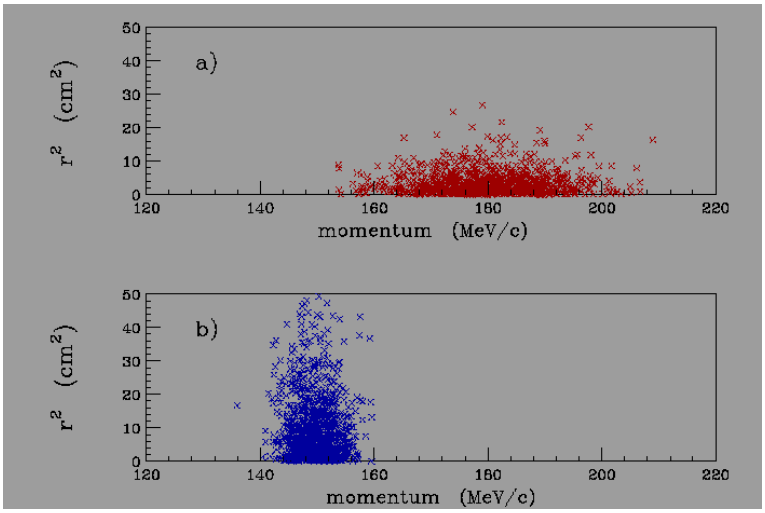

Fig. 4.13: Results of emittance exchange simulation through a bent solenoid system. Transverse beam size is increased, while momentum spread is decreased.

Other configurations are possible, including those using dipoles to generate the dispersion. Combining the emittance exchange sections with transverse cooling sections to form effective 6D cooling systems is an active research topic, and completely satisfactory solutions have not yet been found. Designs which integrate transverse cooling with the emittance exchange are particularly desirable. An example is a design that integrates a bending field onto a Li lens with Be

wedges to obtain simultaneous transverse/longitudinal cooling, developed by T. Vsevoloshkova [20]. Other designs combining transverse/longitudinal cooling are being developed by V. Balbekov [21].

4.8 Cooling scenarios

The complete cooling scenario must take the transverse emittance from $\epsilon_N = 0.017$ m-rad to $\sim 10^{-4}$, while reducing bunch lengths from ~ 1 m to ~ 1 cm, and keeping δp/p less than $\sim 10\%$. This is imagined to occur in a sequence of cooling steps.

An outline complete cooling scenario was initially developed by R. Palmer [22], based on rms cooling equations. However, that outline has not yet been fully updated to include results from the more detailed simulations which have since been developed. In this section we present an outline of the features of a cooling scenario. Detailed design and implementation of the cooling scenario has not yet been accomplished, and is an important goal of the present research.

In initial cooling regions, the large beam sizes from the RF rotation/capture section are reduced by transverse cooling to a size that can be transported through an extended cooling range. The following cooling sections are dominated by longitudinal cooling requirements, as the bunch lengths are shortened from ~ 1 m to ~ 0.1 m or less. In this process the RF reacceleration frequencies are increased from ~ 30 MHz to ~ 300 MHz, to a level where higher gradients and more compact apertures are possible. At this point the beam would have a momentum of $P_\mu \cong 200$–300 MeV/c, a transverse emittance $\epsilon_{t,rms}$ of ~ 0.004 m-rad, so that the rms radius is 4 cm or smaller, $\sigma_z < 0.1$ m. As discussed above, after an initial reduction, δ p/p is $\sim 4 \pm 2\%$ through the cooling channel, and the rms beam angular spread is ~ 100 mrad within the cooling absorbers.

Most of the actual cooling thus occurs in intermediate cooling stages. Within present understanding this intermediate area would be predominantly ASOL cooling elements with absorbers within solenoids. The solenoidal fields at the absorbers would increase from ~ 2 T to ~ 20 T. Emittance exchange along the channel must be included to prevent longitudinal beam blowup, and to provide some net longitudinal cooling so that bunch lengths can be reduced, and reacceleration frequencies would be increased to 800 MHz or more.

Toward the end of this cooling sequence, obtaining adequate focusing with solenoids becomes increasingly difficult, and we would choose Li lens absorbers in order to obtain stronger focusing and cool to minimum emittance values. Cooling to $\epsilon_{t,rms} \sim 0.0002$ m-rad with bunch lengths of 1 cm should be obtained.

In order to obtain minimal-emittance beams, in the final cooling stages, the beams are run at very low energies, so that β^* can be minimized, and an emittance exchange between transverse and longitudinal cooling can be generated. Two methods that can achieve this have been suggested: an anti-wedge absorber which increases energy spread while reducing transverse emittances, or cooling at low energies in a Li lens. At low energies (low momenta) the Li lens can focus to very small β^* and relatively short lengths of absorber can cool the beam to small transverse emittances. However, at low energies, longitudinal energy loss is strongly antidamping, and 6D cooling is at best stationary. The net effect of running in a strong transverse cooling situation with large longitudinal antidamping is a large emittance exchange. Cooling from $\epsilon_{T,N} = 2 \times 10^{-4}$ m-rad to 0.5×10^{-4} with longitudinal emittance dilution by a factor of 10 (or more) appears possible from scenario simulations.

This outline follows a possible approach for cooling from the muon source to the beginning of acceleration; however, the details have not been provided. Significant difficulties exist in: (1) obtaining sufficient gradient in reacceleration to avoid muon decay, particularly at lower

frequencies, (2) avoiding losses at apertures, particularly in initial and final cooling, (3) integration of transverse and longitudinal cooling, and (4) matching between cooling segments without emittance dilution and beam loss. Difficulties also exist in practicality of components and affordability. Variations in the scenario, and possibly very different scenarios, should be explored to find a practical solution.

Alternative scenarios in which the beam is kept somewhat shorter throughout the system (including through the RF rotation/capture) are being developed, so that RF frequencies can be kept above 100 MHz. These may be more affordable, and may also require starting with more bunches and possibly later recombining them to increase luminosity.

Initial design efforts have been concentrated on developing a single-pass scenario. However, it is likely that considerable cost savings could be obtained by having the beam pass through the same cooling hardware for several turns. V. Balbekov has designed an outline cooling system called a ring cooler for multipass cooling [23]. In that design the horizontal, vertical and longitudinal tunes/ turn are set near an integer (or half-integer) so that, in the combination of beam transport plus ionization cooling, the betatron and synchrotron amplitudes (beam sizes) naturally decrease from turn to turn, following the cooling. The dynamics sets a natural basis for multiturn cooling (see Fig. 4.14).

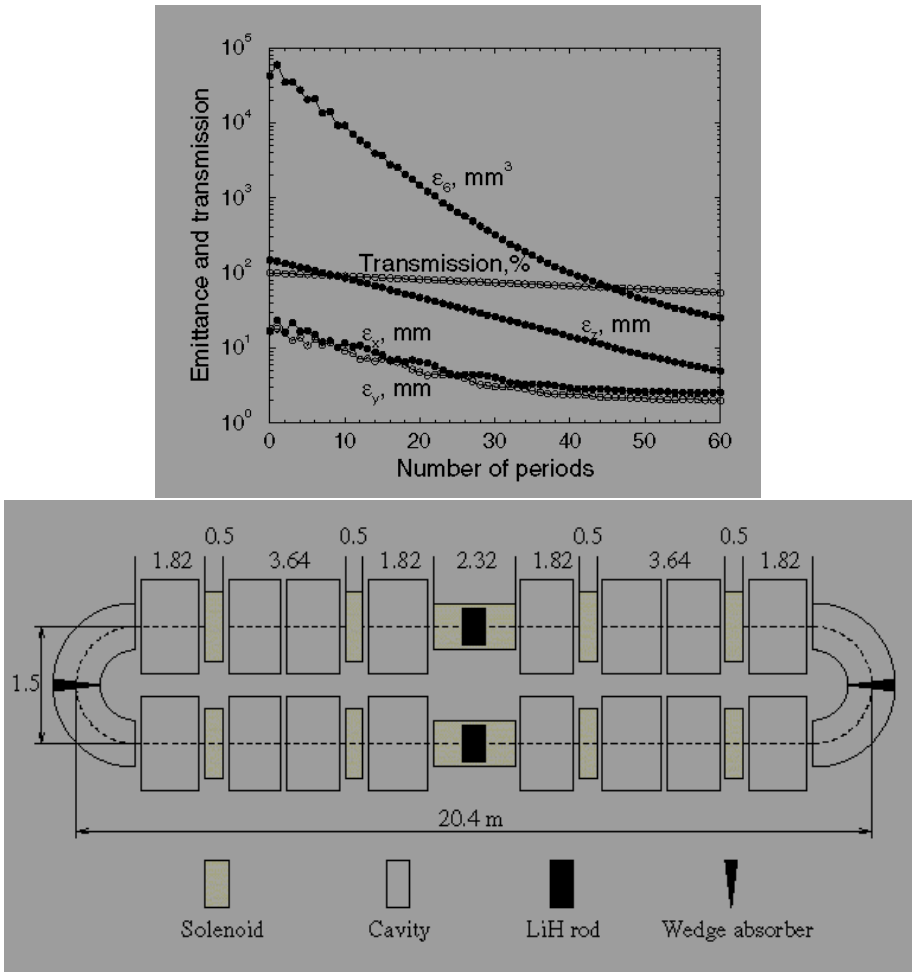

Fig. 4.14: Overview of a Ring Cooler for muons, with simulation results for multiturn cooling.

4.9 Cooling simulation codes

The cooling discussion above has been largely based on rms representations of energy loss and scattering and linear beam-optics transports. However, the energy loss and scattering are notoriously non-Gaussian in statistics with extended tails, and accumulation of beam losses from these tails could become unacceptable. Also the fact that the beams have large angular spreads and large momentum spreads implies that a linear optics treatment could be very inaccurate. Cooling system design must include a more complete picture of beam-material interactions and of the nonlinear optics.

Several simulation codes covering the complicated beam dynamics codes needed to simulate ionization cooling have been developed [24]. Two multiuser codes that are designed to incorporate the full complexity of muon cooling have been developed and applied to ionization cooling examples. They are ICOOL, developed at BNL by R. Fernow and collaborators [25], and DPGeant, developed by P. Lebrun and collaborators at Fermilab [26]. Reoptimization of the cooling parameters after consideration of more complete beam dynamics is under development. Recently an approach toward optimization of cooling by consideration of the coupled particle moment equations has had some success, initially in reoptimizing FOFO configurations, and will be applied to emittance exchange configurations [14].

4.10 Other cooling methods

To date, only ionization cooling, using magnetic and Li lenses for focusing, and reaccelerating RF and low-Z aborbers, with the cooling of medium-energy muons (100–400 MeV kinetic energies), is believed to be within reach of presently available technology and to provide cooling fast enough to avoid muon decay. Other cooling methods are being considered and could eventually become practicable. These methods include:

1) Low-energy cooling methods: Here the general technique is to stop (or nearly stop) the muons within a material, which obtains very cold μ's. The difficulty then is in separating them from the material into a compressed, acceleratable bunch (before they decay).

For positive muons, the bunches can be stopped in a hot tungsten foil, where they combine with atomic electrons to form muonium (μ^+e^- atoms). The muonium atoms evaporate from the foil, where intense laser light pulses resonantly excite and ionize the atoms, and the resulting cloud of muons can then be electromagnetically trapped and accelerated. The process has been implemented at the level of a few per second by Nagamine et al., and intensity upgrades to $\sim 10^{10}$/s are being considered [27].

For negative muons, a sequence of tungsten foils can be used to obtain a very low-energy muon beam which can then be cooled with 'frictional cooling', which is energy-loss cooling at kinetic energies that are small enough that energy cooling is naturally damping (< 20 keV). The frictional cooling process has been demonstrated at PSI, but extrapolation to μ^+–μ^- collider intensities is problematic [28].

2) Optical stochastic cooling: Stochastic cooling has a natural cooling time set by

$$\tau_{\rm cool} \cong \frac{\rm N}{\rm W}$$

where W is the bandwidth of the cooling system (pickup and kicker) and N is the number of particles. In optical stochastic cooling, the pickup and kicker are magnetic wigglers producing light near optical frequencies, with W $\sim 10^{14}$ s^{-1}, and it is in principle possible to cool 100 GeV μ's before decay [29]. However, practical difficulties are significant.

It is, of course, conceivable that other methods may be developed and applied to the problem of muon cooling, and these methods may include some of the concepts we have presented, as well as to-be-invented components.

4.11 Cooling summary

While the general principles of ionization cooling to produce cooled muon beams have been developed, ionization cooling has not yet been demonstrated or implemented in practice. The goal of the current cooling R& D is to develop a practical scenario for cooling muons to collider intensities and to construct and operate key components of the cooling scenario to demonstrate cooling performance. This effort has been organized into an experimental proposal, which is described in more detail in Chapter 8 [30]. Much research remains to be done to fulfil this goal.

References

[1] A.N. Skrinsky and V.V. Parkhomchuk, Sov. J. Nucl. Phys. **12**, 3 (1981).

[2] E.A. Perevedentsev and A.N. Skrinsky, *Proc. 12th Int. Conf. on High Energy Accel.*, p. 485 (1983).

[3] D. Neuffer, Part. Accel. **14**, 75 (1983).

[4] D. Neuffer, *Proc. 12th Int. Conf. on High Energy Accelerators*, p. 481 (1983).

[5] D. Neuffer, Nucl. Instrum. Methods **A350**, 27 (1994).

[6] Particle Data Group - C. Caso et al., 'Review of Particle Physics', Eur. Phys. J. **C3** (1998).

[7] U. Fano, Annu. Rev. Nucl. Sci. **13**, 1 (1963).

[8] D. Neuffer and A. Van Ginneken, Nucl. Instrum. Methods **A403**, 1 (1998), see also Refs [1]–[5] above.

[9] D. Neuffer, 'Phase space exchange in thick wedge absorbers for ionization cooling', AIP Conf. Proc. **441**, 270 (1998).

[10] R. Cooper, Part. Accel. **7**, 41 (1975), see also Ref. [13] below.

[11] B.F. Bayanov et al., Nucl. Instrum. Methods **190**, 9 (1981).

[12] G.I. Silvestrov, 'Lithium lenses for muon colliders', AIP Conf. Proc. **372**, 168 (1996).

[13] R. Palmer and R. Fernow, Lectures on μ^+–μ^- Colliders, (Ionization Cooling) presented at Vanderbilt U., January 1999.

[14] B.A. Shadwick, S. Wurtele, A.M. Sessler, C. Celata, and P.B. Lee, Paper TUP101, *Proc. 1999 PAC*, New York, NY (1999).

[15] R. Palmer, 'Chromaticity Optimization Studies', unpublished (1998).

[16] J.C. Gallardo et al., paper THP35, *Proc. 1999 PAC*, New York, NY (1999).

[17] D. Neuffer and A. Van Ginneken, *Proc. 1997 PAC*, Vancouver, BC p. 417 (1997).

[18] P. Spentzouris and D. Neuffer, paper THP56, *Proc. 1999 PAC*, New York, NY (1999).

[19] R.C. Fernow et al., to be published in *Proc. 8th Workshop on Advanced Accel. Concepts*, Baltimore, MD (1998).

[20] T.A. Vsevolozhskaya, 'Kinetics of 3-D Ionization Cooling of Muons', Budker INP 98-48 (1998).

[21] V. Balbekov, paper THP83, *Proc. 1999 PAC*, New York, NY (1999).

[22] R. Palmer, unpublished (1996).

[23] V. Balbekov, paper WEBR5, *Proc. 1999 PAC*, New York, NY (1999).

[24] A. Van Ginneken, Nucl. Instrum. Methods **A362**, 213 (1995); D. Neuffer and A. Van Ginneken, Nucl. Instrum Methods **A403**, 1 (1998); and paper 4W.31, *Proc. PAC 1997*.

[25] R. Fernow, ICOOL (unpublished) 1998, see also paper THP31, *Proc. 1999 PAC*, New York, NY (1999).

[26] P. LeBrun and P. Spentzouris, DPGeant Simulations, unpublished (1998).

[27] K. Nagamine, 'New μ^+–μ^- cooling for μ^+–μ^- colliders and possible realization at JHF/KEK', AIP Conf. Proc. **441**, p. 295 (1998).

[28] M. Muhlbauer et al., 'Frictional cooling: latest experimental results and first application', Nucl. Phys. B (Proc. Suppl.) **51A**, 135 (1996).

[29] A.A. Mikhailichenko and M.S. Zolotorev, Phys. Rev. Lett. **71**, 4146 (1993).

[30] S. Geer, spokesperson, et al., FNAL Proposal P904 (1998).

5 ACCELERATION

The acceleration system for the μ^+–μ^- collider is the largest system of the μ^+–μ^- collider complex and is expected to be the most expensive component in high-energy colliders [1, 2]. In this chapter we will describe some of the options in accelerator design and then present reference acceleration scenarios. The acceleration scenarios are designed to accelerate μ^+–μ^- beam up to the 50–70 GeV per beam energies needed for the first muon collider (Higgs factory), and be extendable to $\sim$ 250 GeV per beam for a higher-energy Top+ collider, and from there to the $\sim$ 2 TeV per beam energies needed for a very high-energy collider.

While acceleration of muons to high energy is generally considered possible, an optimal and cost-effective acceleration complex must be developed [3]. In the reference scenarios described below, a low-frequency linac would take the beam from the end of cooling to gigaelectronvolt energies followed by two recirculating-linac systems to take the beam to 50–70 GeV. From there a sequence of very-rapid cycling synchrotrons or higher-energy recirculating linacs could take the beam to multi-TeV energies.

In the following discussion, possible acceleration options are described. From current considerations, some sample scenarios are developed. Variations in acceleration and possible difficulties are discussed, and topics for further study and research are described.

5.1 Acceleration options

In this section we discuss the various choices in μ^+–μ^- acceleration. Acceleration must be completed before muon decay ($\tau_\mu = 2.2$ μs at rest, or 2.2 ms at $E_\mu = 100$ GeV). This constraint can be written as the equation:

$$eV'_{RF} \gg \frac{m_\mu c^2}{L_\mu} \cong 0.16 \text{ MeV/m} ,$$

where eV'_{RF} is the acceleration rate, and L_μ is the μ decay length (660 m) [2]. Relatively fast acceleration is required. Acceleration in a single-pass linac is possible; however, it would be expensive and would not use a critical advantage with muons: the lifetime is sufficiently long to permit multipass acceleration. Three alternative multipass methods have been developed: recirculating linacs (RLAs), fixed-field multiple orbit recirculators (FFAG/MORs) and very rapid-cycling synchrotrons (RCSs).

In a RLA (like the CEBAF accelerator [4]), the beam is circulated through the same linac for several passes, with separate energy-matched fixed-field return paths for each pass. In a CEBAF-like RLA, each return path is optically independent and can be separately designed. In initial lattice design the return arcs are designed as similar AG systems with the same dipole layouts, but with differing quadrupole strengths to allow separate arc tunability and chronicity matching. Two configurations for the RLA have been considered: (1) the racetrack configuration (like CEBAF), in which the accelerator consists of two parallel linacs with semicircular multipass return arcs (Fig. 5.1), and (2) a 'dogbone' configuration in which the muons pass back and forth through a single linac with turnaround arcs at each end [5]. In the racetrack configurations all of the return arcs fit within the same tunnel, while in the dogbone separate paths for each return arc are preferred, and it is possible to make the lower-energy return paths shorter. While in the dogbone each return arc requires a complete turnaround of the beam, the number of entrances/exits of the linac per length is reduced by a factor of two. While a dogbone might be preferable at low energies, a racetrack configuration appears to be preferable for higher-energy RLAs, where tunnel costs are significant. Also control of longitudinal motion is easier with the racetrack.

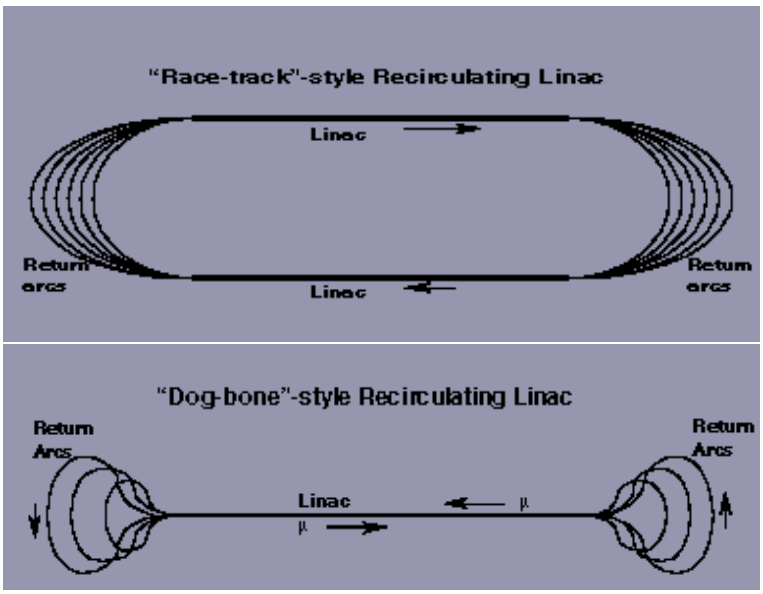

Fig. 5.1: Sketches of 'racetrack' and 'dogbone'-style recirculating linacs, showing linacs and return arcs. Both configurations will also require injection and extraction (not shown).

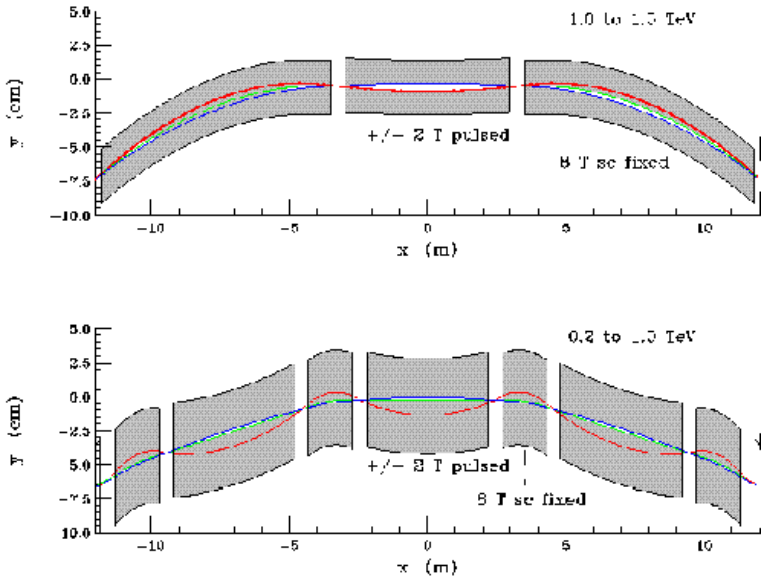

Fig. 5.2: View of a $\mu^+\mu^-$ collider facility with a sequence of four RLAs for acceleration.

More recently, a variation of the fixed-field alternating-gradient (FFAG) concept [6,7] is being considered, called the multiple-orbit recirculator (MOR). In the MOR the return fixed-field transports between accelerating segments are designed with a large energy acceptance, so that separate energy turns can pass through the same transport, with energy-dependent orbits and focusing properties. The MOR arc transports are quadrupole-dominated, with relatively large apertures to accommodate the many turns. Unlike the FFAG, the betatron phase advance changes from turn to turn. Lattices with the broad momentum acceptances and required synchronicity are being developed [8,9].

In a RCS, the beam is also multipass-accelerated through RF systems, and the beam returns in a single arc (like the FFAG/MOR), but the magnetic field is ramped to match the

beam energy increase (as in conventional synchrotrons). More acceleration turns are possible with an RCS (reducing RF requirements), since each turn uses the same transport. Construction costs could be reduced by the single return transport and reduced RF length, but with higher power costs and technical challenges associated with the very rapid-cycling needed to match the muon lifetime. A complete acceleration system would include a sequence of RLAs and/or RCSs, each of which would increase the beam energy by a large factor (five to ten times). RLAs are favoured for the lower energy accelerators, while at higher energies the longer lifetime permits practical magnet cycling rates, and rapid-cycling scenarios are preferred.

Figures 5.2 and 5.3 show μ^+–μ^- collider layouts, with a sequence of accelerators (linac + 4 RLAs in Fig. 5.2, linac, RLA, and 2 RCSs in Fig. 5.3) taking the beam from the end of cooling to full energy. The figures are approximately to scale.

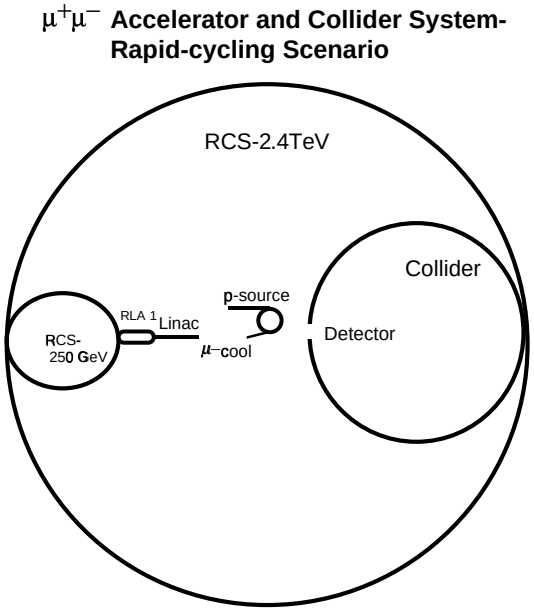

Fig. 5.3: Overview of a μ^+–μ^- collider system (approximately to scale), including multistep acceleration components (linac, RLA, 250 GeV RCS, 2.4 TeV RCS).

Details of an acceleration scenario, particularly the initial stages of that scenario depend critically on the beam parameters at the end of cooling. Since optimum cooling scenarios have not yet been specified, some flexibility in scenario construction is presently indicated. In the present discussion, we assume that at the end of cooling the bunch has been somewhat lengthened to provide additional transverse emittance cooling at the expense of longitudinal emittance. Typical parameters may have $\epsilon_{t,N} \cong 10^{-4}$ m-rad, with a bunchlength of between 0.5 and 0.1 m, with $\delta p/p \cong 10\%$. An initial linac would accelerate the beam from 100 MeV to 1 GeV energy, while compressing the bunch length to the 0.05–0.1 m region. At this point the beams would be injected into multipass acceleration systems.

5.2 Example: 1 → 50 → 250 → 2000 GeV acceleration scenario

As an example, we present a reference scenario for acceleration of muons from the cooling channel output to 50–70 GeV, with a plan for addition of a RCS to take the beam to 250 GeV, and a further RCS to take the beam to 2000 GeV. The basic acceleration elements in this scenario are multiple transport RLAs up to 70 GeV, with RCS systems for higher energies. Future R&D development may shift this scenario toward the use of MOR lattices for the RLAs and/or more RCS acceleration.

The acceleration scenario parameters are shown in Table 5.1. It begins with a linac system that takes the muons from 0.2 to 1.5 GeV, while compressing the rms beam bunch length from $\sim$ 0.5 m to $\sim$ 8 cm. A bunch compression arc then injects the beam into a sequence of two racetrack RLAs to bring the muons to 50–70 GeV, the appropriate energy for the first muon collider (Higgs factory). The RF frequency increases (using shorter RF wavelengths) in this sequence with increasing energy systems, since the bunch length decreases following adiabatic damping. The arcs in the RLAs are tuned off isochronous by relatively small amounts ($M_{56} \sim 0.2$–0.5 m), and the acceleration is off-crest by 20° in each RLA, to obtain stable oscillations within an accelerating RF bucket. While, in principle, phase and M_{56} can be arbitrarily set from turn to turn in a RLA, we have kept fs constant throughout and limited the M_{56} variation. (Larger changes may be helpful in capturing a more diffuse beam.) The first RLA would use Cu cavities with SLEDs, while superconducting RF (SRF) could be used for the second RLA (at 400 MHz). The bunch length here is 0.5 cm (rms) with an energy width of $\sim$ 0.5 GeV. A phase rotation with injection into a collider ring would obtain the $\sim$ 4 cm $\times \sim 0.06$ GeV beams needed for the high-luminosity 50×50 GeV first muon collider.

Table 5.1:
Parameters of a RLA + RCS muon accelerator system

	Linac	RLA1	RLA2	RCS1	RCS2
E (GeV)	$0.1 \rightarrow 1.5$	$1.5 \rightarrow 10$	$10 \rightarrow 70$	$70 \rightarrow 250$	$250 \rightarrow 2000$
f_{RF} (MHz)	$30 \rightarrow 100$	200.0	400	800	1300
N_{turns}	1	9	11	33	45
V_{RF} (GV)/turn	1.5	1.0	6	6.5	42
C_{turn} (km)	0.3	0.16	1.1	2.0	11.5
τ (ms)	0.0013	0.005	0.04	0.22	1.73
ϕ_S		20°	20°	30°	24°
M_{56}/arc (m)		$0.2 \rightarrow 0.5$	0.2	0.3125/2	0.94/2
$\sigma_{z,beam}$ (cm)	$50 \rightarrow 8$	$4 \rightarrow 1.7$	$1.7 \rightarrow 0.5$	$\rightarrow 0.25$	$\rightarrow 0.12$
$\sigma_{z,beam}$ (GeV)	$0.005 \rightarrow 0.033$	$0.067 \rightarrow 0.16$	$\rightarrow 0.58$	$\rightarrow 1.14$	$\rightarrow 2.3$
Decay survival (%)	95	93	94	93	90

This second RLA could be followed by a RCS for $70 \rightarrow 250$ GeV acceleration (at 800 MHz) which would use superconducting RF cavities. From that energy, TESLA SRF cavities (1300 MHz) can be used to accelerate the beam to 2 TeV in a second RCS. The beam continues to decrease in bunch length as the beam accelerates. In the RCS lattices, large γ_T values are used ($\gamma_T = 80$ and 120, respectively), and off-crest acceleration maintains phase stability.

Figure 5.4 shows results of simulations of longitudinal motion through this acceleration system. The beam remains adequately matched throughout the system, with minimal phase space dilution. Initial beam conditions which correspond to the larger phase space of the high-L, large-δE 50×50 GeV collider were used. If the smaller phase space of the narrow-band collider is used, still less dilution would occur, although somewhat different acceleration bunching and debunching parameters would be used.

This example is just one of a broad range of possibilities which are being developed. Acceleration scenarios based entirely on RLAs have been developed [2]. Acceleration which relies on higher frequency RF systems could be developed, particularly if initial bunch lengths are short. However, wake field effects are an increasing difficulty at higher frequencies. Conversely, larger initial bunchlengths would make lower-frequency acceleration more attractive.

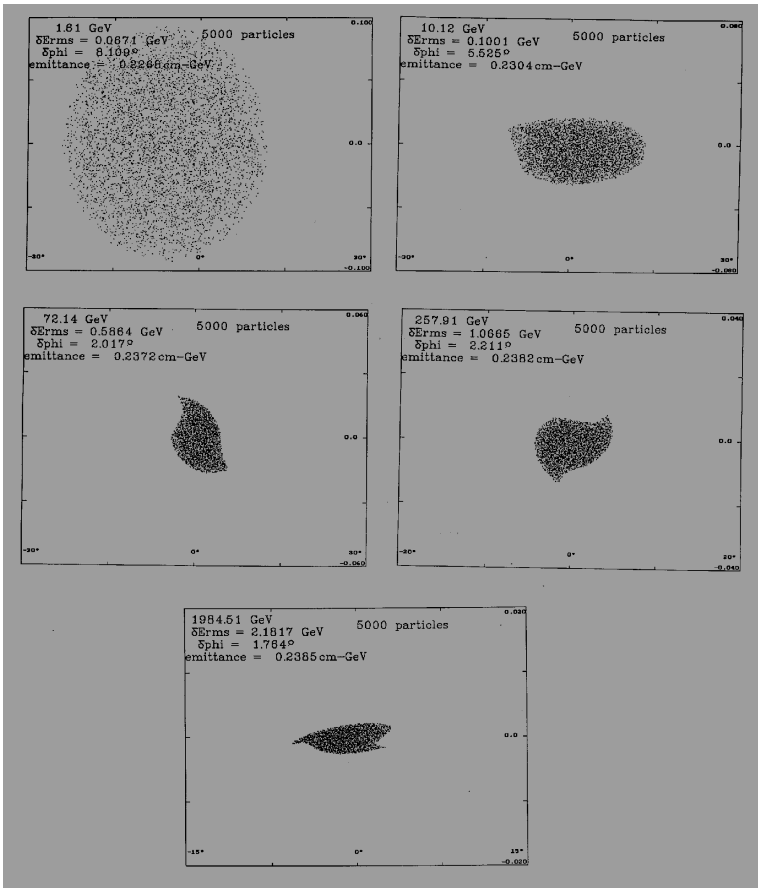

Fig. 5.4: Simulation results of longitudinal motion through a 2-RLA + 2-RCS acceleration system, taking the beam from 1.5 GeV to 2 TeV (see Table 5.1).

5.3 FFAG-MOR acceleration scenario development

Recent research is exploring the possibility of fixed-field multi-orbit recirculators for muon acceleration. The designs are based on FFAG concepts developed at MURA in the 1950s [6,7] but with some modifications for the different constraints in muon acceleration.

The fixed-field accelerators are quadrupole dominated with relatively weak bending components, in order to keep the beam within the same beampipe. This makes the circumference relatively large, and therefore increases beam decay.

As an example, A. Garren et al. have developed a scaling radial sector FFAG lattice for a 16–64 GeV accelerator, with a central design energy of 40 GeV [8]. Parameters of this example are displayed in Table 5.2. A cell of the lattice contains a (horizontally) focusing F magnet, a defocusing D magnet, and short drift spaces. Each of the magnets has $B(\rho) \propto \rho^n$, where ρ is the local curvature radius, so that the field index $n = -(\rho/B)(dB/d\rho)$ is independent of energy. The F and D magnets have opposite signs of both B and n. With this scaling the lattice has the same tune for all energies (as in the MURA FFAGs). With the strong focusing, the dispersion is very small (3.9 cm) and the beam orbit moves by only 5.4 cm over the energy swing, and dispersion is matched to zero in the straight sections. The ring periodicity is relatively high. Magnetic fields are strong, reaching ~ 9 T at the quadrupole aperture limits.

Table 5.2
Parameters of a FFAG μ^+–μ^- accelerator [8]

Beam energy (initial, central, final)	$16 \rightarrow 40 \rightarrow 64$ GeV
Circumference, periodicity (m)	1356 m, 4
Cell length, number of cells	3.51 m, 204
Betatron amplitudes ($\beta_{x,max}, \beta_{y,max}$), dispersion η	7.8 m, 15.3 m, 3.87 cm
Quad lengths, L_F, L_D	1.79, 1.3
Magnetic radius ρ	27.5 m
Tunes ν_x, ν_y, field index n	112.8, 25.9, 707
B (40 GeV), B′ (40 GeV)	4.86 T, 125 T/m
Straight sections (N_S, L_S)	16, 14 m
Acceleration/turn	2 GeV

With the small number of acceleration turns, constant tune is not required, and non-scaling lattices which do not require constant tune are being developed [9].

The primary unresolved problem in multi-orbit recirculators is in matching beam phases to the RF acceleration on each turn and in maintaining phase stability. Lattices are typically nearly isochronous, and the previous design allows introduction of pulsed path length chicanes to maintain phase. However, lattice designs which naturally preserve phase stability would be preferred. Some control of RF parameters and filling may be needed to adjust phases on a turn-by-turn basis, matched to the acceleration cycle.

5.4 RF/SRF

While the gradients needed in the acceleration systems are not excessive ($\geq$ 10 MV/m), these are larger than shown by previous experience at the lower frequencies, and the high-peak power pulsed operation poses power handling difficulties at lower energies, while high peak-current presents collective effect (wake-field) difficulties at higher energies. Higher gradients and efficiencies in all sections would improve performance.

For lower energies (where muon lifetimes are short and bunches are relatively long) copper cavities at relatively low frequencies (f $<$ 400 MHz) would be used. Because the instantaneous power is large, RF options such as using SLED (SLAC Energy Doubler) pulse formation, and allowing RF gradients to sag on successive passes are suggested. Liquid nitrogen temperature operation is also possible. Adaptation of existing 200 MHz acceleration systems, as well as development of novel structures, has been discussed [10].

At higher energies and higher frequencies, SRF appears to be preferred. The SRF would operate in pulsed mode, matched to the acceleration time of up to a few milliseconds. This pulse structure is similar to the multibunch acceleration mode planned for TESLA (25 MV/m at 1300 MHz designs), and studies indicate that this design could be adapted to μ^+–μ^- acceleration. At lower frequencies, structures such as the CERN 350 MHz SRF cavities could be used. These cavities have been tested in pulsed-mode operation, and tests indicate that pulsed acceleration fields of $>$ 10 MV/m are possible [12].

The high single-bunch intensities required for high intensities imply large higher-order-mode losses in the SRF cavities and large wake-field effects from the short, high-intensity bunches. HOM load designs adapted from SRF experience could be used. HOM loads and wake-fields are expected to vary as $1/a^2$ and $1/\lambda^2$ and $1/\sigma^{1/2}$, where a is the cavity aperture, λ is the acceleration wavelength and σ is the bunch length [13,14]. Calculations indicate that the wake-fields would limit bunch intensities to $\sim 2 \times 10^{12}$ with 1300 MHz SRF in a RLA scenario. The longitudinal dynamics is microtron-like or synchrotron-like and off-crest acceleration enables compensation of the linear part of the wake-fields, with synchrotron-like phase stability

[2]. However, a more accurate and complete model of wake-field effects, integrated with the beam-loading and nonlinear phase-stability considerations, should be developed.

5.5 Beam transport and magnets

Beam transport for RLAs follows the model of the CEBAF accelerator. The layout is a racetrack with linacs in the straight sections and multipass return arcs. At the ends of the linacs the multipass beam lines are recombined. A pulsed magnet at each separation/recombination point could be used to guide the beam into an energy-matched return arc. Or, as at CEBAF, fixed-field beam separators and recombiners could be placed at the end of each linac.

Some initial lattice design concepts for RLAs are being developed. The basic return arc unit would be a FODO lattice, but with the quadrupole strengths varied in order to perturb the arc dispersion function and obtain nearly isochronous motion around the arcs, and the nonisochronous transport matrix element M_{56} would be tuned to optimize the longitudinal bunching scenario. The arcs are dispersion matched by setting the arc phase advance to a multiple of 2π. Arc designs based upon the flexible momentum compaction (FMC) module can also be used. Also strong-focusing lattice modules with broad momentum acceptances, based upon the quadrupole-dominated lattices used in FFAG configurations, could be used, particularly for the initial turns of low-energy RLAs, where momentum acceptances of up to $\pm 10\%$ would be required.

Permanent, ferric or superferric (< 2 T), or high-field superconducting magnets could be used for RLAs. The lower field magnets may be economic for initial turns, while high-field magnets minimize particle travel times, and therefore decay losses. Designs for multiaperture superconducting magnets suitable for RLAs have been developed by S. Kahn et al., and superconducting magnets with as many as 18 apertures with 0.7–7 T fields have been designed [15]. A variety of magnet configurations can be developed; cost/performance optimization will be needed in developing a final choice.

A more difficult challenge is in the design of very rapid-cycling configurations suitable for μ^+–μ^- rapid cycling synchrotrons. E. Willen has designed a pulsed current 4 T magnet for acceleration to 250 GeV in 360 μs [16]. (A slightly faster cycle (220 μs) would be required for the first RCS of Table 5.3.) Efficiency favours use of ferric materials in rapid-cycling magnets, although this would limit peak magnetic fields to $\sim$ 2 T. Average field can be increased by interleaving magnets cycling from -2 T to 2 T with fixed-field 8 T superconducting magnets. The scenario of Table 5.3 uses such a configuration, and magnet cycling rates of $\sim$ 250 Hz would be sufficient [17]. Figure 5.5 shows hybrid magnet configurations; the energy-dependent closed orbits are also displayed.

Table 5.3
Parameters of a two-stage 0.2 $\rightarrow$ 1.5 TeV VRCS scenario

Parameter	RCS1	RCS2
Energy	0.2 $\rightarrow$ 1.0	1.0 $\rightarrow$ 1.5
Mean B-field	0.7 $\rightarrow$ 3.6	3.6 $\rightarrow$ 5.4
Frac. 8 T sc	27%	57%
Circumference	9 km	9 km
Number of turns	50	32
V_{RF}/turn	18 GV	18 GV
Cycling time	250 Hz	400 Hz
Decay losses	15%	3%

Faster pulsing magnets would require special materials to minimize energy losses from eddy currents. Options include silicon steel, metglass laminations, or finemet laminated tape or powdered solid. A 30-micron metglass lamination suitable for several kHz cycling has been developed [18]. While some initial concepts of fast pulsing magnets have been discussed, detailed designs and constructed prototypes must be developed, and the practical limits of recycling scenarios should be determined.

5.6 Acceleration research needed

As discussed above, possible acceleration configurations have been developed, and critical longitudinal motion simulations have been performed. These calculations support the general feasibility of acceleration of muons from cooling to collider energies. However, the designs of acceleration systems have not been fully detailed and much work would be needed to obtain a buildable design [19]. Complete transport lattices for linacs and return arcs have not yet been derived, and 6D phase space-tracking of beams through the accelerators has not been attempted. Also the geometry of combining and separating multipass beams has not been worked out and optimized.

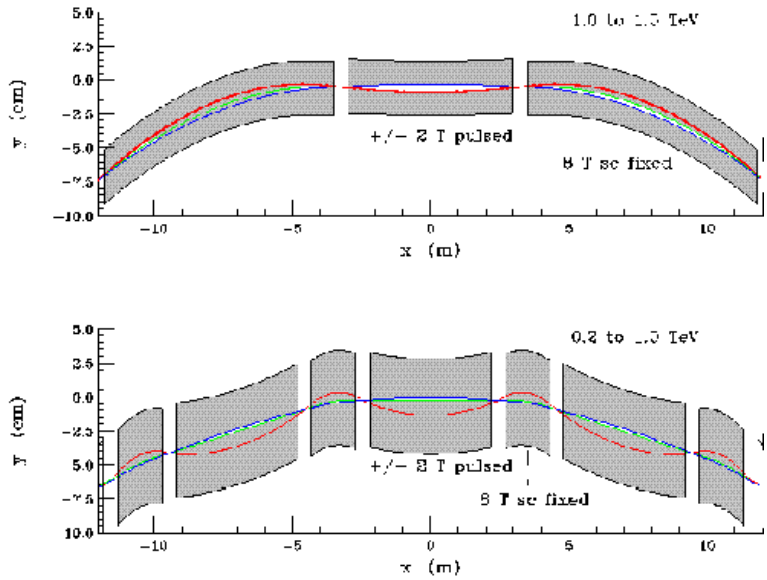

Fig. 5.5: Overview of hybrid superconducting + rapid-cycling dipole configurations for rapid-cycling synchrotron configurations. Configurations suitable for cycling from 0.2 to 1 TeV and 1 to 1.5 TeV are shown, as well as closed orbits at the extremes of the cycling ranges; accelerator parameters using these magnets are also displayed.

RF requirements and systems have been specified at only the rudimentary requirements level, and have not been developed to a constructable level. Optimal configurations and choices of normal or superconducting RF must be developed, as well as more optimal choices in acceleration frequencies. The simple wake-field models used in the initial simulations should be expanded to obtain more realistic systems, and more precise calculations of wake-field effects must be developed.

Rapid-cycling systems have only been outlined at the simplest conceptual level. Prototype magnet design and testing is needed to test the limits of cycling rate and field strengths. Successful magnet concepts must then be specified in terms of stable beam transport configurations, including focusing and transport matching. While beam is stored for only a few turns, the individual bunch intensities are large enough that the possibility of single-bunch instabilities must

be considered and calculated. The larger number of passes in a RCS places greater demands on the RF systems and HOM loads, particularly for superconducting systems.

The concept of a fixed-field multipass accelerator needs further research, particularly in magnet design and matching, and in acceleration stability, before a candidate configuration can be proposed.

5.7 Summary

It is generally expected to be possible to accelerate muons from low to high energies, and several scenarios for that process has been developed. The most conservative acceleration scenarios would use linacs and recirculating linacs for acceleration; RCS and FFAG-MOR options require substantially more component and scenario development to be considered practical. The research efforts must be extended to include more complete design studies for all of the various options, and integrated with practical RF acceleration components. Once the research specifies buildable designs, cost/complexity criteria and optima must be applied to obtain practical solutions.

References

[1] $\mu^+\mu^-$ Collider - A Feasibility Study, BNL-52503, Fermi-Lab-Conf.-96-092, LBNL-38946 (1996), presented at the *Snowmass 96 Workshop* (1997).

[2] D. Neuffer, Nucl. Instrum. Methods **A384**, 263 (1997).

[3] D. Neuffer, 'Acceleration to collisions for the μ^+–μ^- collider', *Proc. Montauk Workshop*, AIP Conf. Proc. **372**, 315 (1996).

[4] CEBAF Design Report, Newport News, VA, (May 1986).

[5] D. Summers, unpublished, (1998).

[6] K.R. Symon, D.W. Kerst, L.W. Jones, L.J. Laslett, and K. Terwilliger, Phys. Rev. **103**, 1837 (1956).

[7] L.J. Laslett, Science **124**, 781 (October 26, 1956).

[8] A. Garren, C. Johnstone, and W. Wan, paper THP50, *Proc. 1999 PAC*, New York, NY (1999).

[9] C. Johnstone, W. Wan and A. Garren, unpublished, (1999).

[10] Y. Zhao et al., 'A normal conducting accelerator for a muon-collider demonstration machine', *Proc. PAC 1997*, Vancouver, BC, p. 408 (1997).

[11] Q.S. Shu et al., *Proc. 1997 PAC*, Vancouver, BC, p. 2906 (1997).

[12] H.P. Kindermann and M. Stirbet, CERN-SL-97-64 (1997).

[13] A. Mosnier and O. Napoly, *Proc. 15th Int. Conf. High Energy Accelerators*, ed. J. Rossbach, p. 963 (1992).

[14] A. Novokhatski and A. Mosnier, *Proc. PAC 1997*, Vancouver BC, p. 467 (1997).

[15] S. Kahn, G. Morgan, and E. Willen, 'Recirculating arc dipole for the 2+2 TeV μ^+–μ^- Collider', unpublished, (1996).

[16] E. Willen,'Pulsed Dipole Magnets for the Muon Collider', Magnet Note 555-31, BNL May 1996, *Snowmass Proc.*, p. 246 (1997).

[17] D. Summers et al., *Proc. PAC 1997*, Vancouver, BC, p. 624 (1997).

[18] D. Summers, unpublished, (1997).

[19] J.S. Berg et al., *Proc. 1999 PAC*, New York, NY, (1999).

6 COLLIDER AND DETECTOR

6.1 Collider introduction

After acceleration to full energy, the μ^+ and μ^- bunches are inserted into a storage ring for multiturn collisions at full energy until μ-decay. The number of storage turns before decay is ~ 300 B, where B is the mean ring bending field in T, or ~ 2000 turns at B = 6.7 T. The relatively short beam lifetime means that long-term stability in the beam dynamics and collective effects is not required. However, high luminosity requires that the beams be focused to small spots and short bunches at the interaction points (IPs), and that implies extreme focusing and high beam densities which may still test the limits of the short-term stability requirements.

In this chapter we discuss lattice designs for 50 GeV and 2 TeV collider rings, and these examples cover the range of the types of collider rings which may be developed. Lattice parameters for these two cases are similar, but with some differences. The 50 GeV ring circumference is dominated by the IR region and the accompanying correction section; the arcs are relatively short. While more extreme IR focusing is required for the 2 TeV machine, the arcs are much longer and dominate the circumference. Parameters of rings designed for these two cases are displayed in Table 6.1.

Table 6.1
Parameters of μ^+–μ^- collider rings

Parameter	Symbol, unit	50×50 GeV (low δE-high L)	2×2 TeV collider
Beam energy	E_μ, GeV	50	2000
Circumference	C, m	345	8085
IR low-β^*	β^*, cm	13–4	0.3
IR quad $\beta_{\rm Max}$	$\beta_{\rm Max}$	600–1600 m	145 000 m
IR quad triplet lengths	$L_{\rm IRQ}$, m	2.8	24.8
IR quad field, aperture	$B_{\rm IR}, a_{\rm IR}$	8 T, 11 cm	12 T, 11 cm
Tune	ν_x, ν_y	5.85, 3.86	29.49, 28.99
Arc β-maximum		30 m	80 m
Dispersion (max., min.)	$\eta_{\rm max}, \eta_{\rm min}$	4, −5 m	1.5, −1.75
Dipole field (arcs)		8 T	8 T
Quad gradients (typ.)		160 T/m	260 T/m
Arc length		93 m	
Arc apertures		5 cm	4 cm
Chromatic correction	$\beta_{\rm max}, \beta_{\rm min}$	100, 0.7 m	10 000, 0.6
CC insert length	L_{cc}	27 m	274 m
CC dispersion		3.1/1 m	3.4/1.5
Momentum compaction	$\eta_p = 1/\gamma_T^2$	-1×10^{-6}	-1×10^{-5}
Beam emittance	$\epsilon = \epsilon_N/(\beta\gamma)$ m-rad		
Energy spread	δE	1.5 MeV–50 MeV	3 GeV
RF voltage, frequency			1 GV, 3000 MHz

Note: The 100 GeV Collider is designed to run in both small δE, small luminosity or higher δE, higher luminosity modes; where the parameters are different they are separated by a dash.

6.2 Lattice designs

A number of lattice designs have been developed for μ^+–μ^- colliders, and we have chosen some specific examples. In this chapter we present a design developed by C. Johnstone et al. for the 100 GeV collider [1], and a design initiated at the Snowmass Workshop for the 2 TeV collider [2]–[4]. Variations on the design components are then discussed, as well as the significant issues which are the topics of current research.

The 50 GeV ring is designed to operate in two modes: (1) a high-luminosity (high-L) mode, where emittance and beam sizes are minimized to obtain maximum luminosity with a moderately large momentum spread ($\sim 0.1\%$), and (2) a low-energy-spread (small-δE) mode, in which emittances and bunch lengths are increased, reducing luminosity, while energy spread is minimized. The small-δE ring is designed for detailed study of the Higgs boson, which is expected to have a small energy spread.

The principal difficulties in the lattice are associated with the requirements for small β^* (small beam size) at the IR centre. Figure 6.1 displays the lattice elements and betatron functions in the IR to arc region, while Table 6.1 shows lattice parameters [5]. The small β^* is obtained by strong-focusing triplets of quadrupoles on opposite sides of the IR detector. The betatron functions expand to large values in the IR quadrupoles and must be matched to modest values in the arcs. The transport from IR to arc also includes a chromatic correction section, designed to remove the large chromatic effects developing from the IR quadrupoles.

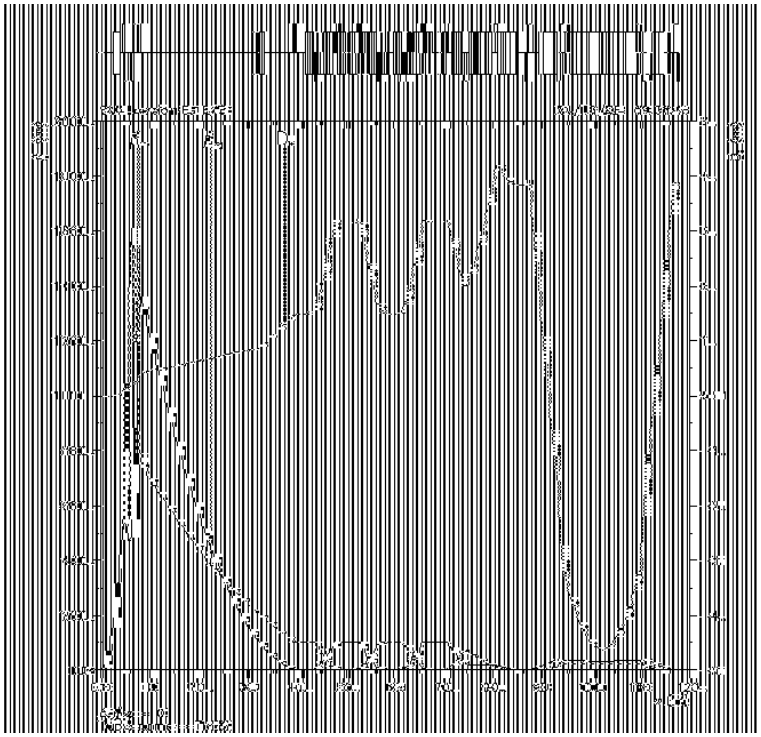

Fig. 6.1: The 50 GeV Muon Collider lattice showing half of the IR, matching in a local chromatic correction section, followed by 1 of 3 FMC arc modules in an arc.

The high-L mode requires maintaining $\beta^* \cong 4$ cm over the beam momentum spread (σp/p $\cong 0.001$), and this requires local chromatic correction sections between the IR and the arc. The chromatic correction section consists of a transport segment with dipoles to generate dispersion, quadrupoles for focusing and sextupoles for chromaticity correction. As in linear collider chromatic correction [6], a pair of sextupoles in each plane is used, with a phase advance of π between each pair, and each pair is also a phase advance of $(2n + 1)\pi/2$ from the IR centre. An innovative module design was developed for the μ^+–μ^- collider, in which high-dispersion, high-β plateau in one plane is coupled with a deep minimum in the opposite plane, so that the corrections in each plane are strongly decoupled. The high-beta plateaux alternate between planes, and the strong decoupling of the two corrections permits interleaving of the two correction systems, and this shortens the total chromatic section. Similar chromatic correction section concepts are used for both 50×50 GeV and 2×2 TeV lattices. However, the small-

δE mode has such a small momentum spread ($\sigma_{\rm p}/{\rm p} \cong 3 \times 10^{-5}$) it does not need chromatic correction, and the sextupoles could be turned off.

Owing to the hourglass effect, the bunch length must be maintained at less than β^* (4–13 cm), and to make the bunch length more stationary it is desirable to make the ring momentum compaction small. The first-order momentum compaction $\alpha_{\rm p}$ can be written as:

$$\alpha_{\rm p} = \frac{1}{\gamma_{\rm T}^2} = \frac{\delta {\rm C}/{\rm C}}{\delta {\rm P}/{\rm P}} = \eta \frac{1}{\rm R} {\rm d}\theta$$

where η is the dispersion, and the integration dθ integrates η over the bending magnets. The dispersion is positive in the chromatic correction section, so it must be made negative in the arcs, which is an unnatural configuration. In Refs. [1, 2] the negative dispersion regions are obtained by use of flexible momentum compaction (FMC) modules [7]. Betatron functions are kept small through the use of quadrupole doublets in each of the focusing points. Relatively large negative dispersions are needed to compensate for the naturally positive values of dispersion in the chromatic correction section and the matching portions of the FMC modules. The $\alpha_{\rm p}$ can be made small enough ($\alpha_{\rm p} <\sim 10^{-6}$) in the 50×50 ring such that the longitudinal motion is sufficiently stationary over the ~ 1000 turns beam lifetime that no bunching RF is required.

In the present design only one IR is included in the ring. The opposite straight section would be a utility section which would include injection and extraction as well as the beam collimation section. The three arc modules in each arc provide only about half the ring circumference; the IR, chromaticity correction sections, and the opposite utility section fill the other half.

The 2×2 TeV ring is conceptually similar to the 50×50 lattice, but with much more extreme parameters. The low-β^* requirement is much more difficult, requiring larger and longer IR quads and more carefully tuned correction sections. The small focus at the IP ($\sigma = 2$ μm, $\beta = 0.003$ m) with the geometric and chromatic acceptance requirements is a significant design challenge. A design has been developed which uses final focusing triplets of 12 T quads (11 cm radius) where $\beta_{\rm max} = 100$ km, and chromaticity correction inserts of ~ 300 m are included on each side of the IP. Figure 6.2 shows an overview of the collider ring while Fig. 6.3 shows the IR and chromatic correction lattices, and Fig. 6.4 shows an arc FMC module. In simulation the lattice has adequate dynamic apertures of $\delta {\rm p}/{\rm p} \sim \pm 0.15\%$ with 5σ beam amplitudes.

The short-bunch requirement ($\sigma_{\rm z} \sim 3$ mm) of the 2×2 TeV collider places even stricter requirements on isochronicity in the ring to avoid bunch-lengthening and an FMC lattice for the arcs obtains $\alpha_{\rm p}$ near zero ($\alpha_{\rm p} \sim 10^{-5} - 10^{-8}$). The bunch length is, however, too short to be maintained without a bunching RF system, and the design includes an RF system to maintain the bunch length and assist in stabilizing the beam. Thus in the present example $\alpha_{\rm p} = 10^{-5}$ is chosen, and a 1300 GHz RF system with 1 GV of RF acceleration is used. An alternative system using higher-frequency, double-harmonic RF systems with reduced voltage requirements could also be developed.

6.3 Instability considerations

The peak currents associated with the high-intensity muon bunches pose the possibility of coherent instabilities. The usual synchrotron stability criteria [8] for longitudinal and transverse impedances $Z_{\rm L}$, $Z_\perp$ may be applied:

$$\left| \frac{Z_{\rm L}}{\rm n} \right| < {\rm F} \frac{{\rm E}|\eta_{\rm p}|}{{\rm e}\beta^2 {\rm I}_{\rm peak}} \left(\frac{\Delta {\rm E}}{\rm E} \right)^2 \quad ; \quad Z_\perp < \frac{4\pi {\rm m}\gamma\beta\omega_\beta {\rm c}}{{\rm e}{\rm I}_{\rm peak}} \Delta\nu \, .$$

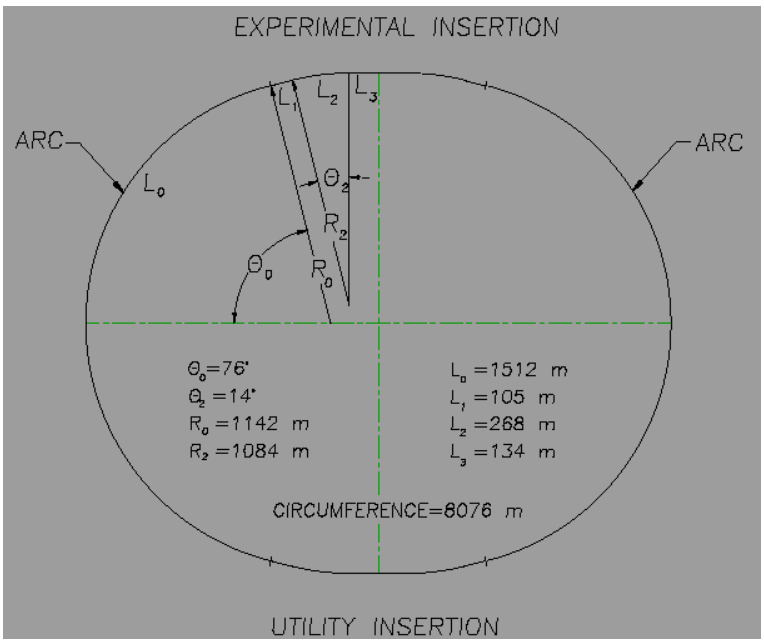

Fig. 6.2: Overview of a μ^+–μ^- collider ring, showing a 'race-track'-like configuration, with a single experimental region with detector on one side of the ring, and utility insertion at the other end. The numbers displayed correspond a 2×2 TeV collider. A 50×50 GeV ring would have a similar layout, but smaller dimensions.

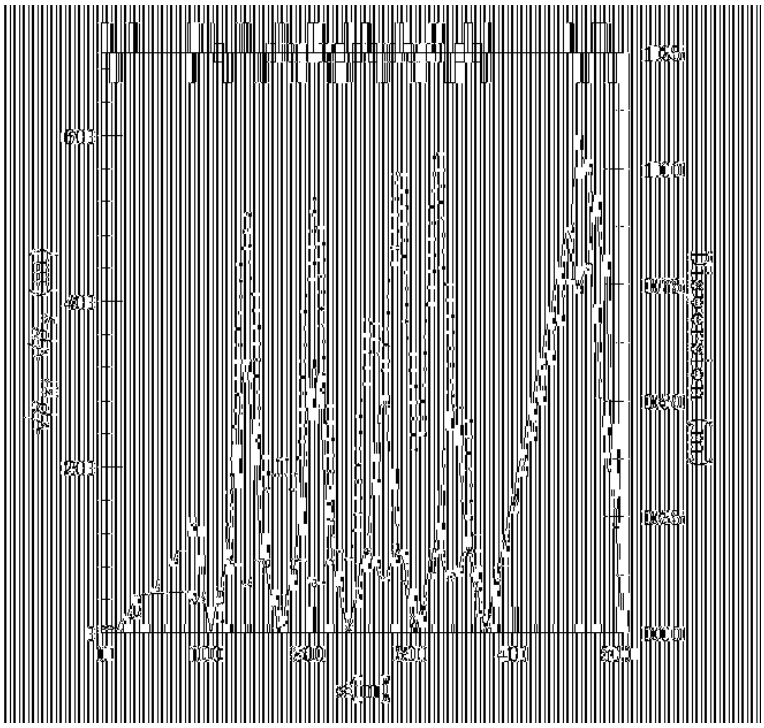

Fig. 6.3: A 2×2 TeV lattice segment (arc to IR) showing matching section, (noninterleaved) chromatic correction section and IR quad triplet focusing to very small β^* at the IR centre.

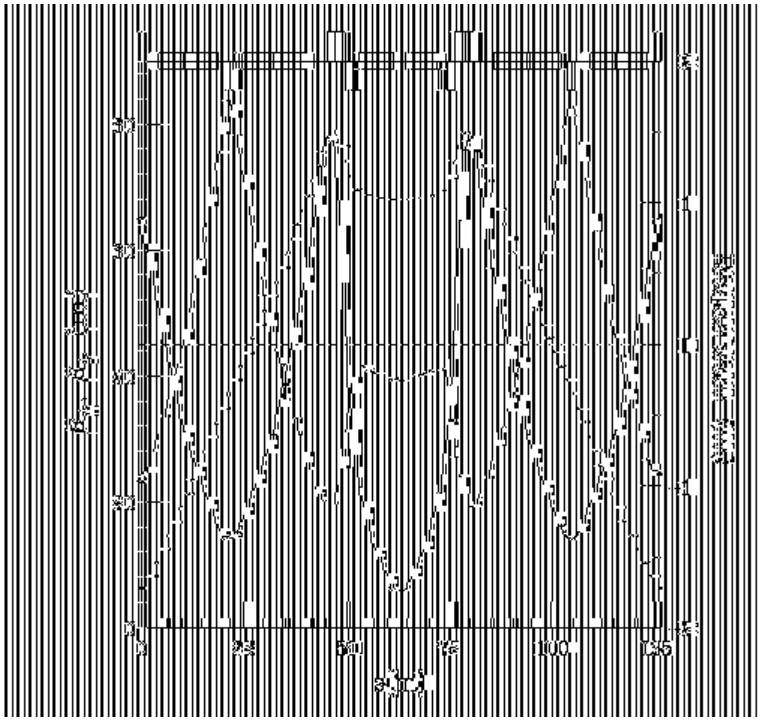

Fig. 6.4: A cell of the bending arc of the 2 TeV lattice.

However, instability growth rates need only be less than the muon luminosity lifetime, which is ~ 1000 turns [9].

For the 50×50 GeV collider the peak current with bunches of 4×10^{12} μ is 600–2000 A for bunch lengths of 13–4 cm, respectively. For $\eta_p \sim 10^{-6}$, these formulas give stability limits on Z_L/n of $\sim 10^{-4}$ Ω or less, smaller than may be expected, even in a low-impedance ring design. However, the growth rates are naturally quite small. Ng [10] and Kim et al. [11] have studied the instability behaviour of the 50×50 collider, using simulations of beam motion within broad-band impedance models. For the high-L, larger $\delta p/p$ mode, energy spread growth within the muon lifetime is much less than the beam energy spread. For the small-δE mode ($\delta p/p \cong 3 \times 10^{-5}$), relatively small impedances can lead to beam energy distortions greater than the beam energy spread, and some compensation or corrections are needed. In their simulations a double-harmonic RF system is inserted with RF voltages and frequencies designed to cancel the wakefield voltages induced by the large charge coupled to the beam impedance. (In an optimized example, RF voltages of 12.12 and 4.26 kV operating at 399 and 825 MHz were used to cancel a $Z_L/n = 0.1$ Ω impedance [11].) While this external voltage compensates the bulk of the interaction, fluctuations can still grow exponentially, and in Ref. [10] these fluctuations become comparable to δE at $Z_L/n = 1$ Ω.

The coherent stability of the 2×2 TeV collider was studied by Cheng et al. [12] and Ng [13]. The peak currents associated with bunches of 2×10^{12} μ and $\sigma_z = 3$ mm (13 000 A) pose the possibility of coherent instabilities. For $\alpha_p \cong 10^{-8}$, there is no longitudinal motion within the muon lifetime and the beam motion is e^--linac-like, with the linac length given by the muon decay length, and the beam would have linac-like instability modes with the possibility of head-tail beam breakup, but with possible solutions such as BNS damping. Obtaining $\alpha_p \cong 10^{-8}$ over the full energy spread appears difficult, and somewhat better stability is obtained for $\alpha_p \cong 10^{-5}$, where there are ~ 10 synchrotron oscillations per muon lifetime.

Cheng et al. [14] have analysed potential longitudinal and transverse instabilities in a tracking code that includes linear and non-linear α_p, wakefields (including resistive-wall, RF cavities and broad-band resonators), and μ-decay. They find acceptable dynamics at $Z_L/n = 0.1\ \Omega$ with $\alpha_p = -10^{-5}$, $\delta p/p = 0.15\%$, and 1 GV of 3000 MHz RF. (Synchrotron dynamics with negative α_p was preferable to isochronous motion.) The simulations did not include advanced stabilization methods such as BNS damping, multiharmonic RF, alternating chromaticity, etc., and these should be considered in future simulations.

6.4 Beam-beam interaction

Another critical limitation in collider rings is set by the beam-beam interaction, the nonlinear interaction at the collision points. The beam-beam tune shift $\Delta\nu_{BB}$ is given by:

$$\Delta\nu_{BB} = \frac{N_\mu r_\mu}{4\pi\epsilon_N} ,$$

and is chosen to be ~ 0.05 for the 2×2 TeV collider at the parameters of Table 6.1. Simulations by P. Chen [15] and by M. Furman [16] have shown some hour-glass and disruption effects but general stability with the beam-beam interaction for the μ-lifetime. The beam-beam tune shift is somewhat smaller for the 50×50 GeV collider, because larger ϵ_N is used. Somewhat larger $\Delta\nu_{BB}$ than 0.05 can be tolerated in the colliders; M. Furman has presented simulation results for $\Delta\nu_{BB} = 0.05$, 0.10 and 0.15 and only the largest value shows any luminosity loss.

Stupakov and Chen [17] and Skrinsky [18] have suggested that even larger $\Delta\nu_{BB}$ could be tolerated if the collision points were immersed in a plasma or in solid Li, which would neutralize the beam-beam force. The μ-material interaction rates and multiple scattering in the plasma or Li are tolerably small within the μ-lifetime; however, detector backgrounds may increase.

6.5 Magnets for the collider

Considerable research has been devoted to the design of magnets for the collider ring. It is desirable to use as high a bending field as possible in order to reduce the ring circumference and thereby increase the number of storage turns in the muon lifetime. Thus high-field superconducting magnets are preferred. The major difficulty is that the muons decay ($\mu \to e\,\nu\,\nu^*$), and the electrons from that decay deposit energy in the beam pipe walls, and therefore into the low-temperature superconducting magnets, if they are unshielded. The total energy deposited in muon-decay electrons is $\sim 1/3$ of the beam energy. With no shielding, the average power deposited per unit length is about 2 kW/m for the 2×2 TeV machine and 300 W/m in the 50×50 GeV ring, and this is much more energy than can be absorbed at cryogenic temperatures.

The current plan is to insert tungsten shielding between the beam and the magnet body. In the simplest configuration the tungsten is in a cylindrical ring around the beam pipe, which would then be placed within a $\cos\theta$ dipole, such as that displayed in Fig. 6.5 [19]. Simulations show a reduction of the power penetrating the shield to an acceptable level of 10 W/m with 3 cm of tungsten for the 50×50 GeV ring, and with 5.5 cm for the 2×2 TeV case.

An 8-T dipole with $\cos\theta$ current coils (see Fig. 6.5) could be used in a first μ^+–μ^- collider. Designs for higher-field magnets, and magnets with more efficient shielding configurations, are being developed in the μ^+–μ^- Collider Collaboration. A design based on Nb_3Sn conductor and racetrack coils is being developed and fields up to ~ 15 T appear achievable [20]. Nb_3Sn magnets with $\cos\theta$ current coils in a block design are also being developed [21].

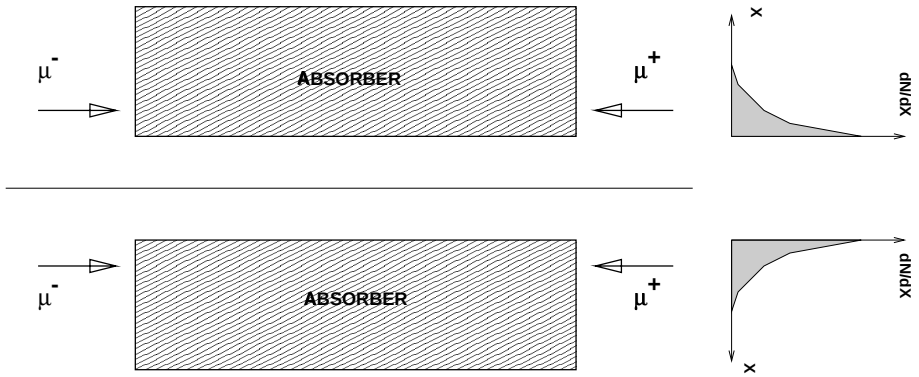

Fig. 6.5: Collimator configuration for 50×50 Collider: Energy loss in scrapers set at the desired beam acceptance aperture removes beam from the ring.

6.6 Collimator design

In order to reduce background in detectors as well as to control beam losses in the magnets, it is desirable to have collimators to remove beam that has scattered (or decayed) to larger amplitudes or energy offsets. Figures 6.6 and 6.7 show collimator designs for the 50×50 ring and the 2×2 TeV collider. For the 50×50 ring, energy loss in scrapers (5 m long steel absorbers) set at the desired beam acceptance aperture removes beam from the ring. For the 2×2 TeV ring, energy loss in a short absorber is insufficient to remove the beam and a sequence of electrostatic septa and magnetic Lambertson septa is used to capture beam distribution tails and extract them from the ring (as is done for the LHC). Simulations show that the background in the IR detector is reduced by more than an order of magnitude by these scraping systems [22,23].

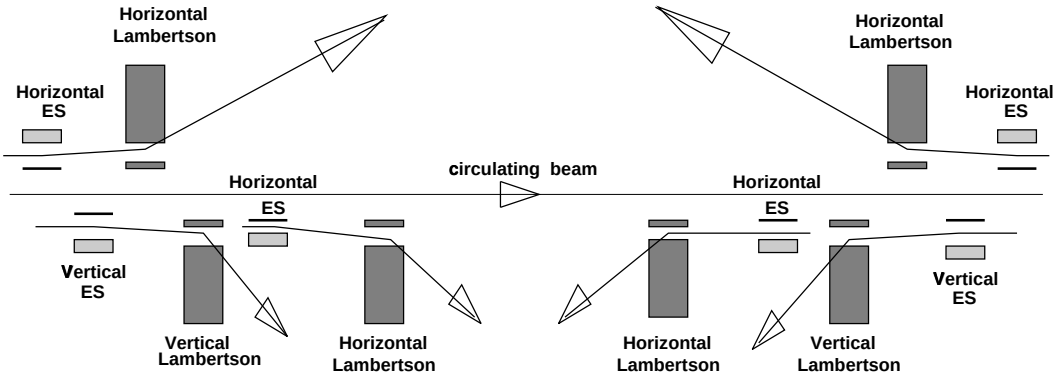

Fig. 6.6: Collimator configuration for 2×2 TeV (or high energy) Collider. Energy loss in a short absorber is insufficient to remove the beam and a sequence of electrostatic septa and magnetic Lambertson septa are used to scrape beam tails outside the ring (as is done for LHC). In an initial design the electrostatic septa and lambertsons are all 3 m long. Betatron functions are magnified to $\beta \sim 1000$ m at the collimators.

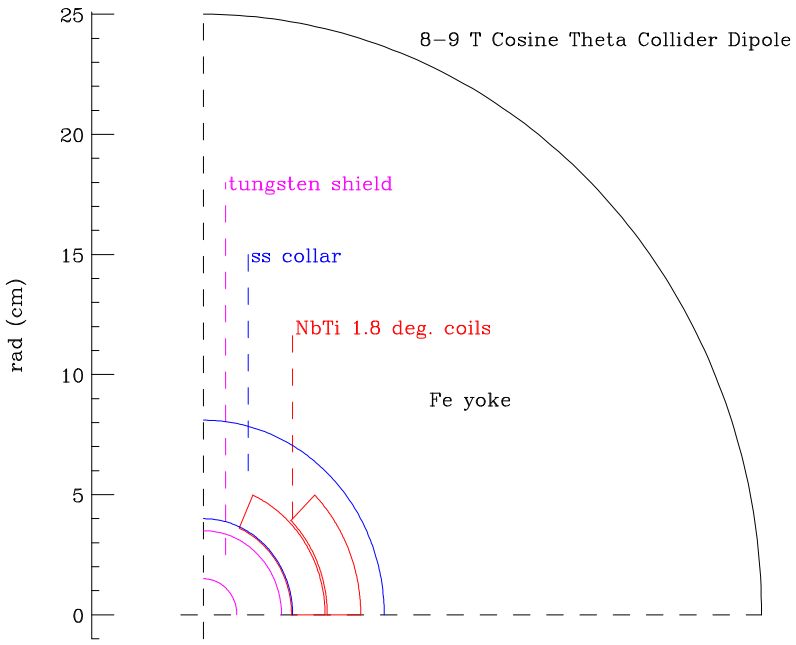

Fig. 6.7: Cross-section of a quadrant of a 9 T magnet for the 50×50 GeV μ^+–μ^- Collider. From r = 0 we see a 1.5 cm radius beam channel, a 2.5 cm tungsten shield followed by $\cos\theta$ NbTi windings within a stainless steel collar inside an iron yoke.

6.7 Detector issues

In this section we present only a short overview of the IR detector; more detailed discussions are developed in the Snowmass report [24] and in the status report [25] (and references therein), and in the lecture notes of A. Blondel [26]. The μ^+–μ^- collider detector is similar to the other multipurpose detectors being developed for e^+–e^- and p–p colliders, but with the difference that the detector must handle the background from muon decays near the IR. An overview of a strawman detector is shown in Fig. 6.8. The detector would include a solenoidal field (2^+ T) for momentum measurements. The element nearest to the IR is a vertex detector (possibly using silicon pixels) located at as small a radius as possible. Outside the vertex detector would be a tracking chamber, such as a time projection chamber (TPC). Outside that would be an electromagnetic calorimeter (possibly a lead-liquid argon system) followed by a hadron calorimeter (possibly scintillator). Outside this (and outside the solenoid) would be muon detectors, such as cathode strip chambers.

The critical issue for development of a practical μ^+–μ^- collider detector has been the problem that muons decay throughout the collider ring, including near the detectors and the detectors must be able to separate decay background from IR events. To shield the detector from decay background, cones of absorber (tungsten shielding) would be placed around the beam pipe upstream and downstream of the interaction point. Shielding is distributed around the ring, particularly near the IR and the magnets near the IR, and simulations optimizing shielding configurations versus background have been performed. Collision events differ from decay products in that the interaction point is the source of the particle trajectories. Detector components which select tracks from the IP and veto background sources are being developed. Detector designs and shielding configurations which reduce background to tolerable levels appear possible [27,28].

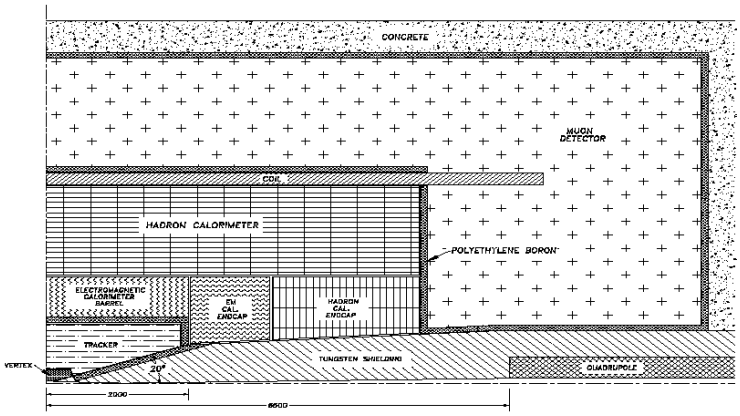

Fig. 6.8: Overview of a strawman detector for a $\mu^+\mu^-$ Collider. View shows a quadrant of the cylindrical collider detector, with vertex (collision point) at lower left corner.

References

[1] C. Johnstone, A. Drozhdin, N. Mokhov, W. Wan and A. Garren, AIP Conf. Proc. **441**, 209 (1998).

[2] C. Johnstone and A. Garren, *Proc. 1996 Snowmass Workshop on Future Directions in High Energy Physics* (1997).

[3] A. Garren et al., Nucl. Phys. B (Proc. Suppl.) **51A**, 148 (1997).

[4] C. Johnstone and A. Garren, 'A ring lattice for a 2-TeV muon collider', *Proc. PAC 1997*, Vancouver, BC, p. 411 (1997).

[5] C. Johnstone, W. Wan and A. Garren, paper THP49, *Proc. 1999 PAC*, New York, NY (1999).

[6] K. Brown, SLAC-PUB-4159 (1987).

[7] S.Y. Lee, K.Y. Ng and D. Trbojevic, Phys. Rev. **E48**, 3040 (1993).

[8] A.W. Chao, *'Physics of Collective Beam Instabilities in High Energy Accelerators'*, (Wiley and Sons, 1993).

[9] K.-Y. Ng, 'Beam stability issues in a quasi-isochronous muon collider', *Proc. Montauk Workshop*, AIP Conf. Proc. **372**, 224 (1996).

[10] K.-Y. Ng, 'Collective instabilities of the 50 × 50 GeV muon collider ring', paper THP53, *Proc. 1999 PAC*, New York, NY (1999).

[11] E-S Kim, A. Sessler and J. Wurtele, paper THP44, Proc. 1999 PAC, New York, NY (1999).

[12] E.-S. Kim, A. Sessler and J. Wurtele, MuCool 24, Phys. Rev. STAB 051001 (1999).

[13] W.-H. Cheng, A.M. Sessler and J.S. Wurtele, 'Studies of collective instabilities in muon collider rings', AIP Conf. Proc. **372**, 206 (1996).

[14] W.-H. Cheng, A.M. Sessler and J.S. Wurtele, 'Longitudinal behavior in a muon collider ring', unpublished, February 1997; W.H. Cheng et al., *Proc. PAC 1997*, p. 422, Vancouver, BC (1997)

[15] P. Chen, Nucl. Phys. B (Proc. Suppl.) **51A**, 179 (1997).

[16] M. Furman, 'The Classical Beam-beam Interaction for the Muon Collider, a First Look', LBL-38563 (1996).

[17] I. Stupakov and P. Chen, Phys. Rev. Lett. **6**, 3715 (1996).

[18] A.N. Skrinsky, unpublished (1996).

[19] N.V. Mokhov and I. Striganov, AIP Conf. Proc. **372**, 234 (1996).

[20] K. Chow et al., paper TUBR2, Proc. 1999 PAC, New York, NY (1999); R.C. Gupta et al., *Proc. 1998 EPAC.* p. 1990, Stockholm, (1998).

[21] E. Willen et al., *Proc. PAC97*, p. 3362, Vancouver, BC (1997).

[22] A. Drozhdin, N. Mokhov, C. Johnstone, W. Wan and A. Garren, 'Scraping beam halo in μ^+–μ^- colliders', AIP Conf. Proc. **441**, 242 (1998).

[23] A. Drozhdin et al., paper THP43, *Proc. 1999* PAC, New York, NY (1999).

[24] $\mu^+\mu^-$ Collider - A Feasibility Study, BNL-52503, Fermi-Lab-Conf.-96-092, LBNL-38946 (1996), presented at the Snowmass 96 Workshop (1997).

[25] C.M. Ankenbrandt et al., 'Status of muon collider research', submitted to Phys. Rev. Special Topics (1998).

[26] B. Autin, A. Blondel and J. Ellis, eds., CERN 99-02 (1999).

[27] I. Stumer, *Proc. 1996 Snowmass Workshop*, p. 453 (1996).

[28] N. V. Mokhov, Nucl. Phys. B (Proc. Suppl) **51A**, 210 (1997).

7 ν-BEAMS AND ν-RADIATION

Neutrinos are produced in the pion decay which produces the muons ($\pi \rightarrow \mu + \nu\mu^*$) as well as in the muon decays, which occur in the cooling and acceleration channels and in the collider storage ring ($\mu \rightarrow e + \nu\mu + \nu e^*$). Thus the high-intensity muon source is also a high-inten sity source of neutrinos, and the resulting neutrino beams could be a very important physics tool. However, it is also possible that very high-energy, high-intensity neutrino sources will be nontrivial radiation sources.

In this section we describe some particular neutrino beam possibilities which can be generated from a μ^+–μ^- collider complex. In particular we describe in some detail a particular scenario for the generation of neutrino beams from a muon storage ring for the study of neutrino oscillations. In a separate discussion we describe the parameters for radiation exposure from high-energy muon-induced neutrinos. Constraints on μ^+–μ^- collider development are described.

7.1 ν-beams example - μ storage ring

Recent observations from the Super-Kamiokande experiment support the proposition that neutrino oscillations exist; in particular, that the muon neutrino oscillates into an unknown particle (possibly a tau neutrino)[1]. For 2-neutrino oscillations, the oscillation probability can be expressed as:

$$P(\nu_1 \rightarrow \nu_2) = \sin^2(2\theta)\sin^2\left(\frac{1.27\delta m^2 L}{E}\right)$$

where ν_1 and ν_2 are the initial and final neutrino types, θ is the mixing angle, $\delta m^2 = m_2^2 - m_1^2$ is the difference in neutrino masses (squared) in eV^2, L the distance in kilometres and E the neutrino energy in GeV. The Super-Kamiokande results are consistent with oscillations with $\sin^2(\theta_\nu) \cong 1$, and $\delta m^2 \cong 0.003$ eV^2, with large error ranges.

Also, observations at the Los Alamos LSND detector suggest oscillations of electron neutrinos, possibly at $\sin^2(\theta_\nu) \cong 0.1$, and $\delta m^2 \cong 0.1$ eV^2 [2].

These initial obervations must be confirmed and measured more precisely, using accelerator-generated neutrino beams, and the identity of the various oscillating species determined. In particular, to identify an oscillation into tau-neutrinos it is desirable to have neutrino energy comfortably above the tau production threshold, which means energies above several GeV. Also, to see oscillations at $\delta m^2 \sim 0.003$ eV^2 or less requires L/E $\sim 10^3$ km/GeV, which implies the distance from neutrino source to detector must be ~ 1000 km or more. Candidate locations for a detector for a Fermilab μ-storage ring are at the Soudan mine (732 km away) or at Super-Kamiokande (Japan) or Gran Sasso (Italy) ($\sim 10\,000$ km away) [3].

As has previously been noted, the neutrinos from a muon storage ring provide a precisely knowable flux of neutrinos of particular species [4]. The muon decay ($\mu^+ \rightarrow e^+ \nu\, \nu^*$) provides a muon neutrino and an electron antineutrino with an angular and energy distribution that can be precisely predicted from the decay kinematics, and the intensity can be continuously monitored by tracking the muon intensity in the ring.

In Ref. [5] a muon storage ring for neutrino beams is developed as an initial step in a programme which also develops a μ^+–μ^- collider. The scenario is displayed graphically in Fig. 7.1. It starts with a proton source at parameters similar to those presented in Chapter 2 (16 GeV, 15 Hz, up to 10^{14} protons per pulse), but with the difference that the protons could be distributed about the accelerator rather than in a few bunches (i.e., with h = 12 bunches, where h is the accelerator harmonic). This means that the prebooster would not be needed. The proton bunches would be focused onto a high-intensity target with a high acceptance optics, such as the solenoidal transport and the bunch rotation RF system described in Chapter 3, and

high-intensity muon bunches would be obtained at the end of that channel. The bunches could then receive some initial transverse cooling, with the cooling designed to place the beam within the acceptance of the following acceleration and storage ring. Some cooling to fit the resulting muons within the acceptance of the following systems would follow. Transverse cooling by only a factor of ~ 3 to $\epsilon_N \cong 0.005$ m-rad should be sufficient to place the muons within the acceptance of the following accelerator and storage ring. This degree of cooling can be obtained by using the first transverse cooling section from the cooling scenario of Chapter 4 (~ 100 m of low-frequency reacceleration RF + absorbers).

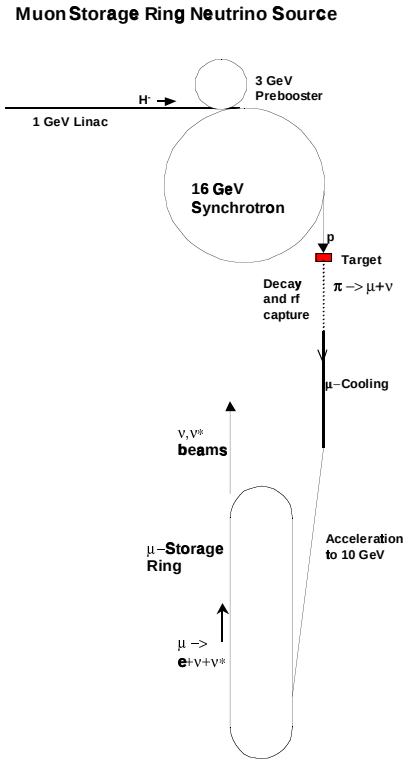

Fig. 7.1: Overview of a muon storage ring for neutrino beams facility, showing proton source, pion production and muon collection channel, muon acceleration and muon storage ring.

The muons would then be injected into an 805 MHz linac, which would capture most of them within strings of ~ 805 MHz buckets and accelerate them to 10 GeV for injection into the 10 GeV storage ring. In simulations a final energy spread of $\sigma_E/E \cong 2.5\%$ is obtained, which should be within the acceptance of the storage ring. (A bunch rotation just before injection into the storage ring could reduce this energy spread.) The storage ring is designed to have a circumference of 450 m with straight sections of ~ 180 m for a muon decay neutrino source, and a momentum acceptance of $\sigma_E/E \cong \pm 5\%$.

An estimate of the neutrino event rate can be obtained by calculating the flux of neutrinos at the detector, and multiplying it by the ν–N cross-section and then by the detector size (in nuclei). The neutrino flux is given by

$$F = \frac{Nf}{\pi \langle (L\theta)^2 \rangle} ,$$

where N is the number of muons stored in the μ^+-storage ring, f is the fraction of muons which decay in the neutrino source straight section (0.4 in Ref. [6]), $\theta^2 \cong (m_\mu/E_\mu)^2$ is the rms angle (squared) of neutrino emission, L is the distance from neutrino source to detector. The ν–N

cross-section can be estimated as $\sigma_{\nu-N} \cong 0.7 \times 10^{-38}$ E_ν cm^2, where E_ν is the neutrino energy in GeV and the average energy of a neutrino reaching the detector (directly downstream) is $\sim 2/3$ E_μ. A typical detector mass is 10 kT, or $\sim 6 \times 10^{33}$ nuclei.

Using the μ^+–μ^- collider muon source (10^{14} p, 15 Hz, 10^7 s/year, 0.1 μ/p) and a 10 GeV storage ring we obtain $\sim 10^5$ events/year at a detector at Soudan (L = 732 km), and $\sim 10^3$/year at Gran Sasso or Kamiokande. This should be more than adequate for a detailed study of neutrino oscillations at $\delta m^2 \sim 10^{-3}$ eV^2.

In this initial concept, the acceleration is done by a single-pass 805 MHz linac, and 805 MHz was chosen because high-gradient, affordable RF systems are possible at that frequency. A multipass accelerator such as a recirculating linac could also be used and may be more affordable. Also, a lower-energy neutrino source could be obtained with less acceleration and would be able to explore smaller δm^2; however, it would be below the tau production threshold.

Other scenarios for developing ν-beams from μ-storage rings, with the muons produced from a high-energy proton source, collected, cooled, and accelerated to a suitable source energy, are being developed. A workshop at Lyon (NuFact'99) will present these options, and design work toward optimizing the various concepts has been initiated [7].

7.2 Other neutrino sources

The π-decays in the $\pi \rightarrow \mu$ decay and capture transport provide a very intense source of $\sim$ 100–300 MeV muon neutrinos ($\sim 10^{22}$/year) which could be very useful in some physics experiments. The intensity would be less precisely monitored than the intensity from a μ-storage ring, but would be extremely useful in measuring muon neutrino properties, including oscillating into electron neutrino states. Similarly, muon decay in the cooling transports will also provide low-energy neutrinos.

Neutrinos will be produced from muon decay in the accelerators and colliders, with intensity enhancement in decays along straight-sections. Neutrinos at energies up to the full energy of the collider (TeV scale) will be provided. The high-energy neutrinos will be particularly useful in deep-inelastic studies of nucleon structure.

7.3 ν-radiation from μ-colliders

B. King first pointed out that neutrino radiation from the decay of neutrinos from high-intensity, very-high-energy μ^+–μ^- colliders can reach nontrivial intensity levels [8]. In this section we calculate an estimate of the radiation production, summarize more detailed production calculations (from N. Mokhov et al. [9]), and discuss methods for reducing and controlling the effect.

A first estimate of the size of the radiation deposition can be made from an estimate of the neutrino intensity multiplied by the cross section. Each muon which decays within the ring produces an electron, a muon neutrino and an electron antineutrino, and each of these particles carries $\sim 1/3$ of the initial muon energy ($E_\nu \cong E_\mu/3$). These neutrinos follow the original muon direction, with an rms opening angle of $\theta = \sim 1/\gamma$ (see Fig. 7.2).

The number of neutrinos emitted per year can be estimated by the formula:

$$N_\nu = 2 n_B N_\mu f_0 N_{cycles} P_{decay}$$

where n_B is the total of μ^+ and μ^- bunches, N_μ is the number of muons/bunch, f_0 is the cycling repetition rate, N_{cycles} is the number of cycles/year, and P_{decay} is the probability of muon decay within the ring. For typical values ($n_B = 4$, $N_\mu = 2 \times 10^{12}$, $f_0 = 15$ Hz, $N_{cycles} = 10^7$/year, and $P_{decay} = 0.5$), we obtain $N_\nu = 1.2 \times 10^{21}$/year. The cross-section for neutrino–nucleon interactions can be estimated by the formula $\sigma_{\nu-N} \cong 7 \times 10^{-40} E_\nu(m^2)$, where E_ν is the

neutrino energy in TeV. The radiation dose is the product of the number of neutrinos reaching the material, the cross-section, the neutrino energy, and the number of nucleons per kilogram ($\sim 10^3$ N_A), where N_A is the Avogadro constant. The number of neutrinos reaching a point in the plane of the collider is simply $N_\nu/(2\pi hR)$, where $h \cong 2R\theta \cong 2R/\gamma_\mu$, where h is the height of the neutrino disk (obtained from θ, the decay opening angle, which is $\sim 1/\gamma$), R is the distance from the μ^+–μ^- collider ring to the material. The resulting dosage can be written as:

$$\text{Dose} \cong \frac{N_\nu}{2\pi hR}\,\sigma_{\nu-N}\,10^3\,N_A\,E_\nu \cong 4.3\times 10^{10}\,\frac{E_\mu(\text{TeV})^3}{R(\text{m})^2}\,\text{TeV/kg/year}\,.$$

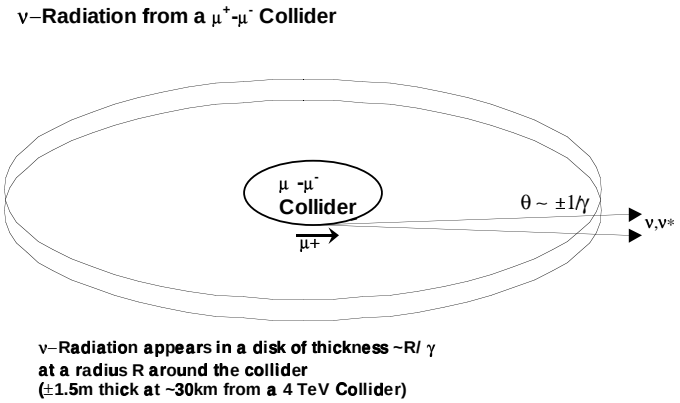

Fig. 7.2: Overview of ν-radiation from a μ^+–μ^- collider.

This can be compared with the standard energy deposition unit, the rem/yr, which is 6.25×10^4 TeV/kg/year, and one obtains a dose of ~ 7.2 mrem/year at a distance of 10 km from a collider with 1 TeV muons. Physics facilities are required to keep the exposure of the general public to radiation to low levels. In the US, there is a legal exposure limit of 100 mrem/year, and Fermilab has a Laboratory goal of keeping external exposure to less than ~ 10 mrem/year. The estimated exposure is uncomfortably close to that level with 1 TeV muons. Because of the E_μ^3/R^2 scaling, the effect is strongly dependent on energy and distance. Lower energy colliders have no problem, but higher-energy machines could be seriously constrained.

The above estimate assumes the muon orbit is a uniform circle. More intense radiation would appear downstream of straight sections of the collider ring. Strategies to mitigate the enhancement include making intermagnet straights as short as possible, and possibly keeping some bending radius (bending field B) throughout any extended sections of the ring.

The above estimate also contains many approximations which underestimate and/or overestimate the effect. Mokhov et al. have done a more detailed simulation of the generation of neutrinos in a muon collider storage ring, and of the neutrino interactions in downstream materials, including secondary particle generation and interactions [9]. Some of those results are displayed in Figs. 7.3 and 7.4.

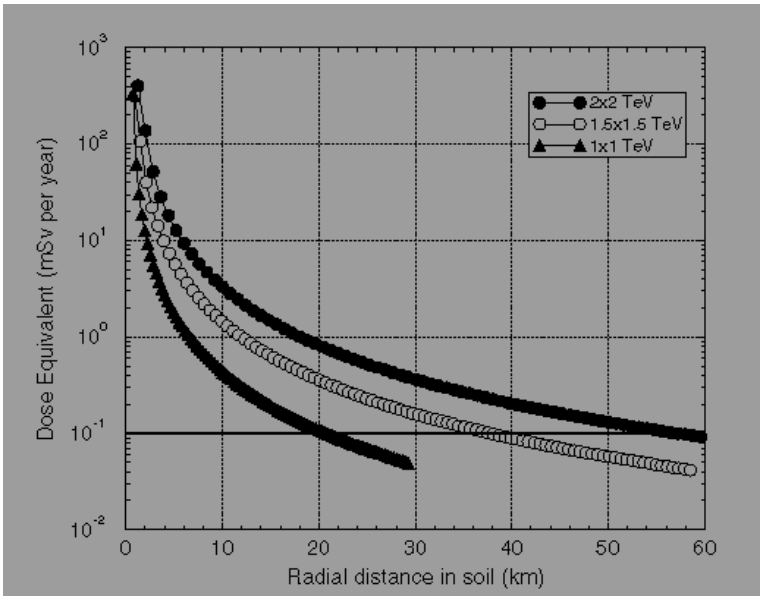

Fig. 7.3 Neutrino irradiation as a function of distance from the collider for various collider energies. The Fermilab goal of less than 10 mrem/year (0.1 mSv/yr) is indicated by the solid line at 10^{-1} mSv per year.

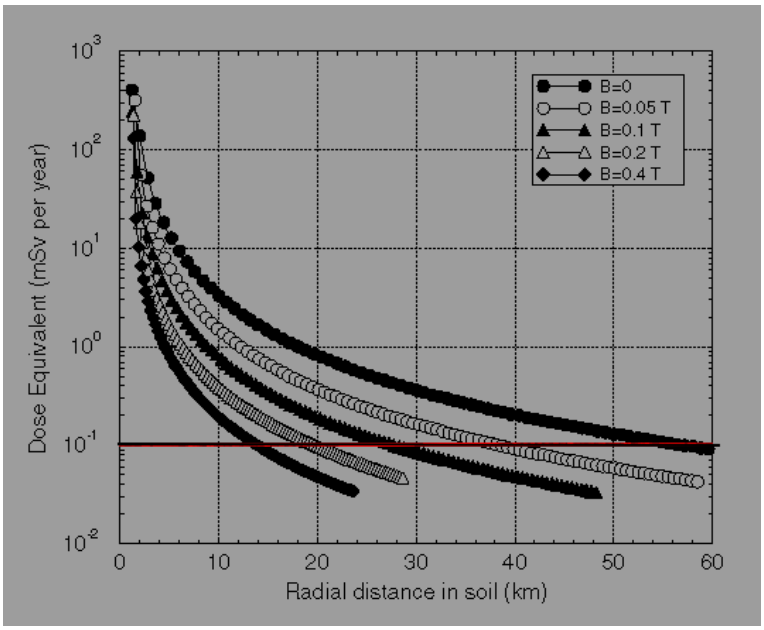

Fig. 7.4: Calculated fluxes of irradiation from a 2 × 2 TeV collider ring (1 mSv = 100 mrem), as a function of distance from the ring. The B indicates the value of the B field used to produce a vertical wave in the beam orbit. The graph shows that the peak irradiation can be greatly reduced with relatively small perturbing fields ($\sim$ 0.1 T).

Several strategies are possible for reducing and/or eliminating the difficulties due to this effect. These include:

1. Placing the collider ring deeply enough that the neutrino radiation does not reach the surface (or any other potential exposure point) until the radiation density is below acceptable levels. The distance from ring to surface L as a function of depth D is given by L $\cong$ $(2RD)^{1/2}$, where R is the earth's radius. For a ring at a a depth of 200 m, the

beam does not reach the surface until a distance of ~ 50 km. This distance would provide adequate dilution for colliders up to a few TeV in energy.

2. The above calculations assume the orbit is completely planar, and that the radiation therefore propagates only within a narrow band, and the narrowness of that band determines the localized radiation density. Vertical orbit oscillations would increase the width of that band, and correspondingly reduce the peak flux. These oscillations would have to be varied over the operational year to reduce peak fluxes. Reduction of peak intensities by at least an order of magnitude is readily obtained with small orbit oscillation (see Fig. 7.4).
3. The collider ring geometry could be tilted such that all straight sections point either toward a region on a laboratory site, where access can be controlled, or toward a distance very far from the lab (1000+ km) where the radiation is greatly diluted. It is, however, difficult to ensure that all neutrino paths from the arcs avoid nearby areas which could potentially be occupied.
4. The location of the collider ring can be chosen such that no potential neutrino beam points toward a potentially continuously occupied point; that all neutrino lines are confined within a controlled-access laboratory, or in the air or in an ocean. Possibilities include siting the ring on an island or on a mountain.
5. New cooling methods can reduce the emittances of the beam significantly and thereby allow the achievement of high luminosity with much lower muon intensities, and hence much lower neutrino radiation.

References

[1] The Super-Kamiokande Collaboration, Phys. Rev. Lett. **81**, 1562 (1998).

[2] C. Athanassopoulos et al., Phys. Rev. Lett. **75**, 2650 (1995).

[3] S. Geer, Phys. Rev. **D57**, 6989 (1998).

[4] D. Cline and D. Neuffer, *Proc. Int. Conf. High-Energy Physics*, AIP Conf. Proc. **68**, pt. 2, 846 (1980).

[5] S. Geer, C. Johnstone and D. Neuffer, Fermilab TM-2073 (1999).

[6] S. Geer, C. Johnstone and D. Neuffer, Fermilab-Pub-99/121, submitted to Nucl. Instrum. Methods A (1999).

[7] NuFact'99, Institut de Physique Nucléaire, Lyon, France, 5-9 July 1999.

[8] B. King, *Proc. 1999 PAC Conf.*, New York, NY (1999).

[9] C.J. Johnstone and N. Mokhov, *Proc. 1997 PAC Conf.*, Vancouver, BC, p. 414 (1999).

8 μ^+–μ^- COLLIDER R&D PROGRAMME

8.1 Introduction

A multilaboratory collaboration has been formed to explore the possibility of a μ^+–μ^- collider, and to investigate critical questions in determining its feasibility and its practicality. Following initial studies presented at Snowmass, the high-energy physics advisory panel recommended expan-ded research including simulations and experiments to determine the feasibility of μ^+–μ^- colliders [1]. In response the μ^+–μ^- Collaboration is expanding its efforts, including experiments on targetry/production at BNL [2] and cooling at Fermilab [3]. The Collaboration will use these experiments to determine the practicality and performance of key components of the μ^+–μ^- collider and integrate that knowledge into optimizing the scenarios.

8.2 Simulation studies

A large portion of the collaboration effort is devoted to simulation studies of critical elements of a μ^+–μ^- collider complex. These studies include studies of the π-production and μ-collection process, and beam cooling studies, as well as detailed design and development of the cooling channel and other systems needed to obtain the high-intensity muon beams. Much of this research has been discussed in the previous sections; we summarize this work and indicate the present goals of the collaboration. This discussion is based on the muon collider status report [4] (and references cited therein), and on the discussions at the recent Muon Collider collaboration meetings, including the St. Croix meeting [5].

In the targetry and π production systems, the MARS simulation codes of N. Mokhov and collaborators have been used as a primary tool in studying the pion production systems. Results of the BNL E910 π production experiment must be compared and integrated with these simulation tools. The magnetic and thermal behaviour of the liquid jet targets is being modelled by Hassanein et al.

In the RF rotation systems some simulations have been developed and run to provide various optimum conditions. Integration of optics and RF designs with practicality constraints and matching with cooling needs further research and study. Development of rotation systems adapted to high-frequency RF systems, as well as the RF rotation designs for muon neutrino sources are also under study.

In beam cooling the ICOOL and DPGeant codes have been developed to provide detailed simulations of beam interactions with beam transport and focusing devices. Integration of these simulations with beam transport codes is less advanced, and optimization of cooling sections, emittance exchange designs, and integration of cooling designs into complete cooling systems remain to be done. Initiatives on studying the beam optics and optimization problem are in progress at LBL, FNAL, and BNL.

Detailed simulation of the acceleration systems has not yet been properly pursued, but the topic has been assigned a high priority by the collaboration for further study. H. Padamsee has initiated studies of the use of superconducting RF in the acceleration systems. Wakefields in the higher-frequency recirculating linac cavities has been identified as a potential problem for further study.

For the collider, critical simulations of the beam decay-detector background problem are being performed by Stumer and Raja et al. Lattice design, instability, beam-beam, and collimation studies are continuing.

The recent interest in neutrino oscillations has led to initiatives on developing muon storage rings for the purpose of neutrino beams; design-centred studies on this concept are in progress at FNAL, CERN, and BNL.

Each of these systems requires innovative development of RF acceleration and magnet systems; design on these is in progress and developing prototypes of the hardware for specific cases are part of the targetry and cooling experiments described below.

8.3 Targetry experiment

An experiment has been proposed to be based at the Brookhaven AGS to explore several critical issues related to targetry, $\pi \rightarrow \mu$ collection, and phase rotation, and some hardware R&D related to that experiment has been initiated. As discussed above, a liquid jet target could be used to circumvent problems of target destruction from the high-intensity proton beam, and to avoid pion recapture by material supporting the target. A pump that produces short jets of liquid metal, shaped to the μ^+–μ^- source requirements is being developed and tested. While several possible alloys will be tested, an attractive choice is the use of jets of the room-temperature liquid eutectic alloy of Ga-Sn. After pump and jet formation problems are solved, the jets would be inserted into a BNL beam line and exposed to nanosecond pulses of 1.5×10^{13} 24 GeV protons. The effects of high-intensity beam on the jet will be explored. The same jet would also be inserted into magnetic fields, with initial tests in a 20 T, 20 cm bore resistive magnet at the National High Magnetic Field Laboratory (Talahassee, Florida) to study the effects of eddy currents on jet propagation. Then a pulsed 20 T magnet will be added to the BNL test station to explore the full configuration of jet, magnet, and pulsed proton beam.

The experiment will include development of the low-frequency RF systems with solenoidal focusing which are to be used in the muon capture, RF rotation, and early cooling. A 70 MHz RF cavity within a 1.25 T solenoid will be developed and tested within beam. The cavity will be exposed to the intense flux of secondary particles downstream of the target with 20 T capture magnet to determine viable operating parameters for the first phase rotation cavity. The complete configuration of the targetry experiment is sketched in Fig. 8.1.

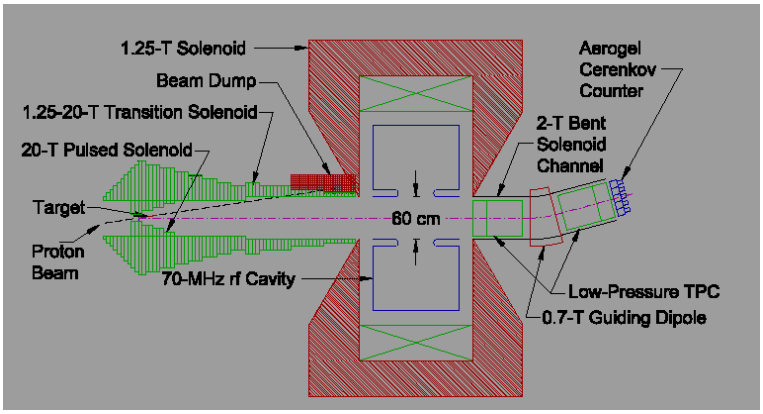

Fig. 8.1: Overview of the BNL-based targetry experiment.

The initial studies of jet formation and exposure to magnetic filed at the National High Magnetic Field Laboratory should be accomplished during 1999 and the later studies with beam in 2000 to 2001.

8.4 Cooling experiment

Another large effort has been initiated in developing the first demonstration of ionization cooling, and thereby exploring and optimizing the cooling scenario and components. A cooling

experiment has been proposed at Fermilab, and development of initial components and detailed planning for that experiment is in progress. Details of the experiment can be found in Fermilab proposal P904 [3], and a summary of the R&D programme can be found in Ref. [4]. The goal of the cooling R&D programme is to develop the muon ionization cooling hardware to the point that a complete cooling channel for a μ^+–μ^- collider can be fully defined and constructed.

The proposed R&D programme consists of:

- Developing an appropriate reacceleration structure for cooling. Research efforts are focused on developing an 805 MHz RF system, where 805 MHz is chosen because of the availability of high-power sources at this frequency, the existing Fermilab equipment and expertise at 805 MHz, and its suitability for use in much of the cooling channel, including the cooling in a first demonstration experiment. An innovative pillbox structure with thin Be windows along the beam line is being studied; the pillbox design with conductor on axis enables the peak cavity surface field to be equal to the accelerating field, and the weakly-interacting muons are not greatly affected by passing through thin windows. An alternative design with open, large apertures is also being developed; the accelerating field is only $\sim 1/3$ of the peak surface field, however. Accelerating gradients of $\sim$ 30 MV/m are required for cooling while maintaining the beam within a stable bunch at these frequencies.
- Prototyping a complete alternating solenoid (ASOL) transverse cooling stage, which consists of several cells of absorber + reacceleration RF with focusing solenoids. A prototype cell design is displayed in Fig. 8.2. After construction and bench testing, the cooling stage would be placed in a beam line and measurements made to determine if cooling performances meets expectations (Fig. 8.3).

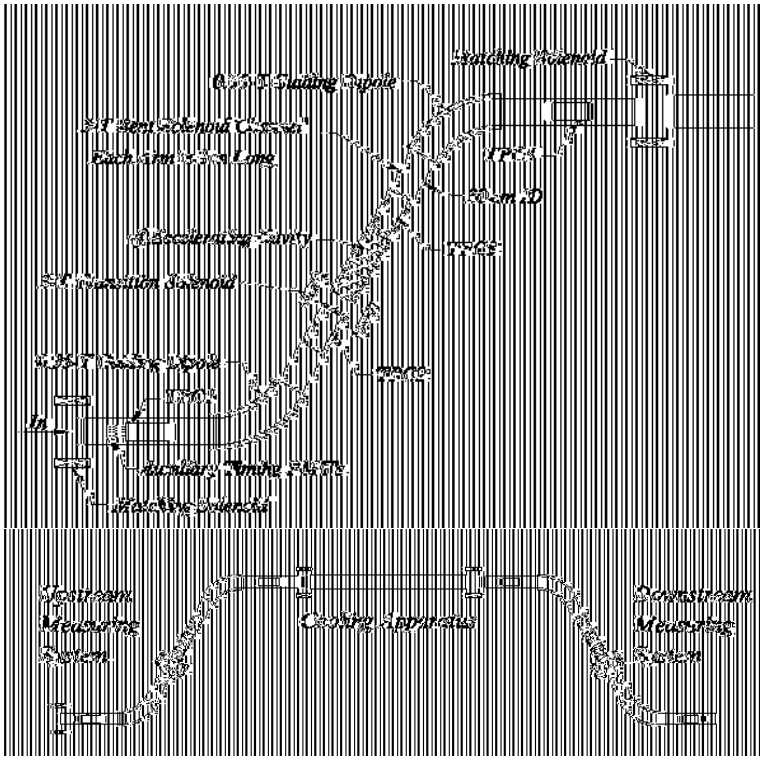

Fig. 8.2: Design of an ASOL cooling segment for the MuCOOL experiment, showing RF cavities, and liquid hydrogen absorbers within high-field solenoids.

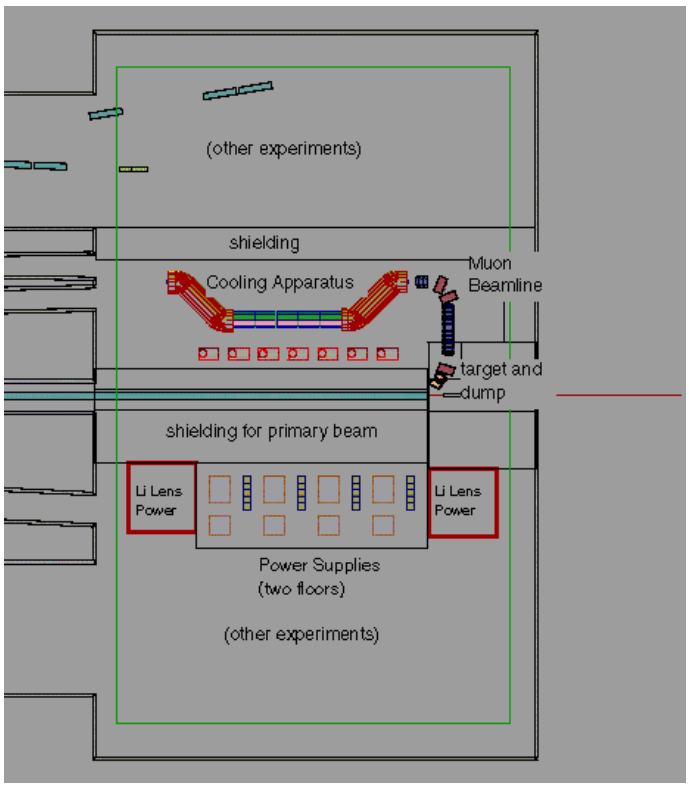

Fig. 8.3: Beam line with measurement equipment for measuring particle properties before and after entering a cooling apparatus. The bent solenoids with cavity enable energy and phase measurements. Transverse positions and angles are also measured.

- Prototyping an emittance exchange (wedge absorber with dispersion + focusing) system, such as the bent solenoid system described in Chapter 4, or a more conventional design combining bending magnets with focusing. The system would also be tested with beam, and it would be desirable if this exchange section could be combined with the ASOL prototype to obtain simultaneous transverse and longitudinal cooling.
- Prototyping a long Li lens absorber. It is currently expected that an optimal cooling lens would be relatively long ($\sim$ 1 m), and high-gradient (large surface field with smaller radii) is desired, since as discussed above the ultimate achievable emittance depends on that gradient. A contract with BINP (Silvestrov et al.) is being developed for an initial design and construction of a lens for cooling. Initial parameter goals are a 1 m long lens with 0.5 cm radius and a peak field of 20 T.
- Following the Li lens R&D, a prototype Li lens-RF-Li lens system will be prototyped and its performance measured in a muon beam. This cooling section could be matched with a longitudinal cooling (wedge or ?) system to be developed.
- Other cooling devices, perhaps significantly different from those currently expected, could also be developed and tested using the beam line and facilities devoted to the cooling experiment.

In addition to the cooling devices discussed above, the experiment will require a suitable m-beam line, an experimental area for insertion of the cooling devices, and the diagnostic equipment for measurement of the beam before and after the experimental area. Currently several candidate areas are being considered. The Fermilab meson Lab had space available within an existing beam line, which could be adapted to receive protons from the main injector (120 GeV), and produce π's in a meson line target, with μ's reaching the experimental area. Figure 8.4 shows the Meson lab with a target and secondary beam transport installed and instrumented for the cooling

experiment. However, external beam use of the main injector may be limited. A new beam line and lab connected to the Fermilab booster (8 GeV p) could be developed, and has the advantage that booster beam is more readily available, and is closer to the desired parameters of the μ^+–μ^- collider proton source. An experiment near the booster could be more readily extended to include more cooling and a new channel could be more readily incorporated into a future high-intensity μ^+–μ^- source, which would be based on a proton accelerator in this area.

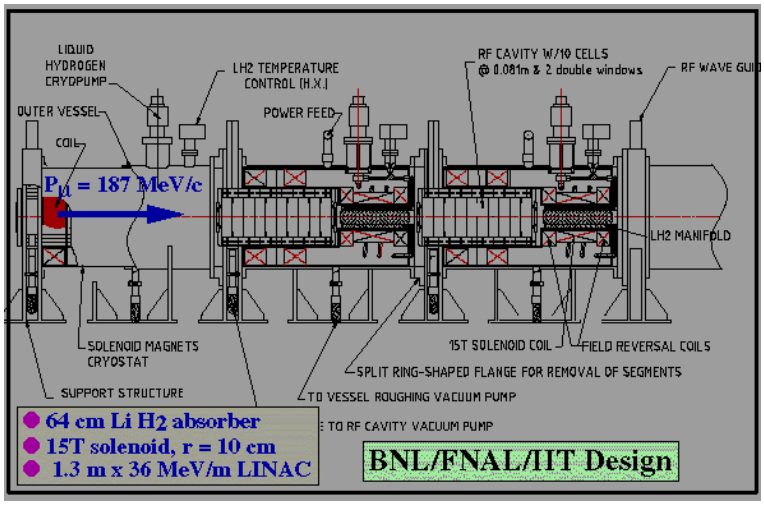

Fig. 8.4: MuCool experimental setup in the Fermilab Meson lab showing the beam source (beam would be bent backward from the target). Power supplies for RF and Li lens are shown.

The experiment also requires equipment for beam measurement before and after the cooling section. In the initial design, individual m trajectories entering and leaving the cooling area are tracked, and sums over a large number of accepted individual tracks will be used to form a virtual beam, whose progress (in 6D phase space) will be calculated to determine the degree of cooling. Thus in this mode the beam is simply a statistical ensemble of individual tracks, and the properties of individual trajectories, as well as the ensemble, can be studied.

An alternative approach, which requires more μ's, is to form the input beam into intense bunchlets, with sufficient intensity to measure the beam parameters in collective form using standard beam monitoring methods. This would require $\sim 10^6\,\mu$/bunchlet. Obtaining these muons would require a more intense source than that available for the Meson lab. Proton bunches from the Fermilab booster, or a future proton driver, may provide sufficiently intense pulses. Beam line designs for both modes of operation (single-particle or intense bunch) are being developed.

8.5 Summary status

The μ^+–μ^- collider research effort is expanding, with increasing funding support from the national laboratories and the Department of Energy. A Technical Advisory Committee (chaired by M. Tigner) has been formed to review the research on a regular basis.

The experimental proposals on targetry and μ-cooling have been submitted to the programme advisory committees at BNL and Fermilab, respectively, and have been favourably received. Development and acquisition of critical experimental components has been initiated, including RF cavity prototype construction and tests, liquid jet tests, etc. The simulation efforts are expanding, and prototype designs for transverse cooling segments have been designed and tested by simulation. Initial scenarios for $\pi \rightarrow \mu$ production, capture, and phase space rotation are ready for experimental tests, while innovative variations are being tested by sim-

ulation. A key challenge for the R&D effort is development of practical emittance exchange (longitudinal cooling) segments, and integration of these with the transverse cooling segments, with reoptimization of a complete cooling scenario.

The significant application of using the intense μ-beams to obtain ν-beams for precision measurements of ν-oscillations is being explored, and practical designs will be developed.

The collaborative effort is expanding to an international level, with significant support and interest at CERN and KEK. CERN has formed a study group on μ^+–μ^- colliders within a general R&D programme searching for meaningful post-LHC projects, with an initial emphasis on the μ-storage ring for ν-beams applications. As discussed above, many difficulties must be solved in order to obtain a practical μ^+–μ^- collider, and many opportunities for innovative solutions and improvements remain. We hope that the presentations in these lectures will encourage the readers to consider and solve some of these challenges.

References

[1] F. Gilman et al., HEPAP subpanel report on Planning the Future of US High-Energy Physics (1998).

[2] J. Alessi et al., *An R&D Program for Targetry at a Muon Collider*, Proposal E951 to the BNL AGS (September 1998).

[3] C.N. Ankenbrandt et al., *Ionization Cooling Research and Development Program for a High Luminosity Muon Collider*, FNAL-P904 (April 15, 1998).

[4] Muon Collider Collaboration, 'Status of Muon Collider Research and Development and Future Plans', BNL-65623, Fermilab-PUB-98/179, LBNL-41935, submitted to Phys. Rev. Special Topics (1998).

[5] Muon Collider Collaboration, discussions at the May 1999 collaboration meeting, St. Croix, VI, 19–26 May, 1999.